Development of a kinetically controlled plasma induced chemical ionisation source

Dissertation submitted to the School of Mathematics and Natural Sciences of the Bergische Universität Wuppertal in partial fulfilment of the requirements for the degree

Doctor of Natural Science in Chemistry

(Dr. rer. nat.)

by

David Benjamin Müller

Wuppertal

2019

The PhD thesis can be quoted as follows:

urn:nbn:de:hbz:468-20200212-113232-0
[http://nbn-resolving.de/urn/resolver.pl?urn=urn%3Anbn%3Ade%3Ahbz%3A468-20200212-113232-0]

DOI: 10.25926/qtrc-ka79
[https://doi.org/10.25926/qtrc-ka79]

“It is the great glory of the quest for human knowledge that, while making some small contribution to that quest, we can also continue to learn and to take pleasure in learning.”

William A. Fowler

Acknowledgement

Mein Dank gilt…

… Prof. Dr. Thorsten Benter für das Ermöglichen der Arbeit und die Betreuung dieser. Vor allem aber danke ich dir für die Aufnahme in die Arbeitsgruppe und Unterstützung in all den Jahren, in denen ich Teil der Arbeitsgruppe sein durfte.

… Dr. Hendrik Kersten für viele Inputs zu Experimenten. Danke für die vielen Ideen und kritischen Diskussionen mit dir.

… Dr. Yessica Brachthäuser für die lange und gute Zusammenarbeit. Danke für die vielen gemeinsamen Labor- und Bürostunden.

… Ronald Giese für die Umsetzung neuer Ideen in Modelle und Zeichnungen.

… Nele Hartmann für die Hilfe und gute Zusammenarbeit in diesem Projekt im Rahmen ihrer Masterarbeit.

… Duygu Erdogdu und Robin Hillen für die Mithilfe in diesem Projekt im Rahmen ihrer Bachelorarbeiten.

… der gesamten Arbeitsgruppe der Physikalischen und Theoretischen Chemie für viele unvergessliche Erinnerungen, von konstruktiven Meetings, unterhaltsamen Telkos und zahlreichen Konferenzaufenthalten und Feiern, die ich im Laufe der Jahre ansammeln durfte.

… Prof. Dr. Hans-Willi Kling für das Zweitgutachten dieser Arbeit.

Mein besonderer Dank gilt…

… meinen Eltern und meinem Bruder, die mich auf dem gesamten Weg unterstützt haben.

… Jasmin für die Unterstützung in guten wie vor allen in den schlechten Zeiten. Danke, dass du mich immer wieder aufgebaut hast und immer für mich da warst.

Abstract

Chemical ionisation (CI) is a widely used ionisation technique for mass spectrometer (MS), forming predominantly molecular ions and/or protonated ions. With these ionic species, the analyte identification by molecular weight is possible even in complex mixtures. Thus, chemical ionisation is ideal for ambient sampling applications. However, most common ion sources show long residence times of the analyte in the ion source leading to post-ionisation transformations. In this work, the parameters influencing the kinetic control of ionisation were investigated, allowing the mass spectrum to mirror the neutral ensemble. Three ion sources were constructed to investigate proton transfer reaction at low-pressure conditions utilising H_3^+ as reagent ions. A helium plasma expanding into a hydrogen atmosphere is the basis for the initial two ion sources. The third utilises hydrogen as reagent gas to form protonated analyte ions within a nitrogen atmosphere. Based on these results, three additional ion sources were developed to investigate the kinetically controlled proton transfer for ambient sampling. This enables the mass spectrum to mirror the distribution of the neutral ensemble. These ion sources utilise a stacked chamber system with hydrogen as reagent gas facilitating optimisation of each reaction step separately. Concomitantly, modifying existing AP-MS instruments to low-pressure sampling was investigated by coupling this ion source series to a modified AP-sampling mass spectrometer. The last ion source design permits the addition of a secondary reagent gas lowering fragmentation by reducing possible excess proton transfer energies. Here, besides methane and *i*-butane, perfluoro compounds were tested as possible broadband reagents.

Contents

1 Introduction

1.1 Chemical Ionization

Chemical ionisation (CI) is a widely used ionisation technique for mass spectrometer (MS).[1] In contrast to direct ionisation methods as electron ionisation (EI) or photo ionisation (PI), the ionisation of the analyte in CI is proceeding via chemical reaction sequences with reagent ions. These are generated separately or in-situ, often in a reaction cascade. Thus, the analyte ionisation takes place after several steps, including the transformation of the primarily available energy into reagent ions and further reactions of these with the analyte.[2–4] The type of ionisation reaction depends on both the properties of the reagent ion and the analyte.[2, 5] Possible ionisation reactions are electron transfer (mostly known as charge transfer, CT) and residue transfer, which is mostly proton transfer (PT) or proton abstraction.[6]

After ionisation of the analyte via CI, further reactions can occur within the ion source environment. These are referred to as ion-transformation processes and have a great influence on the resulting distribution of the detected ion population.[7, 8] They occur especially in atmospheric pressure (AP) MS due to the comparably high pressure causing multiple ion-molecule collisions. The combination of all reactions dictates the detected ion population, which may significantly vary from the primarily generated ion distribution.[7, 8]

The main advantage of CI as compared to other methods is the variability of the excess energy transferred to the target molecule, which provides a method to control the extent of fragmentation.[1]

1.1.1 Historical overview of the CI development

Chemical ionisation mass spectrometry was first published by Mundson and Field in 1966 and is a result of ion-molecule reaction studies.[3, 6] Chemical reactions inside mass spectrometers were observed in the very early days but became less important with improved vacuum conditions. The study of ion-molecule reactions started with the self-protonation of hydrogen resulting in H_3^+, which was speculated about by Thomson in 1912 and explored by Dempster in 1916.[9–11]

$$H_2^+ + H_2 \rightarrow H_3^+ + H \quad (1)$$

When discovering that the self-protonation of methane is faster than reactions involving only neutral species, the interest focused on CH_5^+.[6] Thus, in the 1950^{ths}, numerous studies were carried out on CH_5^+. Consequently, the first CI-MS used methane as the reagent gas.[3]

Nowadays, the most commonly used reagent gas is still methane, although many different reagents (e.g. hydrogen, *i*-butane, ammonia, tetramethylsilane, helium, benzene, nitric oxide) were studied.[12, 13, 22, 23, 14–21]

At first, the reagent gas was directed into a modified EI source.[3] Since then, not much has changed concerning the instrumental arrangement of classical CI, but many CI methods and sources were invented.[1]

1.1.2 Different CI methods

Today, there is a broad family of CI methods with numerous applications. These methods can be categorised by the two parameters reagent gas and primary ionisation mechanism.

In classical CI, the reagent ions are produced via EI at a reduced pressure of about 1 mbar. Besides that, other approaches are, for example, in dopant assisted atmospheric pressure photoionisation (DA-APPI)[24, 25] or atmospheric pressure chemical ionisation (APCI).[26–28] In DA-APPI the reagent (called dopant) is ionised by absorption of vacuum ultraviolet (VUV) photons and may then react with the analyte by transferring energy. The basis of APCI is a point-to-plane

plasma ("Corona") for this purpose. The ionisation mechanism in APCI is well described and mainly utilises either protonation by proton bound water clusters or charge transfer via N_4^+ as main reagent species.[29, 30]

Table 1: Gas phase basicity (GB) and proton affinity (PA) for selected compounds.[31]

substance	GB [kJ/mol]	PA [kJ/mol]
helium	148.5	177.8
neon	174.4	198.8
fluorine	305.5	332.0
argon	346.3	369.2
oxygen	396.3	421.0
hydrogen	394.7	422.3
krypton	402.4	424.6
hydrogen fluoride	456.7	484.0
nitrogen	464.5	493.8
xenon	478.1	499.6
nitric oxide	505.3	531.8
carbon dioxide	515.8	540.5
methane	520.6	543.5
nitrogen dioxide	560.3	591.0
i-butane	671.3	677.8
water	660.0	691.0
2,2,2-trifluoroethanol	669.9	700.2
trifluoroacetic acid	680.7	711.7
benzene	725.4	750.4
toluene	756.3	784.0
p-xylene	766.8	794.4

The ionisation mechanism, the excess energy of the reaction step charging the analyte as well as the range of ionisable analytes can be adjusted by changing the reagent gas. In principle, to increase the range of ionisable analytes, an energetically higher positioned reagent has to be used. On the one hand, this

transfers more energy to the analyte, potentially leading to higher internal energy deposited in the resulting ion and thus fragmentation. On the other hand, reagents depositing lower excess energy may not be able to ionise some analytes. For protonation, an estimation of this excess energy is the difference of the proton affinities (PA) between reagent and analyte as listed in Table 1. A prerequisite is that the reagent is used as a protonated species, and the reaction is bimolecular. In classical CI, methane produces $C_2H_5^+$ in addition to CH_5^+, the dominant protonating species.[1, 3, 12]

According to the calculated energy value, the reagent cannot protonate the substances listed above it. As an example, N_2H^+ as reagent ion protonates xenon but not krypton. While methane is often used as a universal reagent for most analytes, *i*-butane is known for ionisation with low fragmentation.[12] Also, water does not interfere with the ionisation of many analytes (Table 1), which can be useful for measurements at atmospheric pressure.[12, 32] The high proton affinity of water allows suppression of the ionisation of bulk gases and ionisation of analytes with even lower fragmentation as compared to methane CI. Still, water as reagent can protonate a broad range of analytes. Based on this advantage, proton transfer reaction (PTR) MS utilises water as a reagent.[33–35] An electric field must be applied in the analyte ionisation region due to the rapid cluster formation of water and the low ionisation reactivity of larger clusters.[36] The electrical field accelerates ions, including the water clusters of the type $[(H_2O)_n+H]^+$ (n= 1,2,3,…), which leads to shifts in the corresponding equilibrium system. With a reduced electric field strength in the typical PTR range of 100 Td[1], the cluster system shifts to predominantly H_3O^+.[33] While the ionisation process in PTR leads only to minor fragmentation, the required strong electric field causes fragmentation via collision-induced decomposition (CID) processes.[33, 37]

[1] The unit Townsend (Td) is used for the reduced electrical field strength E/N, were E is the electrical field strength and N is the number density of the gas. 1 Td = 10^{-21} V·m^2. The reduced field strength represents a measure of the mean energy of ion molecule collisions in the electrical field.[33]

1.2 Plasma-based CI methods

In the last century, ambient ionisation methods became popular due to their user-friendly sample preparation.[38–40] Many of these ionisation methods as well as several earlier implementations use plasma discharges as primary energy sources.

Direct analysis in real time (DART)[41], low-temperature plasma (LTP)[42], and flowing atmospheric pressure afterglow (FAPA)[43, 44] are such plasma-based ambient methods. In most cases, a helium plasma is used to generate metastable species, which ionise the reagent gas. The two relevant helium metastable states are 2^3S with 19.8 eV and 2^1S with 20.6 eV potential energy.[45] These metastable species will not form ions out of helium, only a collision of two metastable species might result in ionisation.[46] Under ambient conditions, the reagent gases are most likely nitrogen and water, leading to N_2^+, N_4^+ H_2O^+, and $[(H_2O)_n+H]^+$.[26, 36, 40, 47] The analyte is either directed through the discharge region or mixed with/desorbed by the primary gas flow. In most cases, the ion-molecule chemistry is not controlled in any way other than via thermodynamically controlled equilibration of the entire reaction system.

1.2.1 Plasma

Plasma is the state of matter, in which electrons and ions are present at the same time. Gas in the plasma state can maintain an electric current from one electrode to the other. This is also known as a gas discharge.[45] A plasma is a non-equilibrium system, which produces a self-sustaining reaction system after ignition, propelled by the electrical field. To ignite a plasma, a voltage is applied to the pair of electrodes enclosing the discharge gas. This so-called breakdown voltage U_b is given by the approximation depicted in equation 1.

$$U_b = \frac{B(N_a L)}{\ln\left[A\, N_a L / \ln(1+\frac{1}{\gamma})\right]} \qquad \text{(eq. 1)}$$

γ is the second Townsend coefficient, A and B represent empirical constants, which are selected to fit measured breakdown voltages.[48] Figure 1.1 shows the dependence of breakdown voltages and the distance of two parallel electrodes (L) and the number density of atoms (N_a) for typical discharge gases (Paschen curves).

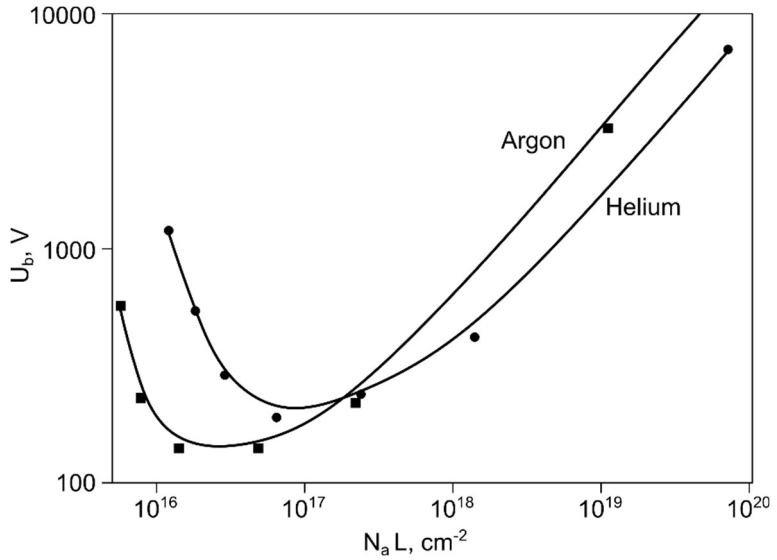

Figure 1.1: Paschen curves of argon and helium as discharge gases. [45]

The self-sustained mode results from the formation of secondary electrons, which can occur in two different ways. First, the electric field gradient accelerates free electrons producing secondary electrons by interaction with atoms of the discharge gas. This process is described by the first Townsend coefficient (α) and is often referred to as avalanches. Second, the generation of secondary electrons via processes detaching electrons from the cathode by ions, excited atoms or photons as described by the second Townsend coefficient (γ).[45]

In addition to electrons, atoms, and ions, the plasma contains electronically excited species. In helium, these species are mainly metastable helium atoms (He^M), dimers (He_2^M) and excimers (He_2^+). The species of interest for this work are the two helium metastables He(2^3S) with 19.8 eV and He(2^1S) with 20.6 eV. The population distribution of the two species depends on the electron energy available for ionisation and therefore on the electric field strength. Figure 1.2 shows the energy losses of electrons in helium depending on the electric field strength. For slow electrons (E/N < 6 Td), the energy is fully converted into elastic collisions. In the range of 10 - 40 Td, mostly excited species appear, while even higher electron acceleration is required to ionise helium.[49]

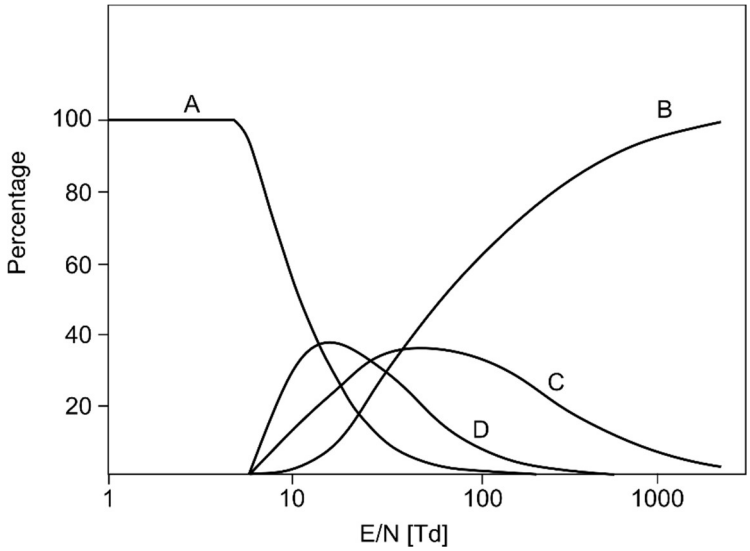

Figure 1.2: Energy losses in helium, percentages of the appearance of A, elastic collisions; B, ionisation; C, excitation (2^1S); D, excitation (2^3S).[49]

1.3 Chemistry in CI sources

The chemistry in a CI source can be sequenced into several steps. First, the generation of primary reagent ions, then ion-molecule reactions occur finally leading to the analyte ion(s). Depending on the gas mixture, the primary reagent ions can react with other compounds prior to analyte ionisation. This can lead to other secondary reagent ions with lower gas-phase acidity up-to the loss of protonation capability. After analyte ionisation, further ion-transformation processes can also occur.

1.3.1 Ion-molecule reaction

In classical CI, primary reagent ions are generated via 70 eV EI[3], which leads to significant fragmentation. For methane, this primarily results in CH_5^+ and $C_2H_5^+$ ions, but further ionic species (2-6) are also observed.[3, 6]

$$CH_4 + e^- \rightarrow CH_4^+, (\text{also } CH_3^+, CH_2^+, CH^+, C^+, H_2^+, H^+) + 2\ e^- \quad (2)$$

$$CH_4^+ + CH_4 \rightarrow CH_5^+ + CH_3^\bullet \quad (3)$$

$$CH_3^+ + CH_4 \rightarrow C_2H_5^+ + H_2 \quad (4)$$

$$CH_2^+ + CH_4 \rightarrow C_2H_4^+ + H_2 \quad (5a)$$

$$CH_2^+ + CH_4 \rightarrow C_2H_3^+ + H_2 + H \quad (5b)$$

$$C_2H_3^+ + CH_4 \rightarrow C_3H_5^+ + H_2 \quad (6)$$

Depending on the reagent ion (R), several possible reactions with the analyte (A) can occur. Proton transfer species (RH^+) will show mainly proton transfer reactions and/or adduct formation (7-8).[6]

$$RH^+ + A \rightarrow [A+H]^{+*} + R \quad (7)$$

$$RH^+ + A \rightarrow [A+RH]^{+*} \quad (8)$$

Additionally to the analyte protonation, reaction 7 also represents proton transfer reactions between different analytes for $PA_{(A)} < PA_{(A')}$. Depending on the difference in proton affinity, both ionised species possess excess energy, which can be swiftly removed by collisions with bulk gas (M, 9). Alternatively, it can lead to fragmentation. A typical CI-fragmentation process leads to loss of H_2 (10).[4]

$$[A+H]^{+*} + M \rightarrow [A+H]^+ + M \quad (9)$$

$$[A+H]^{+*} \rightarrow [A-H]^+ + H_2 \quad (10)$$

Thus, in classical methane CI, $[M\pm H]^+$ ions are the expected main analyte species, as long as the excess energy is sufficiently low. In addition to fragmentation, other ion transformation processes potentially influence the nature of the detected ions through reactions with neutral radicals or molecules, recombination reactions or clustering with neutral molecules.[7, 8]

Replacing the electron source with a helium plasma, the initial chemistry as shown for methane (Reactions 2-6) is almost identical since the energy of the metastable species (19.8 eV) causes fragmentations comparable to EI (70 eV).[50–52] In contrast, hydrogen as reagent gas generates a smaller diversity of ionic species and therefore provides a more defined secondary ion-molecule chemistry.

$$He^M + H_2 \rightarrow HeH^+ + H + e^- \quad (11)$$

$$He^M + H_2 \rightarrow H_2^+ + He + e^- \quad (12)$$

$$He^M + H_2 \rightarrow HeH_2^+ + e^- \quad (13)$$

$$He^M + H_2 \rightarrow H^+ + He + H + e^- \quad (14)$$

$$He^M + H \rightarrow HeH^+ + e^- \quad (15)$$

$$He^M + H \rightarrow He + H^+ + e^- \quad (16)$$

In a hydrogen atmosphere, these species rapidly convert to H_3^+ via the following pathways:

$$H_2^+ + He \rightarrow HeH^+ + H \quad (17)$$

$$H_2^+ + H_2 \rightarrow H_3^+ + H \quad (18)$$

$$HeH^+ + H_2 \rightarrow H_3^+ + He \quad (19)$$

$$H^+ + H_2 \rightarrow H_3^+ + h\nu \quad (20)$$

$$H^+ + H \rightarrow H_2^+ + h\nu \quad (21)$$

After a sufficient dwell time within the hydrogen atmosphere, H_3^+ is the only generated reagent ion.[54] According to reaction 7, H_3^+ protonates methane. In contrast to EI, no fragmentation of methane ions is observed.[21] Thus, CH_5^+ is the solely formed methane reagent ion. While CH_5^+ does not react with nitrogen, both methane and hydrogen ions will protonate water molecules. Depending on the number of collisions, the protonated water will react further with additional water molecules rapidly forming an entire cluster equilibrium system:[36]

$$[(H_2O)_n+H]^+ + H_2O + M \rightarrow [(H_2O)_{n+1}+H]^+ + M \quad (22)$$

$$[(H_2O)_{n+1}+H]^+ + M \rightarrow [(H_2O)_n+H]^+ + H_2O + M \quad (23)$$

1.3.2 Kinetic vs thermodynamic control

The resulting detected ion distribution thus depends on the path of the reaction cascade in the CI source as well as on the extent of ion-transformation processes.

The influence of individual elementary reactions is determined by the bi-/ter-molecular rate constant k, the mixing ratio, the pressure and the temperature. For ambient sampling, the analyte flow generally contains a high amount of water (up to 3% by volume) as well as several analytes. Under such conditions, the time is sufficient for the entire reaction system to equilibrate fully (sometimes referred to as thermodynamic control). Regarding $[M+H]^+$ formation, these conditions may also lead to discrimination of analytes with lower proton affinity.

In synthetic organic and inorganic chemistry, kinetic and thermodynamic control are defined as two or more pathways exhibiting different activation energies between the reactant and product side as depicted in Figure 1.3. In this example, the reactants can overcome the activation barrier via two different pathways. The kinetically controlled path proceeds via lower activation energy but leads to an energetically less favourable product. In contrast, the thermodynamic pathway requires higher activation energy but yields the energetically more favourable product. In this case, the reaction conditions can be chosen to favour one of the two possible products. Product A is the so-called kinetic product, whereas product B is the thermodynamic product. With sufficient energy and time, the system will end up with a higher yield of product B.

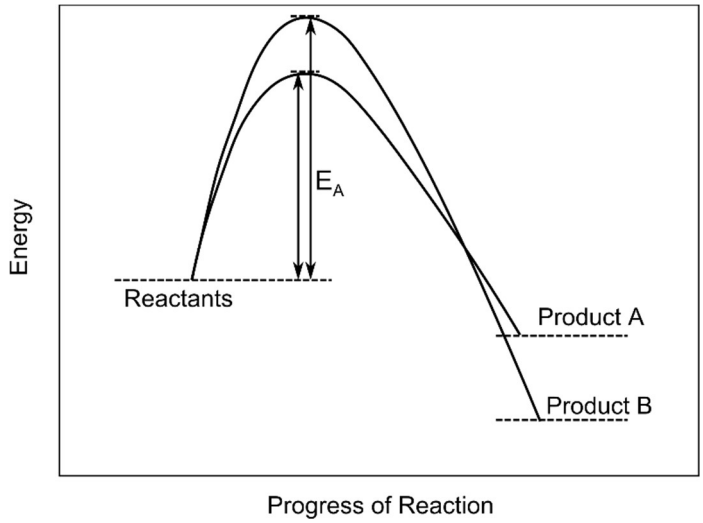

Figure 1.3: Kinetic vs thermodynamic control in classic chemistry; Dependence of the energy of a reaction and the progress, product A is the kinetic product (lower activation energy), product B is the thermodynamically preferred product.

In mass spectrometry, only very few examples of this kind of kinetic vs thermodynamic control as is defined above are published. For example, Joyce and Richards investigated the different protonation sites of crizotinib, an anti-cancer drug, with ESI-MS.[55] Another more recent investigation by Xia and Attygalle shows the shift between the N- and O- protomer of benzocaine depending on the source conditions.[56]

Alternatively, several publications apply the term of kinetic control with regards to the suppression of post-ionisation secondary ion transformation processes.[57–61] A completely equilibrated system ($dG = 0$) is referred to as thermodynamically controlled, whereas every state prior is referred to as controlled by the kinetics.[62] This definition refers to the limited number of collisions the primarily formed analyte ions undergo during the transit time from the ion source to the collision-free environment of the MS. The kinetic product is then the desired analyte ion (formed in reaction 7 and 8), the thermodynamic products are secondary ions formed by post-ionisation processes with the analyte ion as a reactant. A higher kinetic control can be achieved by limiting the reaction time and thus minimisation of the number of collisions. Consequently, the measured ion distribution represents the neutral ensemble in the ion source closely. With longer reaction times (more collisions), the ion distribution shows the thermodynamically favoured ions. Thus, it can vary significantly from the neutral ensemble. However, most common ion sources show long residence times of the analyte in the ion source leading to post ionisation formations.[27, 63] In contrast to the analyte ionisation, operating the reagent ion formation (methane (2-6), hydrogen (11-21)) under kinetic control leads to incomplete conversion. Thus, the reagent consists of a distribution of multiple ionic as well as metastable species. Reactions of the analyte with this variety of reagent species can produce different ions over various reaction pathways leading to more complex mass spectra.

1.4 Protonation capacity

For analytical applications, it is often necessary to ionise a large number of analytes at the same time as well as detecting trace compounds in the presence of large excesses of other analytes. For this purpose, a high protonation capacity (PC), defined as the total mixing ratio of analytes, which can be protonated and quantified with the source, is required.

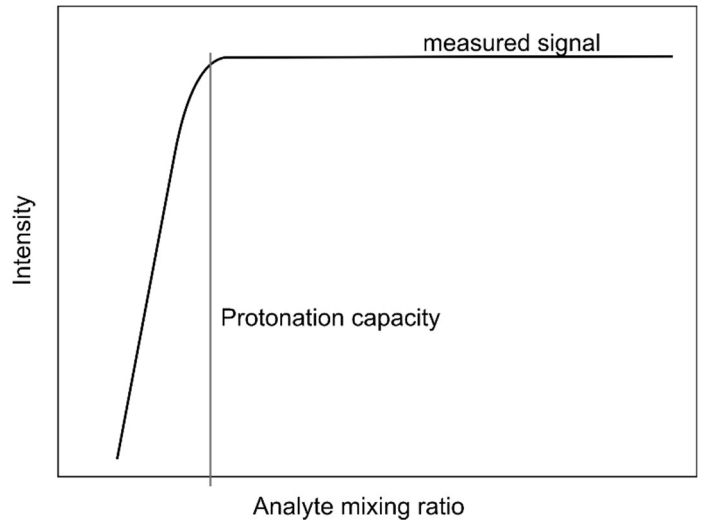

Figure 1.4: Example of the protonation capacity determination.

One approach of measuring the protonation capacity is to determine the linear dynamic range of a protonated analyte and plot the $[M+H]^+$ signal intensity as a function of the neutral mixing ratio (Figure 1.4). By increasing the mixing ratio, the slope of the resulting initially linear response starts to level off at a certain point. This specific mixing ratio is equivalent to the protonation capacity if the ion transfer optics, provided the analyser and the detector still operate in their specific linear range. Thus, the protonation capacity reflects the upper limit of the total analyte mixing ratio quantification.

1.5 Protonation ratio

The protonation ratio (PR) is defined as the ratio of the signal intensity of the protonated molecule and the sum of the signal intensities of the protonated molecule and the radical cation.

$$PR = \frac{[M+H]^+}{[M]^+ + [M+H]^+} \quad \text{(eq.2)}$$

If $[M]^+$ and $[M+H]^+$ are the only ion signals of an analyte, equation 2 yields the protonation ratio of the setup. Since the analyte determines the PR, substance characteristics can influence it. One of these properties is the ratio of fragmentation occurring upon ionisation with a selected reagent via different parallel pathways, e.g., protonation vs charge transfer. On the one hand, if the analyte fragments due to highly exothermal proton transfer, the determined PR is underestimated. On the other hand, if fragmentation is a result of electron transfer, the resulting PR overestimates the extent of protonation.

2 Objectives

As outlined in the introduction, a mixture of analytes can be ionised simultaneously under kinetic control, resulting in an ion distribution, which more or less resembles the neutral ensemble. For example, atmospheric degradation experiments can be monitored and even highly reactive species are detectable with a mass spectrometer, provided appropriate inlet systems are available.

Molecular mass information is essential for the identification of analytes in a mixture. Furthermore, low extents of fragmentation result in simpler mass spectra. Given the option to adjust the excess energy deposited in a generated ion, chemical ionisation in principal provides this opportunity.

This work aims to combine these two features in a CI-based ion source by establishing highly kinetically controlled proton transfer ionisation routes.

2.1 Micro-plasma

Closely linked to the development of a Fourier transform (FT) ion trap mass spectrometer (iTrap®)[64] in collaboration with the Carl Zeiss SMT GmbH (Oberkochen, Germany), Plasma Applications Consulting GmbH & Co. KG (PAC) developed a micro (µ) plasma source operated with helium as reagent gas. This source is built for operating in a vacuum system offering filament-free ionisation approaches. For validation experiments, this source was modified to operate in the first pressure reduction stage of a time of flight (TOF) MS at 1 mbar. Under these conditions, the number of collisions is sufficient for helium metastable species to

most likely react with bulk gas (i.e., the reagent) instead of directly ionising the analyte, which is present in trace amounts. Using hydrogen as reagent gas, mainly protonated analyte molecules are observed.

From these initial experiments, the first configuration to investigate a chemical ionisation source operating with high kinetic control emerged. This setup is characterised and modified further for higher protonation ratios and better control of the prevailing rather complex ion-molecule chemistry.

2.2 Micro-plasma induced chemical ionisation (μ-plici) with stacked chamber system

For monitoring atmospheric degradation experiments, a micro-plasma induced chemical ionisation (μ-plici) source is constructed to provide a highly kinetically controlled ion production and minor fragmentation. It can, therefore, deliver molecular mass and neutral distribution information. This source was mounted on a SCIEX API 3200 triple quadrupole mass spectrometer in order to investigate the modification of an atmospheric pressure (AP) sampling MS with the low-pressure μ-plici ion source. The ion source generates helium metastables in a plasma, to form H_3^+ ions in a hydrogen atmosphere. H_3^+, as one of the most potent gas-phase acids, is used as reagent ion protonating the analyte. To minimise fragmentation, no significant electric field gradient should be present in the analyte ionisation region.

For the interpretation of the signals recorded with this source, the chemistry in each step of the reaction cascade is investigated and ideally driven to a well-defined product distribution to have full control of the ionic species built from the analyte. Physically dividing the reaction cascade into different chambers allows the optimisation of each step individually.

Finally, different reagents are investigated as an intermediator between H_3^+ and the analytes reducing the excess energy and thus, fragmentation.

3 Experimental

In the following, the experimental setups and conditions are presented, including all versions of the developed ion sources with typical parameter sets.

3.1 Micro-plasma source

The micro-plasma source (µ-PS) used in this work was designed and built by the Plasma Applications Consulting GmbH & Co. KG (PAC, Bochum, Germany). It was initially designed to operate in a high vacuum system for hyphenation with an FT quadrupole ion trap (QIT). For this purpose, the plasma source is optimised for low volume flows and small plasma size. The plasma ignites with a direct current (DC) potential between a rod electrode and an aperture. The aperture serves as the counter-electrode for the plasma and represents an interface to the vacuum system. The electrodes are arranged in a ceramic cased chamber, and the discharge is limited to 10 mA with a typical voltage of ± 200 – 400 V. A helium metastables enriched effluent exits the PS and represents the primary ionisation source in this setup.

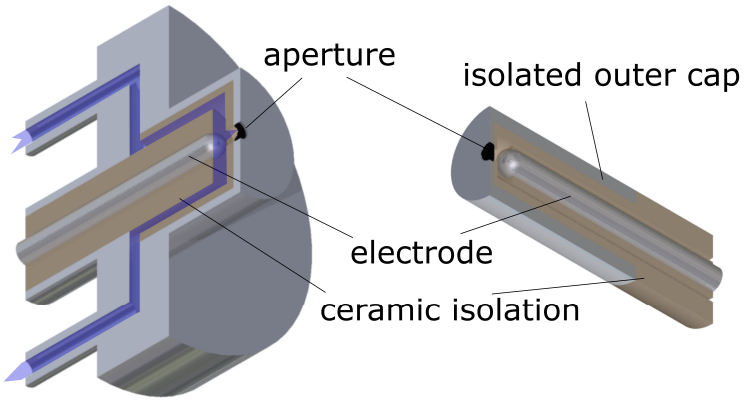

Figure 3.1: Schematic drawing of the front-end of the micro-plasma sources, version 1 (left) and version 2 (right).

In the original design, a continuous helium flow flushed the plasma source, and a portion was directed through the aperture. The majority of the flow was passing through the plasma source to minimise contamination effects (Figure 3.1). The source pressure was in the range of 500 – 1000 mbar and the aperture had an inner diameter of 10 µm. The combination of the helium flow and the small aperture loaded the vacuum system with only a minor flow while the plasma source was kept clean by the main helium flow.

For the following measurements, the original design was changed regarding the gas flow as well as the aperture size. In comparison to the high vacuum application mentioned above, the new plasma source operates in the low mbar range. Therefore, a 100 µm aperture replaces the small one allowing for a higher metastable enriched flow through it. The flow system can be adjusted because impurities can easily leave the source through the aperture. Thus, no continuous flushing of the source is required, and the total helium flow entering the source is directed through the aperture. In this application, the pressure inside the plasma source varies between 100 mbar and over 1700 mbar, depending on the actual helium flow.

Based on this first plasma source design, a second generation was built with a significantly smaller front-end size (Figure 3.1). This design features an isolated cap allowing to choose the reference voltage of the plasma.

3.2 MS Setups

In this work, six ion source configurations were investigated. These arrangements are divided into two groups depending on the MS system for which they were designed. The first ion sources, which are designed based on the plasma source geometry, were implemented into the first pressure reduction stage of a compact time of flight mass spectrometer CTOF (TOFWERK, Thun, Switzerland). Exploring the prospects of modifying an AP-MS to sample from significantly lower pressure, the other ion sources were developed based on the MS inlet of an API 3200 triple quadrupole MS (AB Sciex, Framingham, MA, USA).

3.2.1 CTOF time of flight mass spectrometer

In the beginning of this work, a CTOF with a custom-designed ion transfer stage, as depicted in Figure 3.2 was used. The MS has a mass range of 1 – 4000 Da and a resolution of about 1000. The spectrometer was built as a validation system for the FT-QIT mentioned above. The plasma source was placed in the first pressure reduction stage (approximately 1 mbar) used as the ionisation chamber between two apertures, the sampler (a) and skimmer (b) (Figure 3.2). In addition to the plasma source, a Nd:YAG laser (Spectron Laser Systems, Warwickshire, UK) and an Electron Beam Excimer Lightsource (EBEL) (Photonion GmbH, Schwerin, Germany) were used for several investigations. Therefore, the chamber was equipped with two windows. Their mountings are compatible with KF40 vacuum connections. A third port, which was used for the plasma source connection (c), was placed on the top side. An arrangement of a tube lens (d), a filter orifice (e), and an Einzel lens (g) focus the ions exiting the skimmer. The plasma source ionises a wide range of analytes, including the bulk gas. To reduce adverse overloading with bulk gas ions, the MS was equipped with a notch filter (f) allowing selective discrimination of up to four different m/z values. This

discrimination is essential because the amount of bulk gas ions exceeds the amount of desired analyte ions by more than four orders of magnitude.

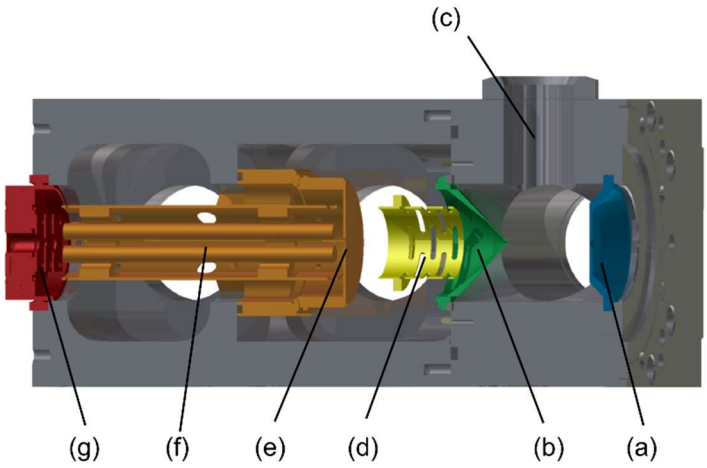

Figure 3.2: Cross-section of the ion transfer stage of the CTOF; a) sampler, b) skimmer, c) connection for plasma source, d) tube lens, e) filter orifice, f) notch filter, g) Einzel lens. [65]

The analyte is sampled into the pressure reduction stage through a 0.3 mm aperture called sampler (a). The sample flow rate is determined by the pressure of the chamber from which the analyte is sampled. The orifice of the sampler can be placed in two positions influencing the transfer length to the skimmer. Previous measurements showed that positioning the orifice farthest away from the skimmer aids to maintain the optimum pressure in the transfer stage while using hydrogen as a bulk gas. Thus, the sampler was used in this position for all applications of this work. To allow sampling of hydrogen as bulk gas, the first pressure reduction stage was equipped with a TriScroll 600 pump (Agilent Technologies Santa Clara, USA) with a pumping speed of 500 L/min. Additionally, a SH-110 scroll pump (Agilent Technologies, Santa Clara, USA) was used as the fore pump of the turbopump keeping the pressure in the drift region of the analyser below 10^{-6} mbar.

3.2.2 API 3200 triple quadrupole mass spectrometer

To verify the possibility of modifying an AP-MS to low-pressure sampling and to couple a helium µ-plasma driven H_3^+ based CI source to it, an API 3200 triple quadrupole was selected. The triple quadrupole instrument provides a means to fragment selected ions intentionally obtaining structural information. In this work, the collision cell was used for the identification of different clustered species. For coupling of the ion source to the MS, the curtain plate (a) of the instrument was removed and the first skimmer (b) was enlarged from 0.3 mm up to 2 mm orifice diameter (Figure 3.3). The exhaust of the conventional AP ion sources, as well as the curtain gas was not needed and consequently sealed. The µ-plici source was adapted to fit directly onto the ceramic surface of the orifice plate, surrounding the skimmer. An additional vacuum pump (Edwards, Crawley, UK) had to be attached to the ion source to take the main gas load off the MS vacuum system. This pump is required as the AP-MS is not designed for higher amounts of helium or hydrogen in the sampled gas mixture.

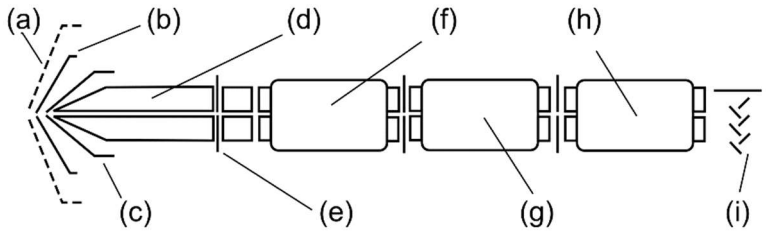

Figure 3.3: Schematic drawing of the ion optics of the API3200 triple quadrupole instrument; a) curtain plate (removed), b) outer skimmer, c) second skimmer, d) quadrupole 0 (sampling quadrupole), e) first lens, f) quadrupole 1 (scanning mode), g) LINAC® collision cell (quadrupole 2), h) quadrupole 3, i) detector with deflector.[66]

On the one hand, the increased inner diameter of the skimmer allows sampling of higher amounts of gas. On the other hand, pressure interlocks in the system limit the composition of the gas used. For most measurements, the MS was operated in the so-called Q1-only mode, in which the first quadrupole scans the selected mass range (usually 10 – 200 $^m/_z$). In contrast to the commonly used APCI and ESI sources, no high voltage is present in the ion source. Additionally, the second skimmer is connected to the instrument ground and cannot be isolated. Thus, no

voltage can be applied. Consequently, the voltages on the first skimmer as well as the entrance potential (EP) on the sampling quadrupole are restricted to rather low values (0 – 5 V). Otherwise, no signal is observed at all.

3.3 Ion sources for the CTOF

The objective of this work was the development of a CI ion source for the API 3200 triple quadrupole instrument. Nevertheless, the initial approach for this ionisation method was based on measurements with the CTOF instrument while operating a free arrangement setup of the µ-plasma source. In addition to the new source development, this free arrangement setup was optimised. In the following section, the different versions of ion sources for the CTOF are presented concerning their physical properties and dimensions.

3.3.1 "free" arrangement setup

For validation measurements between the FT quadrupole ion trap and the CTOF with custom-designed ion transfer stage, the µ-plasma source developed by PAC was placed perpendicular to the analyte gas stream entering the first pressure reduction stage of the CTOF (Figure 3.4). The exit of the plasma source (orifice with 100 µm inner diameter) was placed 15 mm above the axis between skimmer and sampler. Thus, the volume flows were assumed to mix in the centre of the chamber, leading to ionisation of the analyte. The plasma source pressure (150 – 400 mbar), has a high impact on the mode and the volume of the plasma plume inside the ion source. Depending on the helium flow through the plasma source, the plasma afterglow was also present outside of the source as is depicted in Figure 3.4. The analyte was sampled through a 300 µm aperture (sampler) from a pressure-controlled volume. Depending on the bulk gas, the pressure varied between 200 – 1000 mbar. Usually, the analyte flow rate was in the range of 70 – 100 sccm. The TriScroll pump was connected to both sides of the chamber symmetrically to the skimmer so that the analyte gas stream was not deflected. The high pumping rate in combination with the limited flow through the sampler and the 100 µm aperture of the plasma source allowed the ionisation chamber pressure

to be in the range of 0.5 mbar to 1 mbar. The distance between sampler and skimmer was 30 mm.

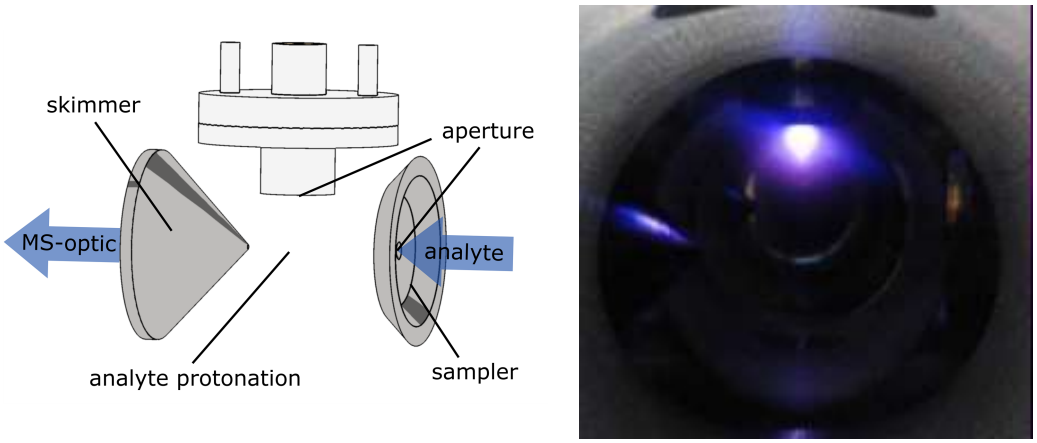

Figure 3.4: Free arrangement setup, left: schematic of the plasma source arrangement inside of the first reduced-pressure stage of the CTOF; right: picture of the plasma in operation.

The metastable helium atoms most likely produce reagent ions from the bulk gas instead of ionising the analyte directly, because of its low mixing ratio. Thus, with nitrogen as bulk gas, N_2^+ and N_4^+ are formed while H_3^+ is generated with hydrogen. The nature of the observed analyte ions relied on the used bulk gas; protonated ions are observed when hydrogen is used as the bulk gas.

3.3.2 Cage arrangement setup (optimised free arrangement setup)

As optimisation of the free plasma source arrangement, the first pressure reduction stage of the CTOF was redesigned by PAC. A new analyte inlet and a cage electrode were implemented in the ionisation chamber. This setup is built to provide a seeded plasma in front of the skimmer and is meant to lead to an ion source design for coupling with the FT-QIT. In addition to these changes, a new generation of the plasma source is used, which allows the application of a voltage onto the exit cap. This additional voltage can be used to increase the sampling efficiency of the mass spectrometer.

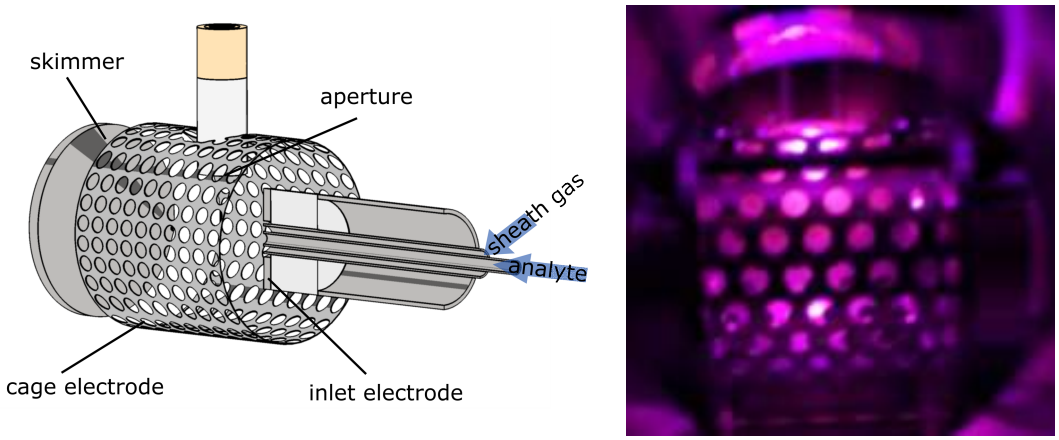

Figure 3.5: Cage arrangement setup with a coaxial gas inlet, left: schematic drawing; right: picture of the setup in operation.

As a result of the implementation of the 100 µm aperture in the plasma source, the afterglow of the primary plasma constituents can significantly exit the source. By applying selected voltages and gas flows, a secondary plasma ignites outside the plasma source. This secondary plasma is fed by the electrons and metastable species of the primary plasma in combination with the voltages in the analyte ionisation region. This so-called seeded plasma extinguishes when either the voltages inside the ion source or the primary plasma is turned off. The electric field gradient required (approximately 1 V/cm) to sustain the seeded plasma is significantly lower compared to a primary plasma present in this region. Thus, the ionisation is expected to provide less fragmentation from the collision-induced dissociation (CID) pathway. The cage electrode enables allocation of a reference voltage other than the ground potential applied to the housing of the ionisation source. The plasma source was operated at different pressures reaching from 150 mbar to 700 mbar depending on the desired operation mode of the ion source. For a seeded mode, the pressure inside the plasma source had to be lower than for a mode, where the primary plasma expands into the ion source.

The new inlet provides a sheath gas flow coaxial to the analyte flow. The front end of this tube is isolated so that an electric potential can be applied. The sheath gas is added to establish a constant plasma performance by stabilising the fluid dynamic properties of the source. Thus, the plasma performance, as well as the

chemistry inside the source, is dictated by the sheath gas. It is therefore independent of the analyte gas flow, which can be continuous or pulsed and of different composition. The sheath gas varies between 10 sccm and 100 sccm or is sampled from 1 bar pressure of pure helium or nitrogen or a mixture of hydrogen diluted in helium. In the latter case, the sheath gas can provide protonating conditions. The analyte flow is varied between 10 and 70 sccm in continuous mode. In pulsed mode, the pulse duration varies between 20 ms and 5 s.

3.3.3 µ-plici 1.0

Similar to the sheath flow inlet of the cage arrangement setup, the plasma source was modified to maintain a protonation in nitrogen or other non-hydrogen background gases by utilising H_3^+ as reagent ion. Downstream of the 100 µm aperture of the source, a T-piece arrangement is mounted. This allows the addition of a reagent gas as close as possible to the metastable enriched plasma effluent.

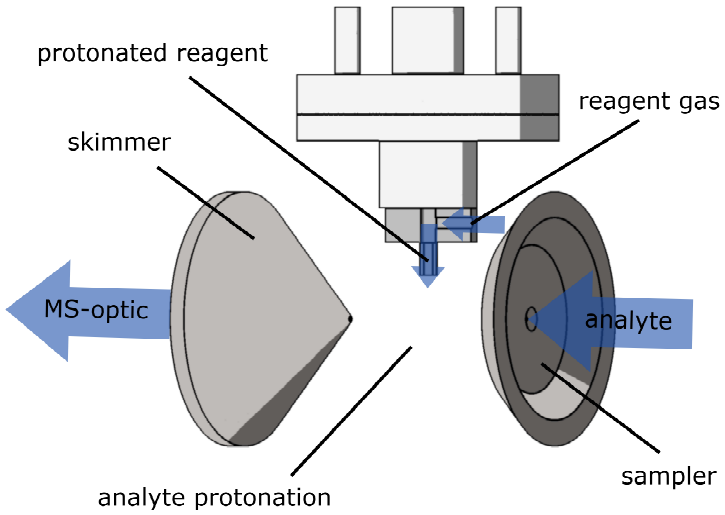

Figure 3.6: Schematic drawing of the µ-plici 1.0 ion source inside the first pressure reduced stage of the CTOF.

Thus, reagent ions are formed inside the T-piece separate from the analyte ion protonation. The T-piece arrangement allows assembly of a gas chromatograph (GC)-column. An uncoated GC-column with an inner diameter of 0.5 mm and a

length of 6 mm was used to restrict the flow from the reagent ionisation region. Thus, the pressure was increased, and separation between plasma and ion source was achieved. As reagent gas, helium, hydrogen or a mixture of both were used, and the flow rate varied between 0 and 85 sccm. For various investigations, typical flow parameters for the plasma source, the reagent gas flow, and the analyte flow were 70 sccm, each. While helium leads to analyte ion species resulting from charge transfer (CT) reactions, hydrogen produces H_3^+ reagent ions and generates proton transfer (PT) products.

3.4 Ion sources for the API 3200

The ion sources developed for the API 3200 triple quadrupole instrument are based on the same plasma source design and followed the idea of sequencing the reaction cascade as described above. In contrast, they implement an axial arrangement of the plasma source concerning the skimmer and a perpendicular addition of the reagent and analyte gas flows. The ion sources are plugged directly on the ceramic of the orifice plate of the MS and are sealed with an O-ring to the ceramic plateau of the plate, surrounding the skimmer. This allows the sources to operate at reduced pressure.

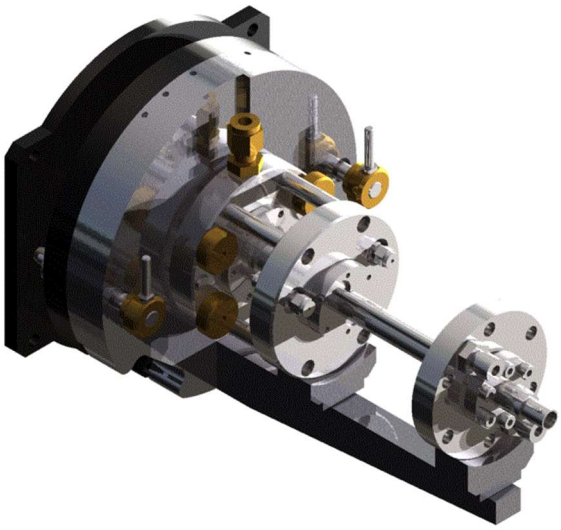

Figure 3.7: Setup of the µ-plici 2 system with fittings mounted on the API 3200 MS.

The mounting base for the ion sources, which is required to ensure proper sealing, was designed to provide access to the controlled gas flows of the standard ion sources (Figure 3.7). The following ion sources are improved iteratively in accordance with the results of the corresponding experimental results. The overall design, a stacked system, was conserved while the inner composition of the ion sources develops from iteration to iteration.

3.4.1 µ-plici 2.0 – flow tube system

The first ion source design made for the AP-MS instrument is µ-plici 2.0 (Figure 3.8). The source design is based on the three-way arrangement (µ-plici 1.0; cf. chapter 3.3.3). To enhance the ion sampling efficiency of the MS while sampling from reduced pressure, the skimmer orifice is enlarged from 0.3 mm up to 1 mm in diameter. As reagent gas, hydrogen or a mixture of hydrogen in helium or argon is used and added directly behind the aperture of the plasma source. In the following tube (inner diameter 1.5 mm, length 9 mm), the H_3^+ ions are produced. The H_3^+ enriched helium/argon/hydrogen gas flow is then mixed with the analyte gas added perpendicularly into the protonation region (inner diameter: 4 mm; distance between reagent tube and skimmer: 35 mm). The gas mixture is directed towards the skimmer, and excess gas is removed symmetrically through an annular space with an oil diffusion pump (Edwards, Crawley, UK). The pressure maintained with this setup could not be measured directly inside the protonation tube. Instead, it is estimated to exceed 20 mbar based on measurements downstream between the source and the pump. The exchange time of the gas is calculated to be 2.6 ms based on a pressure of 20 mbar and an overall gas flow of 200 sccm. Thus, the maximum number of collisions of an analyte ion is approximately 50000, resulting in virtually no kinetic control (see chapters 1.3.2 and 4.1). The recorded mass spectra verify this behaviour.

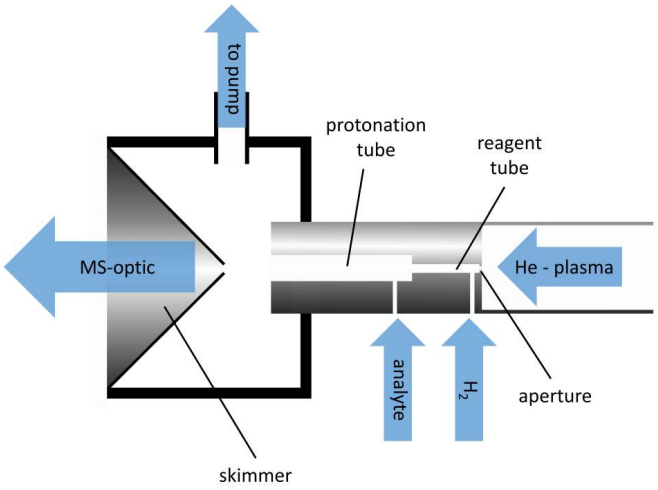

Figure 3.8: Schematic drawing of the µ-plici 2.0 setup with indicated flows.

The second skimmer, as well as the ion source, are grounded, restricting the first skimmer to positive voltages. As a result, the ions either have to overcome the electric field gradient, or the first skimmer has to be operated at 0 V. The distance between the 100 µm aperture of the plasma source and the skimmer is 45 mm and the pressure is assumed to decrease steadily over this length.

Since this setup provides virtually no kinetic control due to the high pressure in the analyte ionisation tube, a new iteration of the source is built. Also, helium metastables are probably transformed insufficiently into H_3^+ reagent ions. Thus, the separation between the plasma and the analyte ionisation had to be improved. Additionally, a possible backflow of analyte bulk gas into the reagent tube needs minimisation.

3.4.2 µ-plici 2.1 – chamber system

To improve the previous source, the regions of reagent ion formation and analyte ionisation are separated by an aperture of 200 µm inner diameter. This creates a reagent chamber of 1.5 mm inner diameter and 9 mm length and allows reduction of the pressure inside the analyte ionisation region. Thus, a backflow effect should be minimised, resulting in higher protonation ratios. The conical shape of the analyte ionisation chamber allows further decreasing the pressure. For a higher

ion sampling, the source is equipped with a ring electrode, operating as a repeller, at the exit of the analyte ionisation chamber. In µ-plici 2.0, the pumping rate of the source was restricted by the connection between the pump and the source. To increase the pumping rates, the PEEK element was reshaped to electrically isolate the ring electrode and the source against the housing. Consequently, lower pressures are reached at the expense of the symmetric pumping.

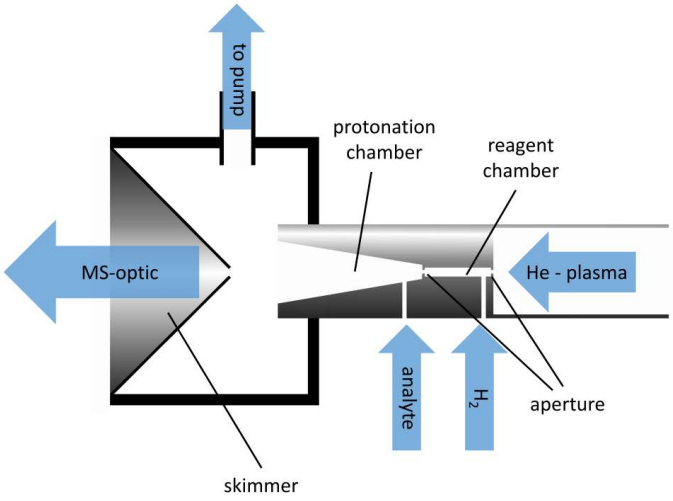

Figure 3.9: Schematic drawing of the µ-plici 2.1 setup with chamber system and indicated flows.

At the ring electrode, voltages of up to 4 V are supplied, which allows the skimmer to be operated at slightly higher voltages in comparison to the µ-plici 2.0 source. In addition to the improved separation of reagent ion production and analyte ionisation, the hydrogen flow can be decreased as a result of implementing the aperture. Additionally, the pressure inside the reagent chamber is increased due to the limitation of effluent caused by the aperture.

The second aperture, separating the plasma source and the reagent chamber, is decreased from 100 µm to 50 µm to lower the helium flow while maintaining a constant pressure inside the plasma source. Although the amount of helium metastable is expected to decrease, the smaller aperture offers several advantages. First, a backflow of hydrogen into the plasma source is minimised. Second, the influence of the primary plasma inside the reagent chamber is reduced to allow

the application of other reagents such as methane. As a result of lower helium and hydrogen flow rates, the protonation chamber pressure is decreased, and the inner diameter of the skimmer can be increased up to 2 mm, improving the sampling efficiency.

The pressure in the protonation chamber of this setup is 10 – 15 mbar. Although the pumping rate is increased in comparison to µ-plici 2.0, the extent of kinetic control could not be improved, in contrast: The exchange time inside the reagent chamber is calculated to be 570 µs for a pressure of 100 mbar and a flow rate of 100 sccm helium and 5 sccm hydrogen. The exchange time inside the protonation chamber is 11.4 ms with a pressure of 10 mbar and a total flow rate of 200 sccm, resulting in a total number of collisions of approximately 100000.

Table 2: Comparison of the number of collisions between different µ-plici versions.

	Reagent region			Ionisation region			
	Pressure [mbar]	Flow [sccm]	Time [ms]	Pressure [mbar]	Flow [sccm]	Time [ms]	Collisions
µ-plici 2.0	-	-	-	20	200	2.6	50000
µ´plici 2.1	100	105	0.57	10	200	11.4	100000

For a better overview, these results are summarised in Table 2. Although the pressure in the analyte ionisation region could be reduced, the degree of kinetic control decreases. The significantly increased volume causes this due to the conical shape.

To improve the kinetic control in the analyte ionisation region, a new version is built with a smaller volume but all improvements in pumping rate. Additionally, the downscaling of excess energy by using other reagents than hydrogen proved difficult due to fragmentation of, for example, methane in the reagent chamber. Thus, a new strategy is pursued, passing protons from H_3^+ to other reagents. This way, the extent of fragmentation is more controllable.

3.4.3 µ-plici 2.2 - stacked chamber system

With µ-plici 2.2, the stacked chamber system is implemented, adding an additional chamber between the reagent chamber and the protonation chamber. In this work, the first chamber is used with pure hydrogen as the primary reagent gas. Further reagents can be added via the additional secondary reagent chamber.

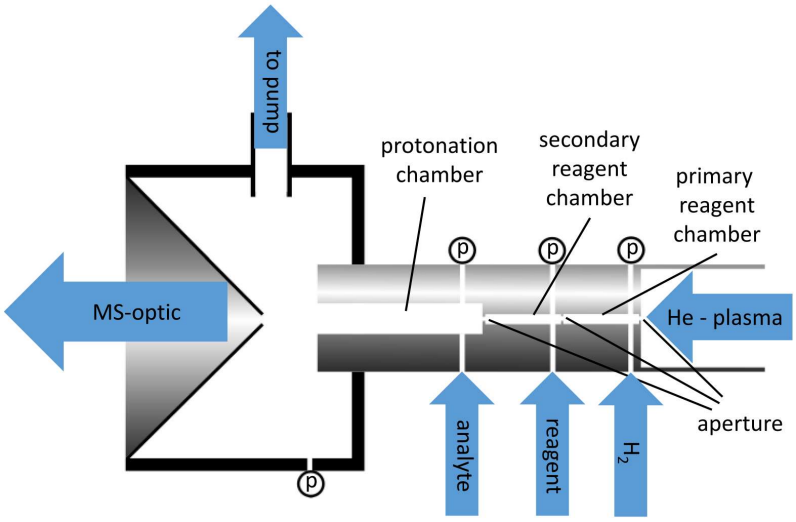

Figure 3.10: Schematic drawing of the µ-plici 2.2 with stacked chamber system and indicated flows; positions for pressure measurements are marked with "p".

The apertures are changed to 60 µm between the plasma source and the primary reagent chamber, 150 or 200 µm between the primary and the secondary reagent chamber and 200 µm between the secondary reagent and the protonation chamber. The sizes of the primary and secondary reagent chamber are identical to the reagent chamber of the prior design with a length of 5.6 mm and an inner diameter of 1.5 mm. The statical pressure can be monitored in each chamber via an additional inlet port. With this modular design, the protonation chamber can be exchanged. Two versions are made with inner diameters (ID) of 4 mm and 8 mm to establish different reaction times. To reduce charging effects of the PEEK element, and to reduce the volume of the protonation chamber, the cylindrical form of this chamber was restored, and the PEEK surface is in no contact with the ions. Also, this decrease in size results in shorter reaction times. For a lower pressure in the protonation chamber and, thus better kinetic control, the diameter of the pumping tube is increased further. For comparison of "hydrogen-only"

measurements, the secondary reagent chamber can be removed receiving a two-chamber system, analogous to µ-plici 2.1. Typical reaction times are 1.2 ms in the primary reagent chamber, 600 µs in the secondary reagent chamber, and 170 µs (ID 4 mm) or 670 µs (ID 8 mm) in the protonation chamber. Typical pressures are 200 mbar in the primary reagent chamber, 100 mbar in the secondary reagent chamber and 1 – 3 mbar in the protonation chamber. Reagents can be used to chemically suppress the formation of bulk gas ions such as nitrogen or water-related ions. The suppression of the water-related ions can provide a higher number of reactive reagent ions available for analyte protonation.

3.5 Ion current measurements

Ion current measurements were carried out to determine total ion currents independent of the mass discrimination of an ion transfer. For this purpose, an adapter was built to couple the ion source to a KF type flange equipped T-piece. The second port of the T-piece is used for pumping, and the remaining one is equipped with a movable electrode. Thus, the ion current can be measured with axial resolution. The electrode is made of a glass capillary with an outer diameter of 6 mm. A net is mounted on top of this capillary, and the electric connection is maintained through the capillary.

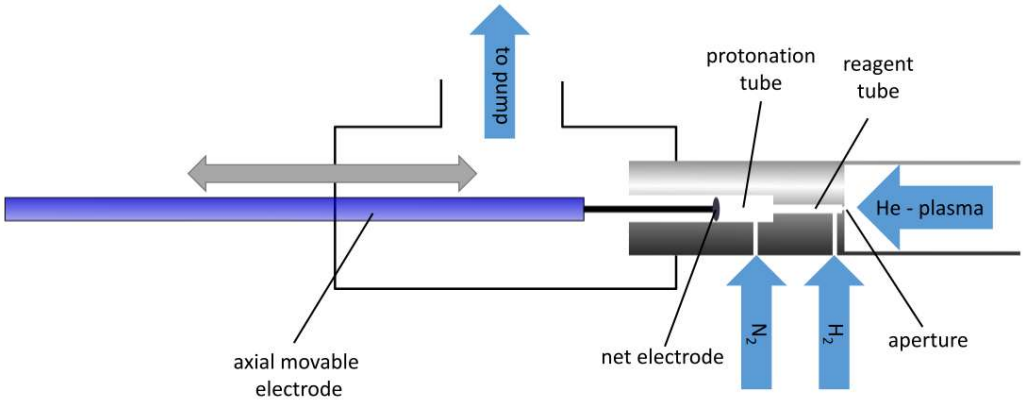

Figure 3.11: Schematic drawing of the ion current measurement setup with µ-plici 2.0 ion source and indicated flows.

Gas flows as well as pressures can be adjusted similar to the source being mounted on the MS. The ion currents are measured with an electrometer (6430 Sub-Femtoamp Remote SourceMeter, Keithley Instruments, Cleveland, USA). For a time-resolved diagram, the ion current data were collected with custom software with a temporal resolution of 1 s.

3.6 Kinetic simulations

For the understanding of the chemical processes in the source, their kinetics is simulated with the open-source program package Cantera [67] as differential equation solver. The simulations were made with the isotherm, isobar reactor model, in which each chamber is simulated separately. Depending on the specific chamber simulated, the reaction cascade (3-23) is used. The corresponding rate constants are listed in Table 3.

Table 3: Rate constants used for the kinetic simulations; B = benzene, T = toluene, X = xylene.

Reaction			Rate constant
Initial charge generation			
$He^M + H_2$	→	$H^+ + He + H$	$8.30 \cdot 10^{-14}$ [$cm^3 molec^{-1} s^{-1}$]
$He^M + H_2$	→	$H_2^+ + He$	$1.70 \cdot 10^{-14}$ [$cm^3 molec^{-1} s^{-1}$]
$He^M + H_2$	→	$HeH^+ + H$	$2.00 \cdot 10^{-12}$ [$cm^3 molec^{-1} s^{-1}$]
$He^M + H_2O$	→	$H^+ + He + OH$	$1.80 \cdot 10^{-10}$ [$cm^3 molec^{-1} s^{-1}$]
$He^M + H_2O$	→	$H + He + OH^+$	$2.50 \cdot 10^{-10}$ [$cm^3 molec^{-1} s^{-1}$]
$He^M + H_2O$	→	$H_2O^+ + He$	$5.50 \cdot 10^{-10}$ [$cm^3 molec^{-1} s^{-1}$]
Reagent ion formation			
$H^+ + H_2$	→	H_3^+	$1.30 \cdot 10^{-16}$ [$cm^3 molec^{-1} s^{-1}$]
$H_2^+ + He$	→	$HeH^+ + H$	$1.40 \cdot 10^{-10}$ [$cm^3 molec^{-1} s^{-1}$]
$H_2^+ + H_2$	→	$H_3^+ + H$	$2.00 \cdot 10^{-9}$ [$cm^3 molec^{-1} s^{-1}$]
$HeH^+ + H_2$	→	$H_3^+ + He$	$1.77 \cdot 10^{-9}$ [$cm^3 molec^{-1} s^{-1}$]
$H_3^+ + N_2$	→	$N_2H^+ + H_2$	$1.63 \cdot 10^{-9}$ [$cm^3 molec^{-1} s^{-1}$]
$N_2H^+ + H_2O$	→	$N_2 + H_3O^+$	$2.60 \cdot 10^{-9}$ [$cm^3 molec^{-1} s^{-1}$]
$H_3^+ + H_2O$	→	$H_2 + H_3O^+$	$4.81 \cdot 10^{-9}$ [$cm^3 molec^{-1} s^{-1}$]
$OH^+ + H_2$	→	$H_2O^+ + H$	$9.70 \cdot 10^{-10}$ [$cm^3 molec^{-1} s^{-1}$]
$H^+ + H_2O$	→	$H_2O^+ + H$	$6.90 \cdot 10^{-9}$ [$cm^3 molec^{-1} s^{-1}$]
$H_2O^+ + H_2$	→	$H_3O^+ + H$	$7.60 \cdot 10^{-10}$ [$cm^3 molec^{-1} s^{-1}$]
$N_2^+ + N_2$	→	N_4^+	$1.76 \cdot 10^{-29}$ [$cm^3 molec^{-1} s^{-1}$]
$N_4^+ + H_2$	→	$H + N_4H^+$	$7.50 \cdot 10^{-13}$ [$cm^3 molec^{-1} s^{-1}$]
$N_4^+ + H_2$	→	$N_2 + H + N_2H^+$	$1.40 \cdot 10^{-9}$ [$cm^3 molec^{-1} s^{-1}$]
Water cluster system			
$H_3O^+ + H_2O + M$	→	$[(H_2O)_2+H]^+ + M$	$6.98 \cdot 10^{-29}$ [$cm^6 molec^{-2} s^{-1}$]
$[(H_2O)_2+H]^+ + M$	→	$H_3O^+ + H_2O + M$	$4.00 \cdot 10^{-27}$ [$cm^3 molec^{-1} s^{-1}$]
$[(H_2O)_2+H]^+ + H_2O + M$	→	$[(H_2O)_3+H]^+ + M$	$6.98 \cdot 10^{-29}$ [$cm^6 molec^{-2} s^{-1}$]
$[(H_2O)_3+H]^+ + M$	→	$[(H_2O)_2+H]^+ + H_2O + M$	$6.78 \cdot 10^{-19}$ [$cm^3 molec^{-1} s^{-1}$]
$[(H_2O)_3+H]^+ + H_2O + M$	→	$[(H_2O)_4+H]^+ + M$	$6.98 \cdot 10^{-29}$ [$cm^6 molec^{-2} s^{-1}$]
$[(H_2O)_4+H]^+ + M$	→	$[(H_2O)_3+H]^+ + H_2O + M$	$2.50 \cdot 10^{-16}$ [$cm^3 molec^{-1} s^{-1}$]
$[(H_2O)_4+H]^+ + H_2O + M$	→	$[(H_2O)_5+H]^+ + M$	$6.98 \cdot 10^{-29}$ [$cm^6 molec^{-2} s^{-1}$]
$[(H_2O)_5+H]^+ + M$	→	$[(H_2O)_4+H]^+ + H_2O + M$	$1.67 \cdot 10^{-13}$ [$cm^3 molec^{-1} s^{-1}$]
$[(H_2O)_5+H]^+ + H_2O + M$	→	$[(H_2O)_6+H]^+ + M$	$6.98 \cdot 10^{-29}$ [$cm^6 molec^{-2} s^{-1}$]
$[(H_2O)_6+H]^+ + M$	→	$[(H_2O)_5+H]^+ + H_2O + M$	$2.06 \cdot 10^{-12}$ [$cm^3 molec^{-1} s^{-1}$]
$[(H_2O)_6+H]^+ + H_2O + M$	→	$[(H_2O)_7+H]^+ + M$	$6.98 \cdot 10^{-29}$ [$cm^6 molec^{-2} s^{-1}$]
$[(H_2O)_7+H]^+ + M$	→	$[(H_2O)_6+H]^+ + H_2O + M$	$1.30 \cdot 10^{-11}$ [$cm^3 molec^{-1} s^{-1}$]
$[(H_2O)_7+H]^+ + H_2O + M$	→	$[(H_2O)_8+H]^+ + M$	$6.98 \cdot 10^{-29}$ [$cm^6 molec^{-2} s^{-1}$]
$[(H_2O)_8+H]^+ + M$	→	$[(H_2O)_7+H]^+ + H_2O + M$	$5.00 \cdot 10^{-11}$ [$cm^3 molec^{-1} s^{-1}$]
$[(H_2O)_8+H]^+ + H_2O + M$	→	$[(H_2O)_9+H]^+ + M$	$6.98 \cdot 10^{-29}$ [$cm^6 molec^{-2} s^{-1}$]
$[(H_2O)_9+H]^+ + M$	→	$[(H_2O)_8+H]^+ + H_2O + M$	$2.11 \cdot 10^{-10}$ [$cm^3 molec^{-1} s^{-1}$]
Analyte ionisation			
$H_3^+ + B$	→	$H_2 + [B+H]^+$	$3.30 \cdot 10^{-9}$ [$cm^3 molec^{-1} s^{-1}$]
$H_3O^+ + B$	→	$H_2O + [B+H]^+$	$1.80 \cdot 10^{-9}$ [$cm^3 molec^{-1} s^{-1}$]
$N_2H^+ + B$	→	$[B+H]^+ + N_2$	$1.50 \cdot 10^{-9}$ [$cm^3 molec^{-1} s^{-1}$]
$H_3^+ + T$	→	$H_2 + [T+H]^+$	$3.30 \cdot 10^{-9}$ [$cm^3 molec^{-1} s^{-1}$]
$H_3O^+ + T$	→	$H_2O + [T+H]^+$	$1.30 \cdot 10^{-9}$ [$cm^3 molec^{-1} s^{-1}$]
$N_2H^+ + T$	→	$[T+H]^+ + N_2$	$1.30 \cdot 10^{-9}$ [$cm^3 molec^{-1} s^{-1}$]
$H_3^+ + X$	→	$H_2 + [X+H]^+$	$3.30 \cdot 10^{-9}$ [$cm^3 molec^{-1} s^{-1}$]
$H_3O^+ + X$	→	$H_2O + [X+H]^+$	$2.30 \cdot 10^{-9}$ [$cm^3 molec^{-1} s^{-1}$]
$N_2H^+ + X$	→	$[X+H]^+ + N_2$	$1.00 \cdot 10^{-9}$ [$cm^3 molec^{-1} s^{-1}$]
$B+H^+ + X$	→	$[X+H]^+ + B$	$1.00 \cdot 10^{-9}$ [$cm^3 molec^{-1} s^{-1}$]
$B+H^+ + T$	→	$[T+H]^+ + B$	$1.00 \cdot 10^{-9}$ [$cm^3 molec^{-1} s^{-1}$]
$T+H^+ + X$	→	$[X+H]^+ + T$	$1.00 \cdot 10^{-9}$ [$cm^3 molec^{-1} s^{-1}$]

3.7 DIA, ion current and transfer time measurements at the CTOF

The transfer time, the ion currents, and the distribution of ion acceptance (DIA)[68] were investigated in the CTOF ion source setup (Chapter 3.3). To determine these two parameters, a laser system (Nd:YAG Spectron SL 401, Spectron Laser Systems, Warwickshire, UK) was mounted on the MS. By adding a gas flow containing 400 ppm_V toluene in nitrogen, the distribution of ion acceptance (DIA) can be measured by focusing the laser to 1 mm^2 and summing the toluene signals over a constant time for each laser position. A heat map of the region visible for the MS accrues by scanning the whole ion source, as indicated in Figure 3.12. The DIA depends on both, sample efficiency at the measured position and the distribution of the neutral analyte inside the source.

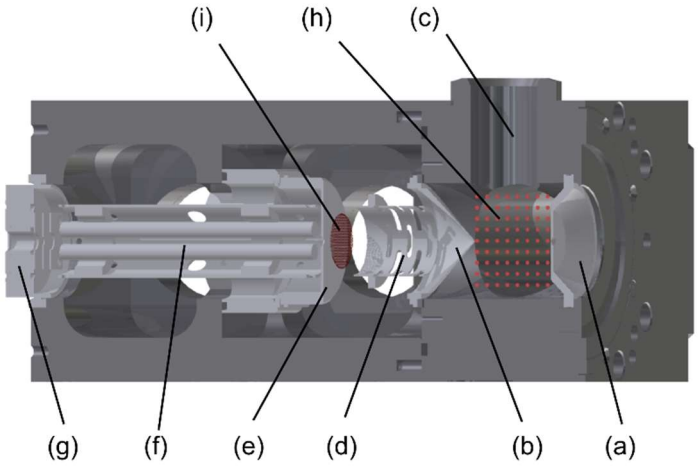

Figure 3.12: Schematic setup for DIA, ion current and transfer time measurements at the CTOF; a) sampler, b) skimmer, c) connection for plasma source, d) tube lens, e) filter orifice, f) notch filter, g) Einzel lens, h) ionisation pattern for DIA measurements, i) mesh electrode inside the ion transfer (for ion current measurements and as gate for ion transfer time measurements).

For the investigation of the transfer time through the first pressure reduction stage of the CTOF, a mesh electrode (i) is implemented into the ion transfer between tube lens (d) and filter orifice (e). By triggering the voltage applied to the mesh electrode with a fast high voltage transistor switch (Behlke Power Electronics GmbH, Kronberg im Taunus, Germany), the ion signal produced by one laser pulse can be gated. For a processible signal, the intensity of the toluene signal was

summed over 30 seconds. The ion transfer is blocked by the mesh electrode (i) for a 1 ms period, which was delayed to the laser pulse in 5 µs steps (Figure 3.13). Thus, the transfer time between the laser position and the mesh electrode is measured. Between 3 positions (right in front of the skimmer, below the plasma source and right behind the sampler), the transfer time is measured. Based on these data, a reaction time can be estimated.

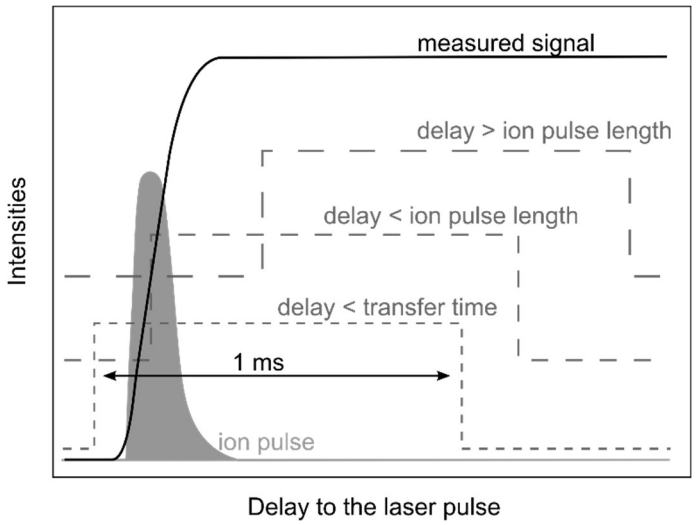

Figure 3.13: Scheme of ion transfer time measurements at the CTOF; Signal overview.

3.8 Analytes

If not stated otherwise, all analytes used were of analytical grade and all gases (Messer Industriegase GmbH, Bad Soden, Germany) of 5.0 grade (99.999% purity). Analytes were sampled from custom mixed gas bottles (labelled 10 ppb or 10 ppm). Exact mixing ratios are given in Table 4. These mixtures were further dynamically diluted using mass flow controllers (MKS Instruments, Andover, USA) into a pressure controlled reservoir (Figure 3.14). The mass spectrometers sample from this reservoir with a constant flow rate, which is restricted by either apertures or capillaries. Reagent gases, as well as the helium for the plasma source, were purified by cooling a tube section with liquid nitrogen or a mixture of acetone and dry ice and were added directly using mass flow controllers.

Table 4: Mixing ratios of the analyte mixtures, quantified by GC-MS.

mixture	toluene "10 ppb"	BTX "10 ppb"	toluene "10 ppm"	BTX "10 ppm"
substance	mixing ratio [ppb_V]		mixing ratio [ppm_V]	
toluene	8.3 ± 0.8	9.4 ± 0.1	4.6 ± 1.0	8.9 ± 0.2
benzene	-	8.2 ± 1.1	-	12.1 ± 0.1
xylene	-	2.6 ± 1.8	-	6.6 ± 0.2

The CTOF utilised with the free arrangement or µ-plici 1.0 samples from the main "mixing chamber" depicted in Figure 3.14. The CTOF equipped with the cage arrangement ion source as well as the triple quadrupole MS sample from the pipe between the mass flow controllers and the "mixing chamber". For a better temporal resolution between changing the mixing ratio and instrumental response, the "mixing chamber" is equipped with additional piping to deliver the analyte gas flow to the MS inlet.

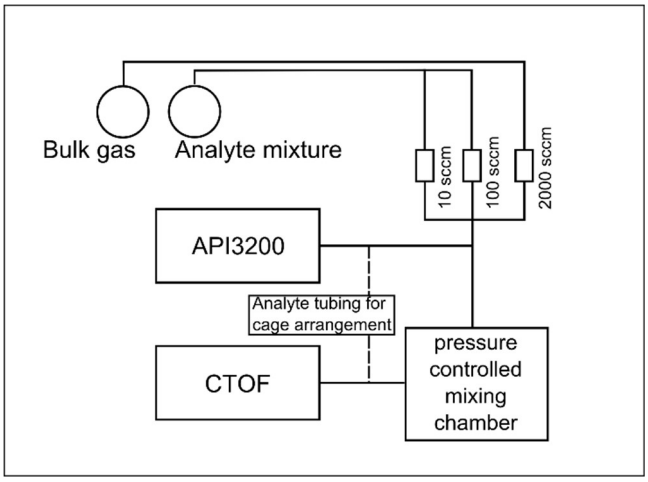

Figure 3.14: Diagram of the gas supply and dilution system with both mass spectrometer attached.

4 Results and Discussion

4.1 Kinetic vs thermodynamic "control"

As mentioned in chapter 1.3.2, different definitions of kinetic control are in use. In contrast, thermodynamic control typically refers to driving reactions until an equilibrium is reached, and no change of the product distribution over time is observed ($dG=0$).[57] Applying this concept to the proton transfer chemistry, thermodynamic control leads to the product with the highest proton affinity. Kinetic control would describe every time step preceding this equilibrium, as is depicted in Figure 4.1. Kinetic control describes not a discrete state within a reaction system, as the thermodynamic control does, and must, therefore, open-source to as high or low kinetic control. It refers to the point on the energy curve in dependence on the progress of the whole system's reaction at which the reaction rates approach zero. Additionally, this point describes how far the ion distribution varies from the neural ensemble.

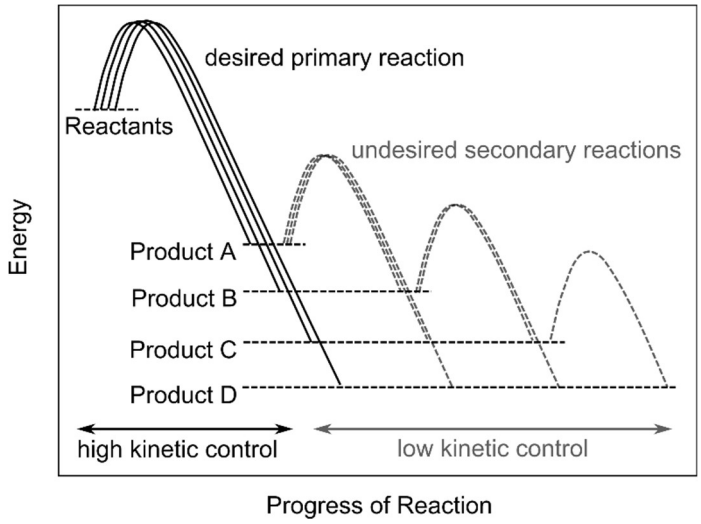

Figure 4.1: Schematic of the kinetic vs thermodynamic control as used in this thesis.

If the pressure and therefore the number of collisions is decreased, post-ionisation reactions of the analyte ions can be prevented. For an ion distribution closely representing the neutral ensemble, analyte ions must not react in any way after protonation, i.e., the analyte protonation step must be as far away from thermodynamic equilibrium as possible. In this case, the ion distribution depends only on the mixing ratio of the analyte and the protonation step rate constants. However, by limiting the number of collisions such far, the sensitivity of the source decreases significantly.

For a better understanding of these process, kinetic simulations are carried out on an exemplary system consisting of benzene (B), toluene (T) and N_2H^+ as reagent ion diluted in nitrogen. This system consists of 3 possible reactions:

$$N_2H^+ + B \rightarrow [B+H]^+ + N_2 \quad (24)$$

$$N_2H^+ + T \rightarrow [T+H]^+ + N_2 \quad (25)$$

$$[B+H]^+ + T \rightarrow [T+H]^+ + B \quad (26)$$

The rate constant of the proton transfer between the two analytes is estimated to $1.00 \cdot 10^{-9}$ $cm^3\,mol^{-1}\,s^{-1}$ since protonation reactions typically occur all in the same region of rate constant values (cf. Table 3).[69] For this investigation, the mixing ratios of benzene and toluene are chosen to be equal to simplify the system further. With a closer look, the deviation depends on the neural distribution, since the rate of reaction (26) strongly depends on the mixing ratio of both analytes.

To quantify the deviation from the "ideal" distribution, simulations were carried out with and without the transfer reaction (26). The ideal distribution is defined as the distribution of the ion signals representing the neutral distribution with consideration of the rate constants. In Figure 4.2, the difference between the ideal slope and the slope with the transfer reaction is evident for high collision numbers. Since the deviation constantly increases from the beginning, no natural turning point can be found for a high kinetic control benchmark.

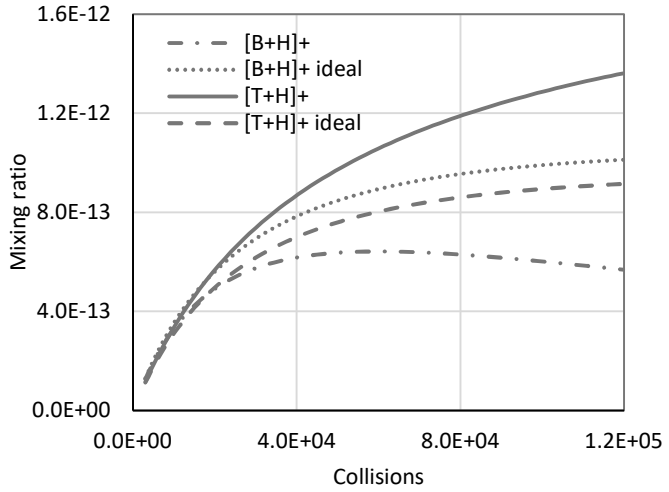

Figure 4.2: Mixing ratio in dependence of the total number of collisions; comparison of the ideal trends and the slopes simulated with transfer reaction.

By relating the difference between the slopes (of transfer reaction (26) and the ideal distribution) the deviation to the neutral distribution, and thus the extent of kinetic control can be determined. As an example, Figure 4.3 shows the relative deviation from the ideal distribution (without transfer reaction) in dependence on the number of collisions. The reference to the number of collisions gives the opportunity to eliminate the pressure dependence of the results provided no third-order reactions are part of the simulated system.

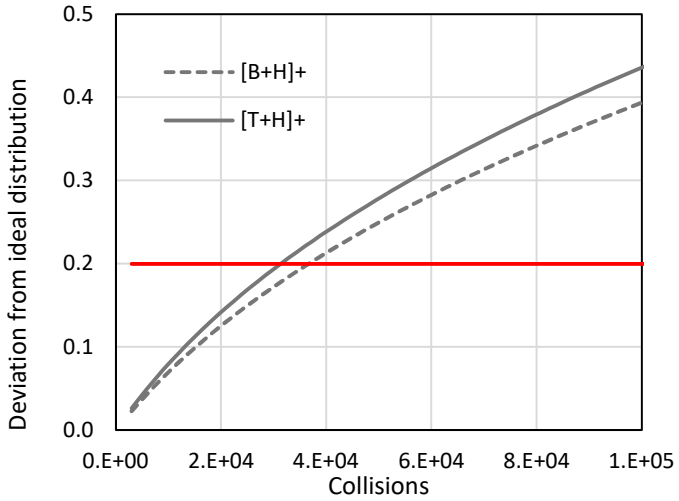

Figure 4.3: Example result of the simulations – relative deviation from the ideal distribution.

The 20% threshold is marked as reference line. For further data analysis, the total number of collisions at the 20% reference is plotted against the mixing ratios of both analytes and the mixing ratio of the reagent ions (Figure 4.4). The 20% reference is selected as the limit for high kinetic control because the precision of determined proton transfer rate constants in the literature is typically in the range of at least 20%.[33]

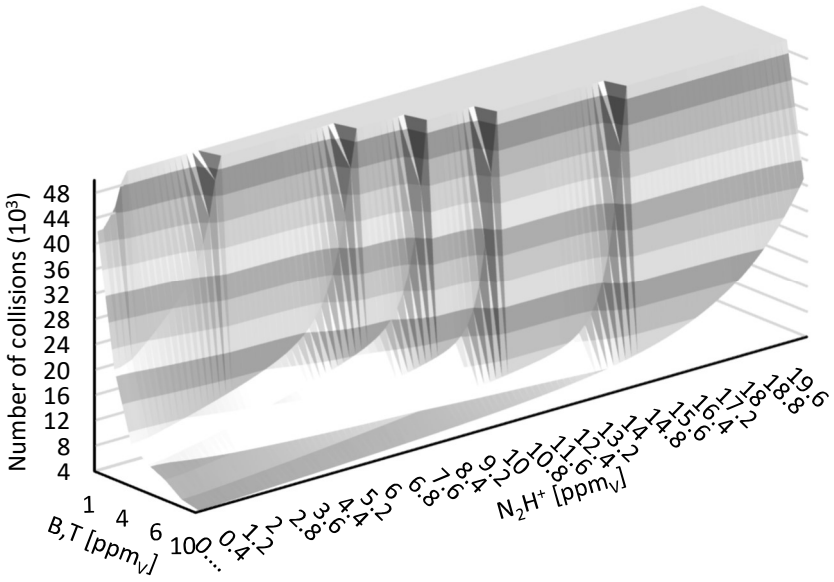

Figure 4.4: High kinetic control surface; the total number of collisions at 20% deviation in dependence of the mixing ratio of the analytes B, T and the reagent ion N_2H^+.

The resulting surface represents the threshold of high kinetic control and is defined here as the high kinetic control surface. Everything below this surface represents reaction conditions with high kinetic control. The grade of the kinetic control is a function of reagent ion mixing ratio, analyte mixing ratio and of the total number of collisions. Thus, for a specific ion source, the upper limit of analyte mixing ratios, which can be measured under high kinetic control can be determined by the number of collisions (see chapter 3.4 and following) and the amount of reagent ions present (chapter 4.2). The projection of the surface on the N_2H^+/B, T plane (Figure 4.5) shows the number of reagent ions required for ionising a specific

amount of B, T under high kinetic control. In this projection, the number of collisions is represented by different lines. In most ion sources this number is constant since their dimensions, as well as flow rates and pressures, are often fixed parameters. Thus, with a known number of collisions and a known reagent ion mixing ratio Figure 4.5 gives the maximum analyte mixing ratio measurable under kinetic control.

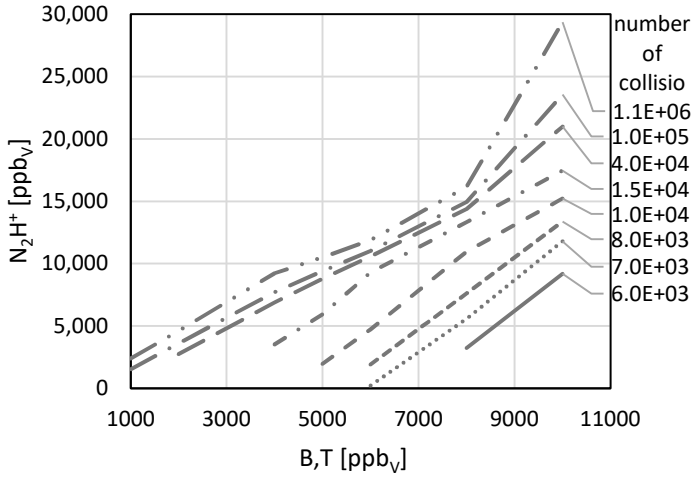

Figure 4.5: Projection of the high kinetic control surface on the N_2H^+/B, T area.

The N_2H^+ mixing ratio seems to have a linear dependence of the benzene/toluene mixing ratio. Comprehensibly, for higher analyte mixing ratios, more reagent ions are needed to maintain a high kinetic control. This dependence is a result of the 20% deviation definition. With a higher reagent ion mixing ratio, more analyte ions are produced by the reagent, lowering the deviation occurring from the analyte-analyte interactions. The dependence of the total number of collisions seems to converge to a limit. This represents a maximum amount of reagent ions needed to be able to operate high kinetic control (regarding proton transfer) under every condition (Figure 4.5). Above this limit, the required amount of reagent ions depends only on the amount of analyte present. The projection of the surface towards the collision number/N_2H^+ area also shows saturation of the dependencies (Figure 4.6). However, a high number of collisions results in more

ion transformation processes as defined in the introduction. Thus, even with a high number of reagent ions, the number of collisions has to be limited to avoid such transformation processes.

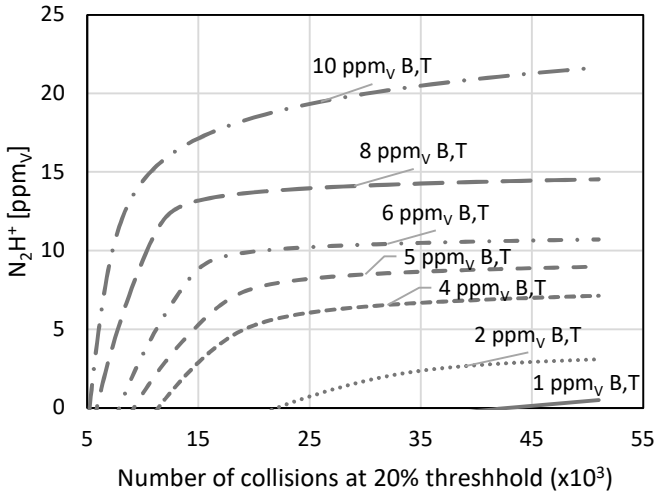

Figure 4.6: Projection on the Collision number/ N_2H^+ area.

As mentioned above, the analyte protonation must be under high kinetic control to get a signal distribution closely representing the neutral ensemble. An additional advantage of high kinetic control is that water cluster formation and post ionisation transformations of the analyte ions are reduced. The disadvantage is that using reagent ions, which can protonate the bulk gas leads to mass spectra with bulk gas ion signals being orders of magnitude larger than the analyte signals. This usually challenges the dynamic range of the analyser and detector technology used.

4.2 Reagent ion mixing ratio

For the classification of kinetic control, both, the reagent ion mixing ratio of the ion source and the number of collisions, are critical parameters (chapter 4.1). In contrast to the number of collisions, which can be easily calculated by volumes and flow rates, the reagent ion mixing ratio is often not directly measurable. To

determine the number of reagent ions inside the analyte protonation region, measurements of the protonation capacity (chapter 1.4) combined with reaction kinetics investigations are carried out. The following chapter describes the general procedures as well as the kinetics investigations. Results for the sources µ-plici 1.0 and µ-plici 2.1 are presented in chapter 4.6.2 and 4.6.5, respectively.

The protonation capacity can be expressed by two different factors. First, the total amount of reagent ions reaching the analyte protonation region ([R]) and second the ionisation efficiency (i).

$$PC\ [ppm] = [R] * i \quad (excess\ of\ analyte) \qquad \text{(eq.3)}$$

The ionisation efficiency (i) reflects the total number of analyte ions relative to the total number of neutral analyte molecules. The total amount of reagent ions depends on the amount generated by the plasma source and the loss on the passage to the analyte protonation region.

It should be noted that the protonation capacity also depends on the upper limit of detection of the MS. If the ion source produces more analyte ions as the MS can quantify, the signal will level up as well.

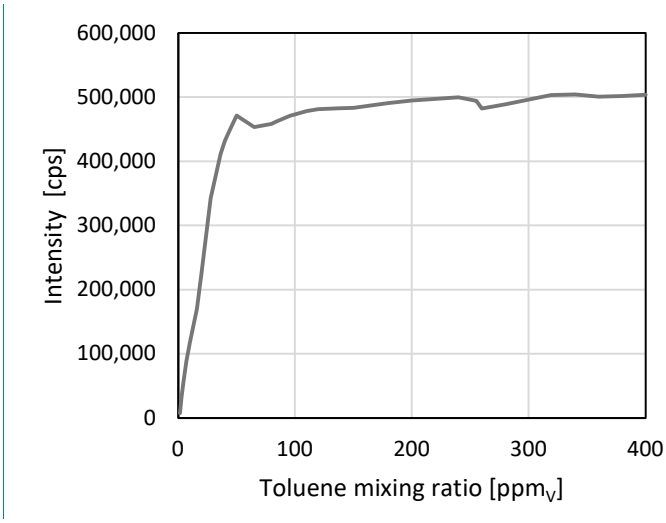

Figure 4.7: Protonation capacity of the µ-plici 2.1 setup.

Figure 4.7 shows an example scan of the linear dynamic range for toluene with the $[M+H]^+$ intensity as a function of the neutral mixing ratio. At approximately 60 ppm_V toluene, the slope levels off. Taking into account the dilution of the sampled analyte with the reagent gas, an in-source mixing ratio of approximately 30 ppm_V is reached. This represents the maximum total amount of analyte the specific source can protonate, i.e., the experimentally determined proton capacity.

By calculating the slope of the intensity/mixing ration function, the reagent ion mixing ratio inside the analyte protonation region can be determined. The ionisation efficiency, as well as the mixing ratio of reagent ions, can be determined by the second-order kinetics of a system as in equation (27).

$$[R+H]^+ + M \rightarrow [M+H]^+ + R \qquad (27)$$

The $[M+H]^+$ mixing ratio over time is then given by:

$$[M+H]^+ = [M]_0 - \frac{\left([M]_0 - \frac{[M]_0{}^2}{[R+H]_0{}^+}\right) * e^{\left([M]_0 - [R+H]_0{}^+\right)kt}}{\left(1 - \frac{[M]_0}{[R+H]_0{}^+} * e^{\left([M]_0 - [R+H]_0{}^+\right)kt}\right)} \qquad \text{(eq. 4)}$$

The calculation of the $[M+H]^+$ signal in dependence of the initial analyte mixing ratio $[M]_0$ with t = 0.5 ms , k = $1.3 \cdot 10^{-9}$ cm^3 $molec^{-1}$ s^{-1}, p = 12 mbar, and $[R+H]^+$ = 15 ppm_V qualitatively results in a function with the same slope as the experimental results (Figure 4.8 and Figure 4.7).

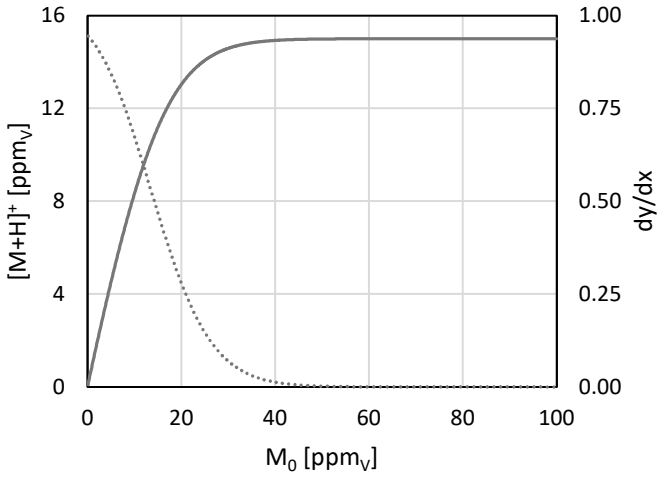

Figure 4.8: Calculation of the $[M+H]^+$ mixing ratio in dependence of the starting neutral analyte mixing ratio; the dotted line represents the first derivative.

For the slope reaching saturation ($dy/dx = 0$), the generated $[M+H]^+$ mixing ratio is equal to the starting mixing ratio of the reagent ions. Thus, for this example, the reagent ion mixing ratio is estimated to be 15 ppm_V.

A more sophisticated approach of calculating the reagent ion mixing ratio is by calculating the partial derivative with regards to $[M]_0$ of equation 4 (equation 5). Solving this derivative with $[M]_0$ equal to the value where the slope levels off (Figure 4.7) results in Figure 4.9.

$$f' = 1 - \frac{\left(1 + [M]_0 kt - 2\frac{[M]_0}{[R+H]_0^+} - \frac{[M]_0^{\,2}}{[R+H]_0^+}kt\right)e^x}{\left(1 - \frac{[M]_0}{[R+H]_0^+}e^x\right)} - \frac{\left(-\frac{1}{[R+H]_0^+} - \frac{[M]_0}{[R+H]_0^+}kt\right)\left([M]_0 - \frac{[M]_0^{\,2}}{[R+H]_0^+}\right)e^{2x}}{\left(1 - \frac{[M]_0}{[R+H]_0^+}e^x\right)^2}$$

$$with\ x = \left([M]_0 - [R+H]_0^+\right)kt \qquad \text{(eq.5)}$$

With the derivative in dependence of the reagent ion mixing ratio, the required mixing ratio of reagent ions for a saturation of the signal in dependence of the analyte mixing ratio can be computed. The resulting curves for analyte mixing ratios in the range of 10 – 90 ppm_V are shown in Figure 4.9.

Solving equation 5 with $f' = 0.01$ and a $[M]_0$ (proton capacity) of 30 ppm_V, $t = 0.5$ ms, $k = 1.3 \cdot 10^{-9}$ cm^3 $molec^{-1}$ s^{-1} and a pressure of 12 mbar results in a reagent

ion mixing ratio of $[R+H]^+ = 7\ ppm_V$. The reason for the threshold of 0.01 (indicated by the black line) instead of 0 is caused by the solver not converging in the latter case.

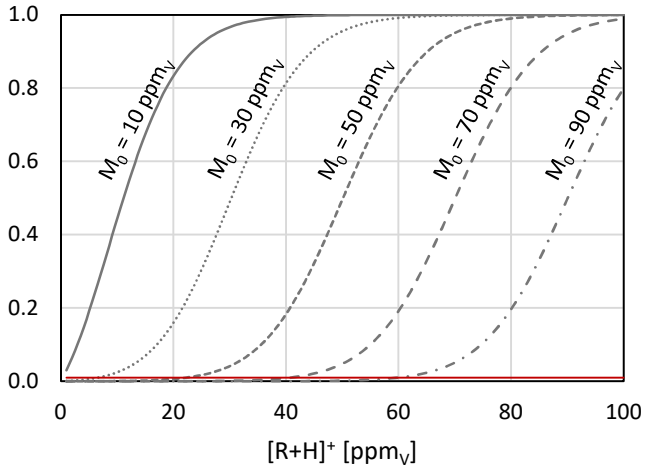

Figure 4.9: First derivative of equation 4 plotted against the $[R+H]^+$ mixing ratio; with $[M]_0$ = 10-90 ppm_V; red line indicates the 0.01 threshold used for the computing.

The difference in the two results (15 ppm_V from data fitting; 7 ppm_V computed) arises from the only qualitative comparison of the two slopes in the first approach and the determination of the correct analyte mixing ratio at the first saturated point (proton capacity).

4.3 DIA Measurements on the CTOF setup

As part of investigations regarding the first pressure reduction stage of the CTOF MS, the distribution of ion acceptance (DIA)[68] was measured with laser ionisation and toluene as analyte (Figure 3.12). DIA measurements reveal the sampling volume superposed by the neutral analyte distribution and thus reveal optimal ionisation positions.

The results indicate that the sampling efficiency is mostly shaped by fluid dynamic properties. The highest ion signals are generated in front of the skimmer and along

the skimmer to sampler axis. By manipulation of the voltage of the skimmer and the sampler, the relative maximum can be positioned near the sampler (Figure 4.10 bottom).

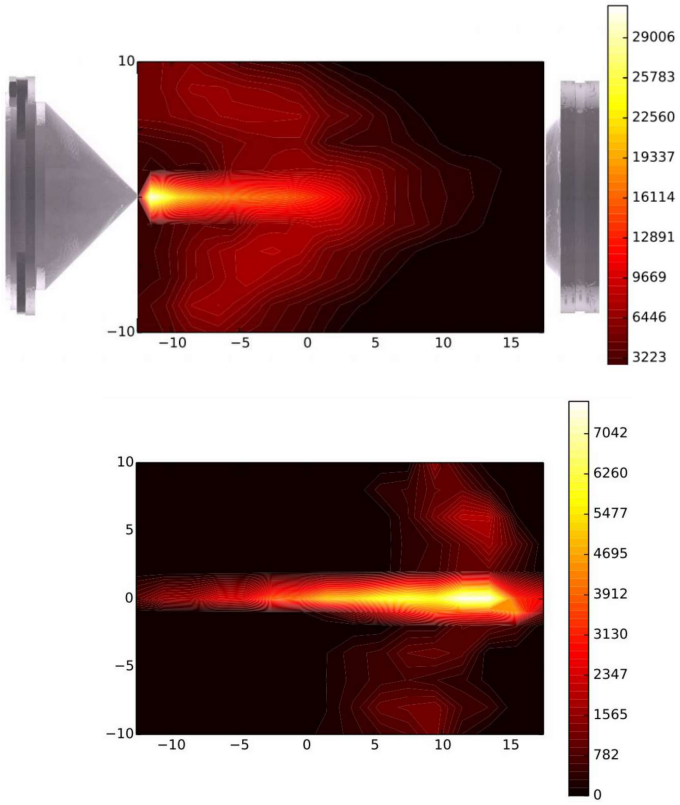

Figure 4.10: DIA measurements of the analyte ionisation chamber [65].

However, in this position, the absolute intensity is decreased. Also, the DIA measurements show that chemical transformation processes are possible in this ion source. While ionising near the skimmer and on the skimmer to sampler axis produces radical cations of toluene, ionising near the sampler results in proton-bound dimers. For measurements with the plasma source, the metastable enriched effluent must be mixed on the axis with the highest ion acceptance. The dominance of the fluid dynamic also allows the minimisation of the applied voltages with only a negligible intensity loss. When the plasma source operates, the additional helium flow will influence the fluid dynamic of the source further. Thus, DIA measurements were carried out with the plasma source mounted 15 mm above the skimmer to sampler axis, and a typical helium flow of 100 sccm through the source

was maintained. However, the results show no significant change in shape or intensity compared to the DIA measurements shown in Figure 4.10.

4.4 Reaction time determination on CTOF setup

For determination of the available reaction time inside the ion source, ion transfer measurements were carried out. To calculate the transfer time from sampler to the centre of the chamber and further to the skimmer, the times ions need from of these three positions to a mesh electrode were measured (cf. Figure 3.12).

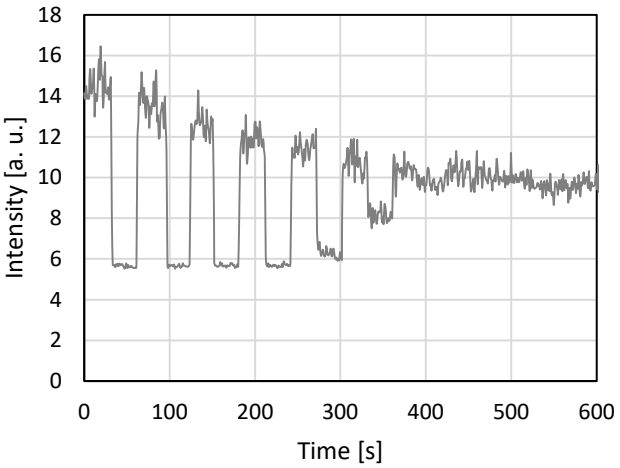

Figure 4.11: Raw ion signal for the reaction time measurement.

By scanning the delay between the laser pulse and ion gate opening time, the resulting ion signal is related to the amount of the ion pulse passing the gate. Each signal is normalised to the full signal measured 30 seconds before and after, to eliminate long-term signal variations caused by analyte mixing ratio variation, laser performance variations or changes in the UV transmission of the window material (Figure 4.11). By fitting this signal and calculating the first derivative of the resulting function, the transient ion signal is obtained (Figure 4.12, dashed line).

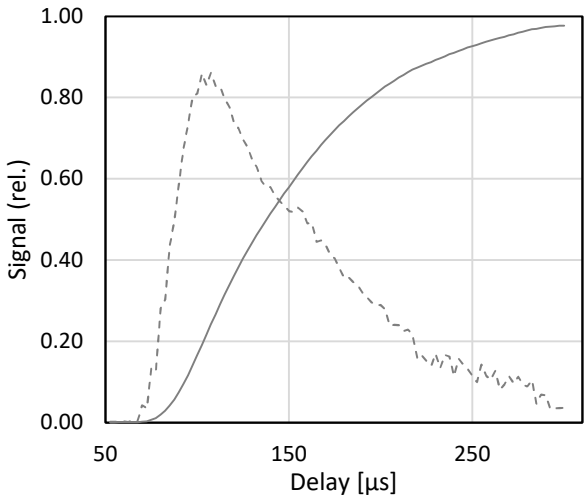

Figure 4.12: Calculated ion pulse (dotted) based on the measured signals (solid) for a scan of delay times.

For the calculation of the transfer time and thus the assumed reaction time, the maximum of this signal is compared to the signals measured at the other positions. It becomes readily apparent that the transfer time is independent of the voltages in the range which are typically applied. With higher pressure, the transfer time increases slightly. From these results, it can be assumed, that the reaction time (transfer time from the centre of the source to the skimmer) is about 100 – 150 µs and is only dependent on the fluid dynamic properties.

4.5 Influence of plasma parameters

On the free arrangement setup (chapter 3.3.1) as well as on the cage setup (chapter 3.3.2), the plasma parameters are varied, and the direct impact on the ion signal is recorded. While varying the helium flow through the plasma source will change the fluid dynamics in the ionisation region, electrical parameters should have no significant influence on the area outside of the plasma source. In the µ-plici setups, the plasma parameters have a more significant influence on the reaction cascade because changes in the flow characteristic of the plasma source will also change the pressure inside the reagent chamber. With parameters in which the plasma afterglow enters this chamber, changing polarisation of the plasma discharge changes the reaction ion generation as well.

In the setups with the plasma source effluent penetrating the first pressure reduced stage of the CTOF, the ion signals are most intense when the plasma source is operated between 400 mbar and 600 mbar which refers to a helium flow of 50 – 70 sccm. For higher volume flows of helium, the signal intensity decreases. It is assumed that the higher flow changes the fluid-dynamic conditions inside the ion source significantly. The impact can be imagined from the DIA measurements, where a higher helium crossflow can deflect the analyte flow on the skimmer/sampler axis (chapter 4.3). The MS collects only ions on the skimmer to sampler axis efficiently. For increasing the plasma source gas flow, the analyte flow direction (from sampler to skimmer) can be redirected, which will lower the ions present in the solid angle of acceptance of the MS. A second optimum of the plasma pressure was found at 100 mbar where the conditions can ignite a secondary plasma between skimmer and sampler. The secondary plasma fills the space between skimmer and sampler so that the ionisation takes place in a much larger volume, which increases the ion signal significantly. The µ-plici setups show most abundant ion signals at plasma pressures of about 1000 mbar to 1700 mbar. The optimum helium flow depends on the used orifice.

The electrical parameters need to change for the positive or negative driven plasma source. A range of 5 mA to 10 mA plasma current needs to be established. All µ-plici setups exhibit a correlation between the plasma current and the achieved ion signal. For higher plasma currents, corresponding higher signals are observed. The change between a negative and positive voltage at the inner electrode of the plasma source shows a clear preference of the negative voltages. Nevertheless, the free arrangement setup can be operated with positive and negative voltages with comparable performance. However, with positive voltages, the plasma source cannot be operated under constant performance for a long time, and additional signals at $^{m}/_{z}$: 191 to 198 appear in the mass spectrum (Figure 4.13). These ions show the typical isotopic pattern of platinum, which is the material used for the aperture.

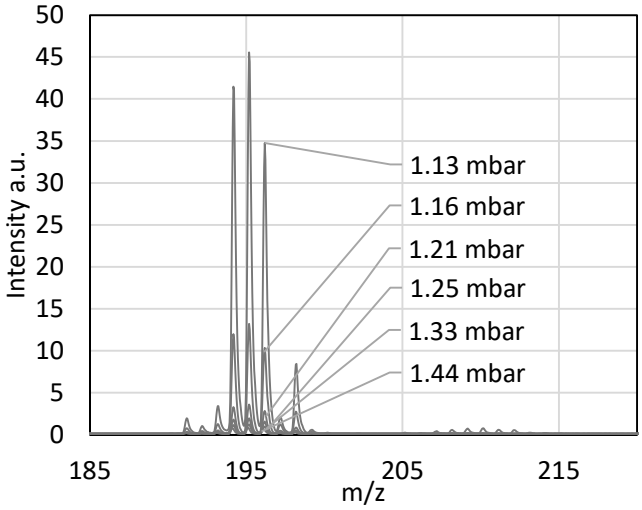

Figure 4.13: Platinum signals at different source pressures in the range 1.13 mbar to 1.44 mbar.

Thus, this mode of operation leads to significant degradation of the aperture, i.e., the orifice diameter widens, which changes the pressure inside the plasma source, the outflow characteristics, and the dimension of the plasma outside of the plasma source. To avoid this, tantalum was tested as material for the orifice, and a long-time measurement over 170 h continuous operation showed no significant change in the plasma source pressure and the MS performance. Additionally, no tantalum ions are observed in the mass spectra. Decreasing the electrical current leads typically to a decreasing signal. However, if the plasma is significantly present inside the ionisation region and ignites a secondary plasma, the performance depends much more on the currents of the electrodes in the ionisation chamber, rather than on the plasma source current itself. Thus, changing the electrical current of the plasma source has almost no impact on the ion signal intensity.

4.6 Ion source development

The main objective of this work is the development of the ion sources listed in the experimental section. in the following, the experimental results obtained with each ion source, as well as the conclusions for the successor designs are presented. The ion sources are presented chronologically giving a better overview of the evolving designs.

4.6.1 Initial version - free arrangement setup

As this setup (cf. Figure 3.4) was intended to validate the FT-QIT measurements, first investigations were to modify the MS for operation with hydrogen bulk gas. After modification of the sampler, sample pressure and the pumping performance, the system was used for validation of the QIT. In addition to the performance comparison with regard to the detection limit and linear dynamic range, the CI was used for validating the quality of the analyte mixtures to identify possible impurities. The initial measurements with the plasma source indicated a signal increase of about 1 order of magnitude when changing the aperture orifice diameter of the plasma source from 10 µm to 100 µm. First organic analytes investigated were a mixture of volatile organic compounds (VOC) as depicted in Figure 4.14. The different compounds are present in the 20 - 70 ppb_V mixing ratio range.

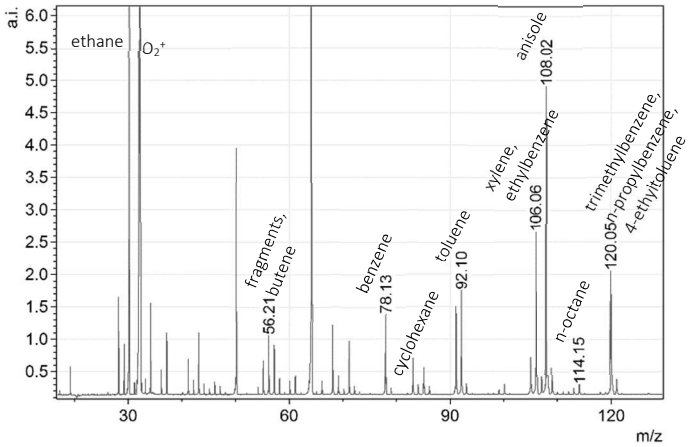

Figure 4.14: First measurements with the plasma source; VOC mixture in synthetic air; 10 µm aperture.

The initial position of the plasma source is 15 mm above the axis between the sampler and skimmer. Simulations carried out by PAC suggested that the metastable helium density decreases over 15 mm to nearly background level. Consequently, the analyte ion production should be increased by decreasing the distance between the plasma source and the analyte-containing gas flow. Nevertheless, arranging the plasma source exit 5 mm above the axis between sampler and skimmer, the preferred position according to the simulations, leads to lower signals.

This can be explained by the impact of the helium expansion on the fluid dynamic properties of the first pressure reduction stage. By decreasing the distance between plasma source exit and analyte gas flow, the latter is deflected further down. The DIA measurements (Figure 4.10) indicate that ions further away from the centre axis are not sampled efficiently. This is not reflected in the simulations because both gas flows were simulated separately, and thus, a deflection could not be considered.

Nature of analyte ions

Depending on the plasma parameters, the plasma afterglow is more or less present in the ion source. According to the findings above, the ion signals are increased by the use of a wider aperture, which leads to deeper penetration of the plasma afterglow into the ion source. As a result and taking into consideration the distance between the plasma and the analyte gas flow, the nature of generated analyte ions is highly dependent on the plasma parameter and the bulk gas. In a nitrogen atmosphere, the generated analyte ions are most likely a result of charge transfer with N_2^+ and N_4^+. When hydrogen is present in the bulk gas, the analyte ions will most likely be protonated by N_2H^+ and H_3^+, depending on the mixing ratio, as dictated by the reaction cascade (cf. Table 3).

Kinetic control

As mentioned in chapter 4.3, the reaction time, which corresponds to the transfer time required to reach the skimmer from the centre of the ion source is 100 – 150 µs. At a pressure of 1 – 3 mbar this results in a total number of collisions of 100-450. According to the high kinetic control surface (Figure 4.4), this low collision number suggests a high kinetic control even for analyte mixing ratios exceeding 10 ppm_V and low reagent ion mixing ratios. Concomitantly, the performance of this source type suggests a higher number of primary reagent ions to be present. This assumption is also supported by the measurements made with the µ-plici 1.0 setup. With respect to the signal intensities, the free arrangement setup performance is better than the µ-plici 1.0. Additionally, with the µ-plici 1.0 no

upper limit of detection for toluene was detected (Figure 4.19). Measurements for the limit of detection reveal a signal to noise of 25 for a 180 ppt_V toluene signal. It should be noted that the pressure in the reaction region is presumably higher because it is positioned in the expansion of the analyte flow. Nevertheless, the source operates under high kinetic control even if a pressure of 10 mbar is assumed in the expansion.

The high kinetic control mode is favoured for the analyte ionisation. Unfortunately, in this setup, the reagent ion formation (from the bulk gas) is in the same location, thus, also under kinetic control. This leads to low conversion of helium metastables into reagent ions, for example, H_3^+ when operated in hydrogen. This low conversion could be a reason for the low protonation ratios.

Seeded vs non-seeded

Depending on the source parameters, a secondary plasma can be ignited outside the plasma source. This plasma is classified as a seeded plasma. A seeded plasma is stabilised by the support of a primary plasma. Thus, if the primary plasma is terminated with all gas flows held constant, the secondary plasma is extinguishing as well. The same holds true when the voltages applied to the ion source are decreased while the primary plasma is maintained. The secondary seeded plasma occupies an extended volume inside the ion source leading to a higher ion current of up to 400 nA and thus higher ion signals. The ion current is measured on the mesh electrode inside the ion transfer shown in Figure 3.12.

While the seeded mode delivers higher ion signals, a sustained operation is critical, and the stability over a long time is low (see also chapter 4.5). The conditions inside the ion source are expected to be more energetic compared to the effusion mode since the analyte is in direct contact with the plasma.

Conclusion

The free arrangement setup shows a good overall performance with respect to limit of detection, linear range, total ion current and kinetic control but lacks the

ability of pure molecular ion production. The reaction cascade is not divided into different areas, which leads to "one-pot" reaction properties. Thus the efficiency of the transformation of helium metastables is directly coupled with the properties of the analyte ionisation. At high kinetic control, the analyte signal distribution is closely resembling the neutral ensemble, but the efficiency of generating only protonated species is not high since the reagent ion production itself is under high kinetic control as well. This leads to more complex mass spectra because several different ion signals belong to one analyte. Thus, for the simultaneous measurement of several analytes, the identification can become challenging. The seeded mode produces higher ion signals, which leads to lower detection limits and is thus a promising operating mode but only when it can be better controlled and stabilised.

4.6.2 µ-plici 1.0

Initially designed as a coupling module and analyte inlet stage of the plasma source for hyphenation with the FT-QIT, µ-plici 1.0 (Figure 3.6) was used to investigate utilizing H_3^+ ions as protonation reagent in nitrogen bulk gas. Thus, all measurements are carried out in a nitrogen atmosphere. By adding the reagent gas directly downstream of the plasma source aperture, the formation of reagent ions takes place prior to the analyte ionisation. Thus, using hydrogen to create H_3^+ ions results in protonation of the analytes. The GC-capillary further separates reagent ion formation and analyte ionisation regions. In contrast to the free arrangement setup, this benefits the protonation ratio.

Charge transfer vs proton transfer

The separation of the reagent ion production and the analyte ionisation region allows using different reagent gases resulting in different ionisation pathways as observed in the free arrangement setup(chapter 4.6.1). While nitrogen produces mainly charge transfer (CT) species, hydrogen results in analyte ions generated via proton transfer (PT). Thus, adding helium into the reagent tube leads to charge transfer species as the nitrogen bulk gas produces N_2^+ and N_4^+. Adding hydrogen

leads to H_3^+ reagent ion production and thus to protonation of the analyte molecules.

The differences are depicted in Figure 4.15, where toluene (1 ppb_V) is sampled from 600 mbar, which is equal to a 70 sccm flow into the ion source. The plasma source is operated with 70 sccm helium, and 250 V. Sampler and skimmer are held at 5 V and 3 V respectively. As reagent gas, 70 sccm helium or a mixture of 750 ppm_V hydrogen in helium is used.

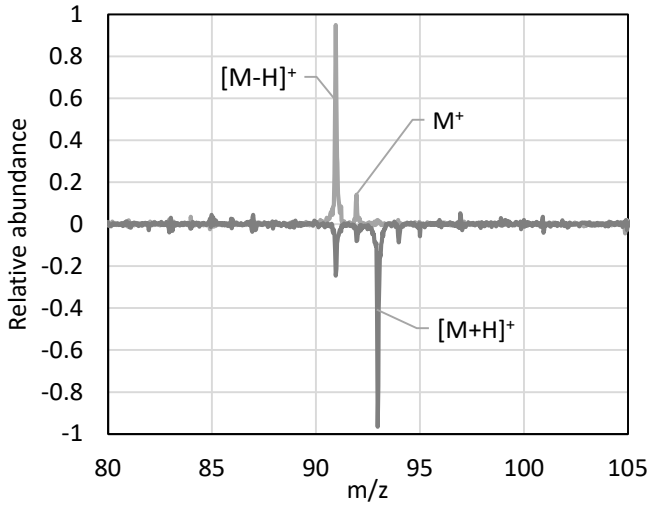

Figure 4.15: Toluene (1 ppb_V) mass spectra (1 sec average) depending on the reagent gas (CT) helium (positive), (PT) 750 ppm hydrogen in helium (negative), the negative values for the PT mode are chosen for comparison purposes.

The more energetic conditions in the charge transfer mode result in the fragmentation of the toluene yielding $[M\text{-}H]^+$ (m/z 91) as main analyte ion species, while the M^+ signal has an abundance of about 15 %. With a 750 ppm_V hydrogen mixture in helium present, the dominant analyte ion is $[M+H]^+$ (m/z 93). The M^+ signal has an abundance of about 10 %, and the $[M\text{-}H]^+$ ion can still be observed with approximately 25 % abundance.

Proton transfer optimisation

By adding hydrogen to the helium reagent flow, protonation of the analyte in a nitrogen atmosphere was investigated. Increasing mixing ratios of hydrogen lead to a significant change of the mass signals of $^{m}/_{z}$ 91 (fragment, mostly from CT) and $^{m}/_{z}$ 93 ($[M+H]^+$) of toluene. Thus, the protonation of analytes diluted in nitrogen can be achieved by adding hydrogen into the plasma effluent, producing H_3^+ as reagent ions as is depicted in Figure 4.15.

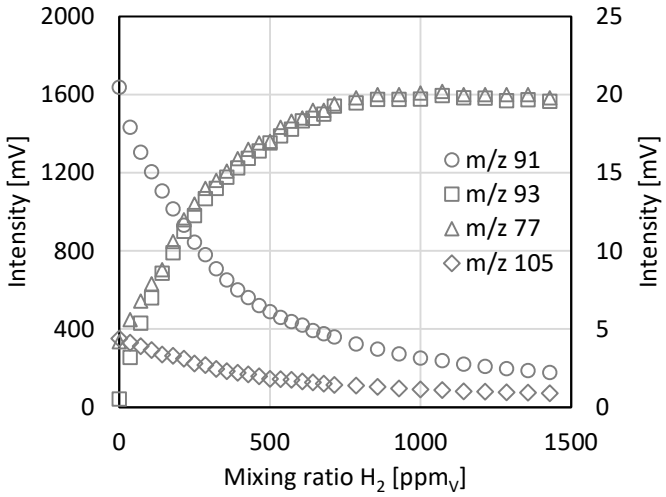

Figure 4.16: Determination of the optimal working point; the slope of different toluene signals in dependence of the H_2 mixing ration; $^{m}/_{z}$ 77 and $^{m}/_{z}$ 105 are plotted on the secondary intensity axis.

Figure 4.16 depicts the hydrogen mixing ratio variation in the reagent gas flow. Besides the change form $^{m}/_{z}$ 91 to $^{m}/_{z}$ 93, which is also seen in Figure 4.15, $^{m}/_{z}$ 105 and $^{m}/_{z}$ 77 show similar behaviour, respectively. The appearance of these two mass signals can be described with the reactions (28,29). [70, 71]

$$C_6H_5CH_2^+ (91) + \text{c-}C_6H_5CH_3 \rightarrow C_8H_9^+ (105) + C_6H_6 \quad (28)$$

$$H_3^+ + \text{c-}C_6H_5CH_3 \rightarrow C_6H_5^+ (77) + H_2 + CH_4 \quad (29)$$

With increasing hydrogen mixing ratio, the $^{m}/_{z}$ 105 signal decreases because the precursor ion $C_6H_5CH_2^+$ ($^{m}/_{z}$ 91) is a product of the charge transfer with N_2^+ reagent ions. The optimal working point for most of the experiments carried out with the

µ-plici 1.0 setup is about 750 ppm_V hydrogen mixing ratio. At this point, the $[M+H]^+$ signal of toluene reaches a maximum. The charge transfer products m/z 91 and m/z 77 are still observed, but increasing the hydrogen mixing ratio further leads to an overall intensity loss. Additionally, it must be noted that the m/z 91 fragment can occur out of strongly exothermic proton transfer as well. Consequently, m/z 91 and m/z 77 can be observed under pure proton transfer conditions. The signal loss at higher hydrogen mixing ratios is considered to be a result of backflow of hydrogen into the plasma source. This changes the composition of the plasma gas and results in worse plasma performance.

Proton affinity

In proton transfer mode, the proton affinities of all substances present dictate the possibility of protonation and the excess energy remaining in the molecules. With a proton affinity of 422.3 kJ/mol hydrogen as reagent gas is capable of protonating nearly all other molecules except helium, neon, fluorine, argon, and oxygen (see also Table 1). Thus, even inert gases such as xenon or krypton can be protonated under these conditions.

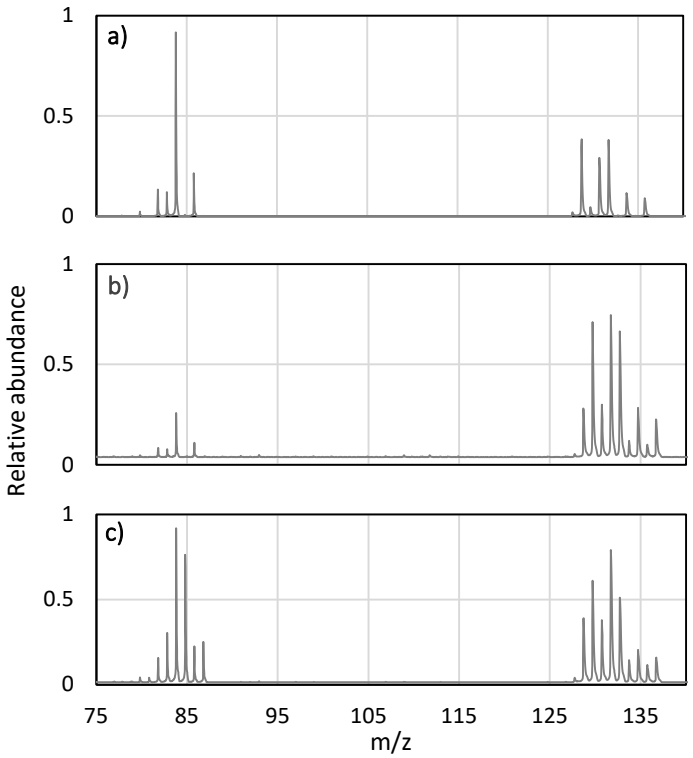

Figure 4.17: Isotopic pattern of xenon and krypton under charge transfer (a), proton transfer mode in nitrogen (b) and in helium (c) as bulk gas.

For the protonation of rare gases, a mixture of krypton and xenon in nitrogen, 10 ppm_V each, is used. This analyte is sampled from 600 mbar resulting in 70 sccm flow. The plasma parameters are 70 sccm helium, 250 V plasma voltage, and 70 sccm reagent gas. In charge transfer mode (Figure 4.17, a) the isotopic patterns of the M^+ of krypton, as well as xenon, are observed. Switching into proton transfer mode by adding 750 ppm_V hydrogen in helium as reagent gas, the isotopic pattern of krypton remains identical, whereas the pattern of xenon gets complex (Figure 4.17, b). Using a mixture of krypton and xenon in helium (10 ppm_V) leads to the complex isotopic pattern for both atoms (Figure 4.17, c).

An explanation for this observation is the incomplete protonation. The M^+ and the $[M+H]^+$ species are observed simultaneously. In nitrogen as bulk gas xenon is protonated partly, whereas krypton is detected as M^+ only. In helium, both atoms appear as $[M+H]^+$ ions and M^+, which leads to an overlay of the isotopic patterns of both ionic species. Nitrogen with a proton affinity of 493.8 kJ/mol is located

between krypton and xenon (see also Table 1). Thus, protonated krypton is capable of transferring the proton to nitrogen but not onto helium. With helium as bulk gas, H_3^+ protonates both krypton and xenon directly but protonated krypton can only transfer the proton to xenon. Due to the low number of collisions, the probability of the latter is low, and thus, krypton is observed as $[M+H]^+$ as well. With nitrogen as bulk gas, predominantly N_2H^+ is formed as reagent ion, preventing the formation of significant amounts of protonated krypton.

Protonation ratio

By adding the T-piece arrangement, µ-plici 1.0 provides a means of adding hydrogen while measuring analytes diluted in nitrogen. By adding 70 sccm of a mixture of hydrogen in helium into the T-piece and varying the hydrogen mixing ratio, the overall performance and the protonation ratio (PR) can be determined in dependence of the H_2 mixing ratio (Figure 4.16). Determining the PR over this hydrogen variation results in the graphs shown in Figure 4.18. As expected, the PR increases with increasing hydrogen mixing ratio and reaches a ratio of near one. Compared to Figure 4.16, the PR rises much faster than the $[M+H]^+$ signal, which is because the M^+ signal is low in intensity and decreases swiftly.

The fragments are not only a result of still existing charge transfer pathways but can also occur due to energetic proton transfer, as mentioned above. Since most of the m/z 91 fragment is expected to be of the charge transfer pathway, the overall protonation ratio, which considers the fragments can be calculated (Figure 4.18, black). Here, m/z 93 and the fragment m/z 77 are defined as proton transfer species, and m/z 92 and the fragments m/z 91 and m/z 105 are regarded as charge transfer species. The curvature of the latter is less pronounced because the M^+ signal is no longer determining, and the PR no longer reaches values near one. At the optimal working point, the PR is at 80%.

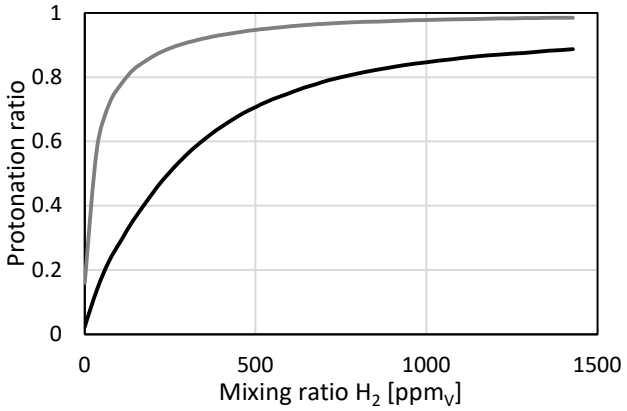

Figure 4.18: Protonation ratios µ-plici 1.0; grey: PR calculated with equation 2; black: PR calculated with $^{m}/_{z}$ 91 considered as CT species, including fragments $^{m}/_{z}$ 77 (PT) and $^{m}/_{z}$ 105 (CT).

Proton capacity

With the µ-plici 1.0 setup, the proton capacity (PC) is determined by sampling toluene diluted in nitrogen from 600 mbar. The toluene mixing ratio is varied between 10 ppb_V and 400 ppm_V. Simultaneously, 600 ppb_V of a mixture of xenon and krypton diluted in nitrogen is added. While krypton cannot be protonated by N_2H^+ reagent ions, protonated xenon ions are observed, and the signal remains constant over the full mixing ratio range of toluene added. For this experiment, the helium flow inside the plasma source, the hydrogen in helium mixture (750 ppm_V), as well as the analyte flow is set to 70 sccm each.

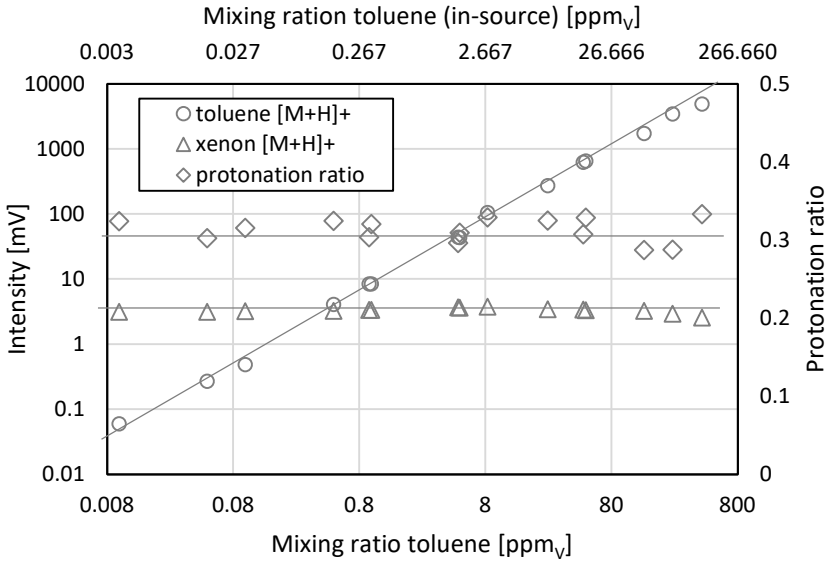

Figure 4.19: Measurement of the protonation capacity with the µ-plici 1.0 setup.

When reaching the PC in an experiment with high reaction times, it is expected that the toluene signals saturate. Additionally, the xenon signals are expected to disappear due to the lower proton affinity. As demonstrated in Figure 4.19, the ion signal of protonated toluene is linearly responding to the toluene mixing ratio over the entire covered range, while the signal corresponding to protonated xenon shows a constant level. Exceeding a toluene mixing ratio of 100 ppm_V, the trend of the xenon signal shows a slight decrease. Additionally, a slight curvature in the toluene signal is visible. This could be a hint that the PC is nearly reached. However, no saturation is observed. Thus, the PC could not be determined with these measurements and is expected to exceed 100 ppm_V in-source.

In charge transfer mode, where only helium is added through the T-piece, the maximum quantifiable analyte mixing ratio could not be reached. Additionally, adding hydrogen led to a decrease in the total ion count. It is therefore assumed that the charge transfer mode has an even higher quantifiable amount of analyte ions.

Conclusion

The µ-plici 1.0 ion source provides the opportunity to protonate analytes diluted in nitrogen. The ion source can be operated in charge transfer mode by using pure helium as reagent gas or in proton transfer mode by adding hydrogen. Adding the reagent gas in close proximity to the plasma source aperture enables the sequencing of the "one-pot" chemistry driven in the free arrangement setup. Thus, reagent ions are formed physically separated from the analyte ionisation region. H_3^+ as reagent ion can protonate a broad analyte spectrum including rare gases as krypton and xenon. In both, charge transfer and proton transfer mode, toluene exhibits fragmentation. The electric field gradients present in the ion source and the primary ion transfer are chosen to be low to minimise CID processes. Thus, it is reasonable to assume that this fragmentation is caused by the exergonicity of the ionisation process, i.e., the proton transfer step.

The µ-plici 1.0 arrangement can be modified by plugging a GC-column onto it. This yields a higher protonation ratio but leads to a significant reduction of the

total ion count (TIC). The decreasing of the TIC has at least two causes. On the first hand, the capillary increases the loss of reagent ions. On the other hand, the capillary produces a directed gas flow closer to the skimmer sampler axis and thus, to changes in the fluid dynamics, as discussed in chapter 4.5.

The kinetic control of the analyte ionisation cascade is assumed to be comparable to the free arrangement setup because the changes made by adding the additional reagent gas are considered negligible. Also, the separation of reagent ion production and analyte ionisation allows of a cleaner formation of reagent ions, and the plasma is not present inside the ion source itself.

The ion signals in proton transfer mode are lower as in charge transfer mode and higher hydrogen mixing ratios lead to a further reduction. It is assumed that this is caused by a hydrogen backflowing, changing the conditions inside the plasma source.

4.6.3 Cage arrangement

The cage arrangement setup (Figure 3.5) was constructed by PAC as an improved version of the free arrangement setup. The goal of this version is the stabilisation and control of the seeded plasma leading to lower detection limits. Also, the cage arrangement setup is a prototype of an external ionisation method for the FT-QIT. For this purpose, the ion current has to be as high as possible, allowing to build an ion transfer into the QIT with a reduced transmission efficiency, i.e., the capillary type design[2]. The analyte inlet is constructed coaxially to stabilise the seeded plasma. Through the outer tube, a constant gas flow is supplied while the analyte

[2] Note added in proof. Ion loss in narrow capillaries is considerable, however, this approach represents *the only feasible route* for transporting ions *through* an alternating RF field with amplitudes in the several hundred volt peak to peak range. This scenario is specific for the Zeiss FT-QIT. Due to the necessity of embedding the ion image current detection electrodes into the QIT cap electrodes, these need to be held at ground – the QIT ring electrode is then driven with the required trapping RF. As a consequence, the analyte feed needs to penetrate through the QIT ring electrode. Neutrals are unaffected by such fields; however ion transport into the trap was proven in subsequent research to be impossible without embedding them into a gas flow acceptable to the vacuum system and operational mode of the FT-QIT.

is pulsed through the inner tube. Also, hydrogen can be added, with the bulk gas, to implement the protonation under a nitrogen atmosphere as is demonstrated with the μ-plici 1.0 setup.

Seeded plasma

The focus of this ion source iteration is the seeded plasma mode. In the free arrangement setup, a seeded plasma mode was attained, and it showed promising results, although the stability was not satisfactory. Using the next generation of plasma sources constructed by PAC provides an additional electrode, the cap of the plasma source. Thus, different reference voltages can be applied, in contrast to the fixed ground potential present in the free arrangement setup. In addition, a cage electrode is implemented, shielding the volume in which the secondary plasma operates. The reasoning behind the variable reference voltage of the cap is the optimisation of the seeded plasma independent of the voltages needed for the primary ion transfer.

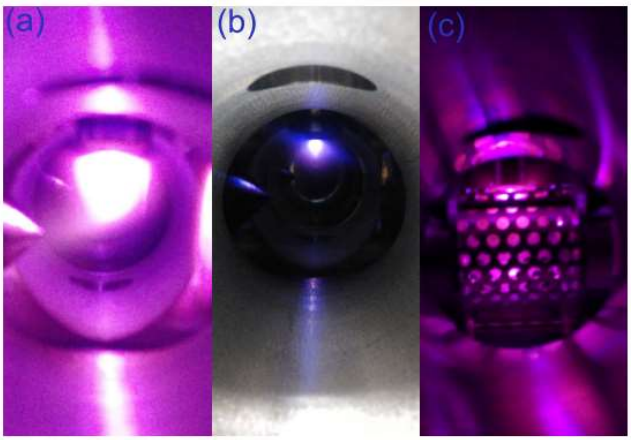

Figure 4.20: Seeded vs expansion mode; (a) seeded mode in the free arrangement, (b): expansion mode in free arrangement setup, (c) expansion mode with the cage arrangement setup.

In Figure 4.20, the seeded plasma mode (a) is compared with the normal expansion mode, both in the free arrangement setup, and the cage arrangement setup(c). Although the cage electrode, in combination with the new plasma source cap and

the new analyte inlet, allows for more variability, the seeded mode could not be stabilised with reference to analytically exploitable conditions. However, the expansion mode in this new setup showed improved performance compared to both modes in the free arrangement setup. Thus, optimisations and analytical performance tests for this mode are carried out.

The new inlet is movable using a compression connection; the skimmer to sampler/inlet distance is adjustable by moving the whole inlet in or out. As the distance increases, the ion signal increases (Figure 4.21). This increase is more pronounced between 10 mm and 12 mm skimmer and inlet distance. After this initial increase, the slope decreases and the ion signal increases up to the maximum distance of 22 mm. It is assumed that the initial increase is induced by manipulation of the expanded plasma. The position at 10 mm is directly below the plasma source exit. Thus, the inlet electrode is very close to the expanded plasma and may influence it.

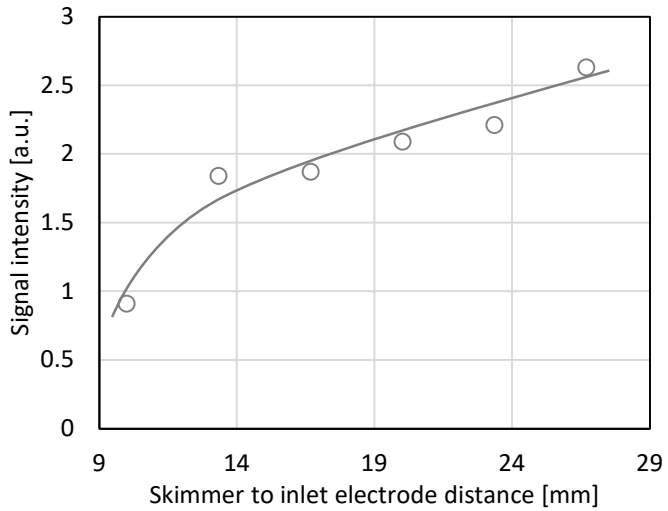

Figure 4.21: Inlet position variation. The signal intensity observed with 208 ppt$_V$ toluene present is plotted in dependence of the inlet position. The plasma source position is at 10 mm.

The increased analyte signal at larger distances between skimmer and inlet is assumed to be caused by increased mixing of the analyte gas stream, sheath gas, and plasma source effluent. Consequently, a higher ionisation efficiency is

reached. It should be noted that an increasing distance and thus mixing will also increase the reaction time since the gas velocity along the skimmer/inlet axis drops. This leads to a lowered kinetic control for this ion source.

Another critical parameter for the seeded plasma is the pressure inside the ion source. Thus, the pressure influence is investigated in the range between 1 and 10 mbar (Figure 4.22). The TriScroll pump for the ion source is equipped with a butterfly valve to accomplish this experiment. As analyte 208 ppt_V of toluene diluted in nitrogen is used, and the measurements are repeated with different helium flows through the plasma source, which results in different plasma source pressures.

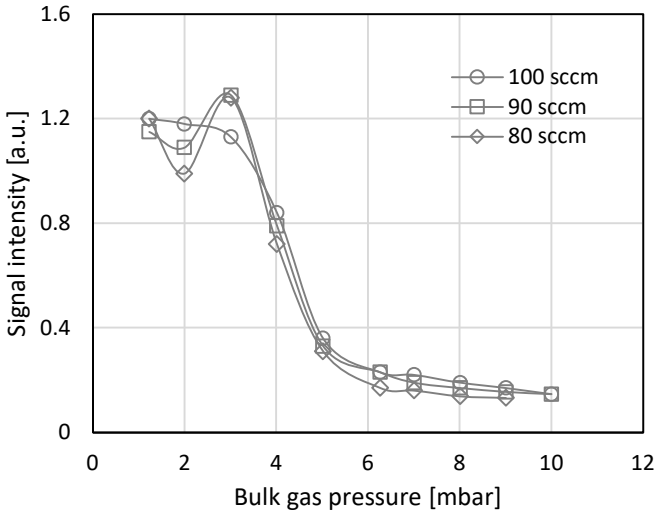

Figure 4.22: Pressure variation (1-10 mbar) inside of the ion source at different plasma pressures; 208 ppt_V toluene as analyte; shown ion signals are the sum of m/z 91 and m/z 92; measured in charge transfer mode.

In the covered range, a variation in plasma source pressure (due to different helium flows in Figure 4.22) does not change the ion signal, and consequently, the trends are similar (Figure 4.22). In the Range from 1 mbar to 3 mbar the ion signals vary only slightly. From 3 mbar to 6 mbar the signals decreases significantly and tails out up to 10 mbar with a signal intensity of ~10%. The ion source operates favourably up to 3 mbar source pressure, which is also the range in which the kinetic control is highest. The exact reason for the decreasing signal above 3 mbar

is not investigated, but a change of the fluid dynamic conditions, including the plasma volume and the DIA of the MS, is conceivable.

Protonation with hydrogen present in the sheath gas

The coaxial analyte inlet allows the addition of hydrogen via the outer gas inlet. As it is the case in the µ-plici 1.0 version, the mixing ratio of hydrogen can be varied, and thus the protonation ratio can be determined in dependence of the H_2 mixing ratio. However, the reaction cascade is not spatially separated, in contrast to the µ-plici 1.0 setup. Nevertheless, through the coaxial arrangement, the reagent gas added through the outer gas inlet can be assumed to surround the analyte flow and thus is in closer vicinity to the plasma afterglow. Consequently, a partial spatial separation of the reaction cascade can be reached, which makes a higher protonation ratio possible.

The outer gas inlet is fitted with two mass flow controllers; one delivers 70 sccm of helium and the other 10 sccm of hydrogen. For these experiments, a mixture of 1% hydrogen in helium is used instead of pure hydrogen to reach lower mixing ratios. hydrogen is varied in the range of 300 ppm_V up to 2800 ppm_V.

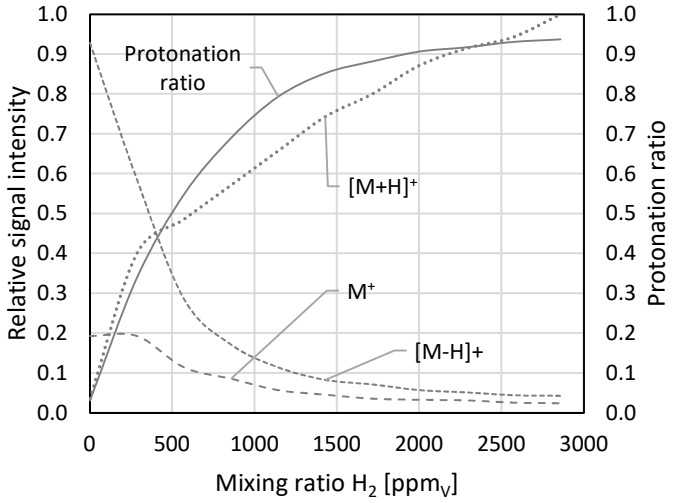

Figure 4.23: Variation of the hydrogen mixing ratio (300-2800 ppm_V) in the cage arrangement setup; relative intensities of different ionic toluene species in dependence of the hydrogen mixing ratio; secondary axis: protonation ratio.

The resulting ion signals recorded with an 83 ppt_V mixture of toluene diluted in nitrogen are shown in Figure 4.23. As expected, the signals for the M^+ as well as $[M-H]^+$, both products of charge transfer from nitrogen reagent ions, decrease with increasing hydrogen mixing ratio. The signal of the single protonation product ($[M+H]^+$) increases over the entire range studied.

The protonation ratio increases to a maximum value of 0.93. It should be noted that for this calculation, the m/z 91 fragment is accounted for as a charge transfer product. As already mentioned above, this is not necessarily entirely the case, and it could also occur out of exothermic proton transfer. Considering the latter, the protonation ratio becomes even higher.

Continuous analyte sampling

The ion source is designed for pulsed analyte sampling. However, for comparison purposes to the free arrangement setup, the source is operated in continuous mode as well. It is concluded that with similar using mixing ratios, the limit of detection is much lower as compared to the free arrangement setup.

For this setup, ion currents are measured in charge transfer as well as proton transfer mode. The ion current is measured on a mesh mounted behind the tube lens in the ion transfer stage, as described in chapter 3.7. For these measurements, the source is operated at 560 mbar plasma source pressure (100 sccm helium) and 70 sccm sheath gas flow. In charge transfer mode with 208 ppt_V toluene present in nitrogen sampled from 600 mbar (70 sccm) and helium as sheath gas on, the ion current is measured to be in the range of 5 - 5.5 nA. In proton transfer mode with 3‰ hydrogen in helium as sheath gas, the ion current is measured to be 4 nA.

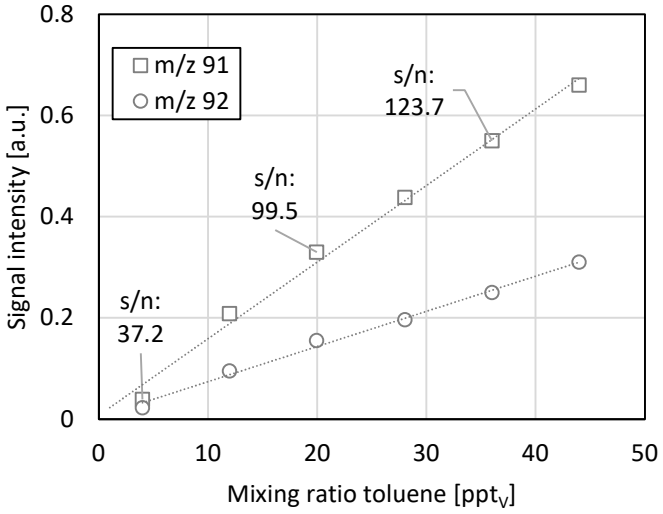

Figure 4.24: LOD of the cage arrangement setup in expansion mode under continuous sampling of toluene with a mixing ratio of 3.3 to 37.3 ppt$_V$; 1 min acquisition time.

For the determination of the LOD, toluene is measured in the range of 3.3 ppt$_V$ to 36.5 ppt$_V$, and the ion signals are averaged over 1 minute. The lower limit of the measured range is limited by the analyte dilution stage. The mixing ratio of the employed toluene mixture is 8.3 ± 0.8 ppb$_V$ and the maximum dilution ratio at a sampling pressure of 600 mbar is 1:2500. Due to this limitation, no measurements near the LOD (S/N ~ 3) can be carried out directly. Thus, the LOD of this system under optimised conditions is determined to be < 3 ppt$_V$ with a signal to noise ratio of 37.

Pulsed analyte sampling

The ion source design allows operation in a pulsed mode. The outer gas inlet of the coaxial design delivers a constant gas flow to stabilise the plasma. The idea is that the plasma performance and the ion chemistry leading to the analyte ions depend only on this gas flow. Thus, the nature of the analyte bulk gas has only a minor influence on the resulting analyte ions. For the pulsed inlet measurements, a three-way valve is used for switching between the analyte and the stabilising gas, which is sampled from the same pressure. The pulse length is varied between 20 ms and 5 s. Helium and nitrogen are used as stabilising gas. The plasma

performance is more stable when the whole system is held at constant gas mixtures. An example measurement is depicted in Figure 4.25.

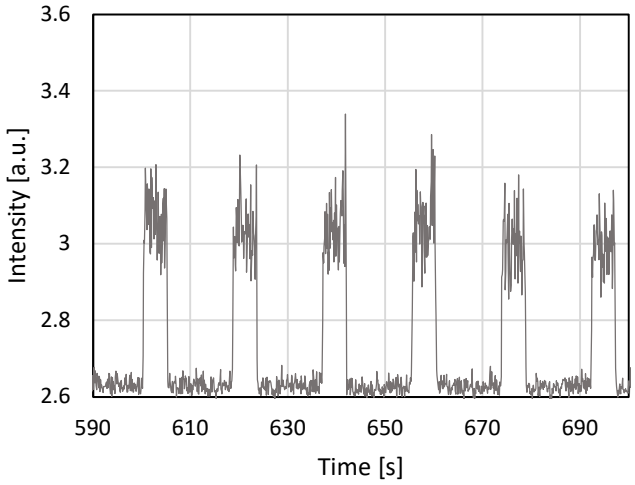

Figure 4.25: Example of the ion signals with the pulsed inlet; 5 s pulse length.

The minimum switching time of the valve is 20 ms. With this short analyte pulse duration, modulation of the plasma is noted during the pulses. Thus, the analyte bulk gas will always have a significant influence in contrast to the initial plan. In charge transfer mode with 208 ppt_V toluene in nitrogen sampled from 600 mbar and helium as sheath/stabilising gas, the ion current is during the pulses 3 – 7 nA and 20 nA in between. Using nitrogen as stabilising gas, the plasma is more stable over the whole measurement and a constant ion current of 3 – 4 nA is recorded. In proton transfer mode with 3‰ hydrogen in helium as sheath gas present, the ion current is 4 - 4.5 nA when nitrogen is used as stabilising gas. When helium is used as stabilising gas, the ion current during the pulses is 3 – 8 nA and 20 – 22 nA in between.

For a determination of the LOD, toluene in nitrogen is varied in the range from 42 ppt_V to 398 ppt_V. The plasma pressure is 560 mbar, the sheath gas is 70 sccm helium, and the analyte is sampled from 600 mbar (70 sccm). The pulse length is 500 ms, and the pulse frequency is 0.2 s^{-1}. The nitrogen stabilising gas is added to the bulk gas of the analyte. The LOD is calculated by averaging the signals for 500 ms of the pulses plus 100 ms before and after, resulting in 700 ms. Ten pulses

are then averaged. The MS is adjusted to provide one data point per 100 ms. The rising and fall time of the signal is well below 100 ms. Thus, by averaging 700 ms per mass spectrum recorded ensures that the whole signal is processed, although the resulting average signal is underrepresented. This procedure results in the LOD being calculated for a total of 7 seconds of acquisition time (Figure 4.26).

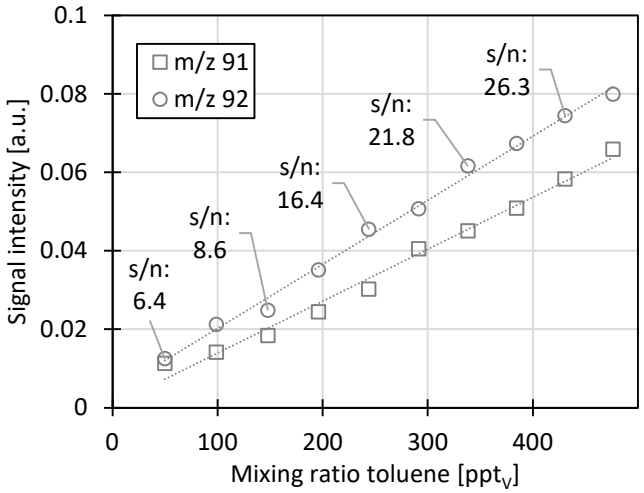

Figure 4.26: LOD of toluene in the cage setup with mixing ratios between 42-398 ppt$_V$; pulsed mode; acquisition of 10 pulses of 700 ms.

The LOD for the charge transfer mode for the M^+ signal is about 50 ppt$_V$ with a signal to noise ratio of 6.4.

Conclusion

The cage arrangement setup and the coaxial inlet are implemented to improve the performance of the free arrangement setup. The seeded plasma mode was the focus of this design work, because it showed a performance well above the expansion mode, in the free arrangement setup. Improvements in performance and stability were addressed. The additional cage electrode allows operating the plasma at a selected potential instead of with reference to the electrical ground of the housing. This is further supported by the new plasma source design with its insulated cap allowing to apply a potential to it. The coaxial inlet is designed to support the plasma with constant stabilising gas flow and thus, operate the plasma

under optimised and constant conditions. The aim was to generate analyte ions independent of the nature of the analyte bulk gas.

The seeded plasma mode could not be performed within this experimental setup under analytical relevant parameters. Instead, the expansion mode is optimised, resulting in even better performance compared to the seeded plasma in the free arrangement setup. The determined LOD value is below 3.3 ppt_V with one minute acquisition time in charge transfer mode.

Mounting a three-way valve upstream to the inlet allows a pulsed sampling of the analyte. The valve allows switching between analyte mixture and stabilisation gas. Thus, modulation of the pressure inside the ion source is avoided. As stabilisation gas helium or nitrogen is used. With helium, the ion currents are higher between the pulses. This does not change the analyte ion signals because the plasma changes significantly faster than the minimum pulse duration. Adapting the stabilisation gas to the analyte bulk gas regarding composition and pressure removes every modulation of the plasma, as observed previously. Thus a constant plasma performance is reached. The LOD of the pulsed mode is determined to be 50 ppt_V with a signal to noise of 6.6 at an acquisition time of 7 s. The much lower acquisition time is a result of the data analysis. For an acquisition time of 1 minute 86 pulses had to be analysed.

Concluding, this setup leads to outstanding performance. However, the proton transfer mode does show significant fragmentation and charge transfer fractions. The latter is because no defined spatial separation of the reaction cascade is implemented as is the case in µ-plici 1.0. Instead, the whole chemistry is in a mixed-up source as present in the free arrangement setup.

4.6.4 µ-plici 2.0

The µ-plici 2.0 setup is the implementation of the three-way design (µ-plici 1.0) on the Sciex API 3200 triple quadrupole MS. The area close to the plasma is designed similarly to µ-plici 1.0 while the orientation to the MS inlet is now axial instead of the perpendicular arrangement on the TOF instrument. The plasma effluent and the analyte are not mixed perpendicularly in front of the skimmer. Instead, the

analyte is added to the reagent ion enriched effluent in a flow tube arrangement directed axially with regard to the central axis of the instrument (Figure 3.8). This change is owing to the minimum footprint approach. This minimisation is meant to allow the substitution of the additional pump since the gas flows is reduced as well. The reagent tube leads to the spatial separation of the reaction cascade. Thus, the metastable species are converted into H_3^+ before the analyte is present, and a high protonation ratio is expected. First measurements show the principal function of this ion source. However, the necessity of pumping as well as a lack of the required pumping speed is evident.

The pressure reached is estimated to be approximately 20 mbar leading to a total number of 50000 - 60000 reactive collisions and thus a low kinetic control. This is verified by the significant water cluster signals present in all measurements with this source. Nevertheless, investigations of this ion source are carried out targeting the pressure issue, the significant water contamination as well as parameters critical for the system performance.

Helium substitution

One aspect of improvement is the substitution of helium. Helium is a limited resource and will thus become expensive in the future. The first attempt is to substitute the helium used for the reagent gas mixture. The He-driven plasma is supposed to be unaltered in this work. Switching from helium to argon changes the reagent reaction cascade to the following:

$$He^M + Ar \rightarrow Ar^+ + He^M + e^- \quad (30)$$

$$Ar^+ + H_2 \rightarrow ArH^+ + H \quad (31)$$

$$ArH^+ + H_2 \rightarrow H_3^+ + Ar \quad (32)$$

H_3^+ remains as primary reagent ion when the reagent gas is in thermodynamic control because argon has a lower proton affinity compared to hydrogen. For this investigation, the hydrogen mixing ration in argon is varied between 3.8% and 38%. The resulting ion signals of nitrogen, toluene, and argon are monitored. The

impact of the substitution of helium with argon in the reagent gas mixture is judged in terms of the protonation ratio of the different species.

The protonation ratios of nitrogen as well as of toluene are above 0.93 and increased slightly with increasing hydrogen mixing ratio. In contrast, argon shows only a protonation ratio of 0.14 increasing to 0.33 (38% H_2). Thus, the postulated reaction cascade is not driven under thermodynamic control resulting in a significant amount of Ar^+, generated in reaction (30), still present in the analyte protonation region. The comparably low protonation ration of argon can be a result of titration of the protonated species with Ar^+ remaining. The high value of the protonation ratios of nitrogen as well as toluene, which are unexpected, can be favoured by the low overall performance of the system leading to ion signals near to the noise level. Further measurements with optimised settings show protonation ratios of toluene under 0.5, which is in accord with the assumption above. Thus, argon supports the charge transfer pathway by generating and transporting unprotonated reagent ions (Ar^+) into the analyte ionisation tube.

In contrast to the ion sources operated on the CTOF, the H_2 gas flow scan in the µ-plici 2.0 setup shows no intensity drop for hydrogen ratios exceeding 1%. Thus, pure hydrogen is used instead of a mixture with helium leading to comparable results and minimising funnelling of non-proton carriers into the analyte region. Compared to the previous setups, the fragmentation of toluene is minimised to nearly zero.

Pressure and kinetic control

Low pressure leading to high volume gas flows and thus low residence time is a critical parameter required for high kinetic control – at the expense of limiting the number of collisions. Unfortunately, the pressure inside the analyte ionisation region is not measured directly but downstream inside the tubing connecting the source and the pump. Thus the measured pressure is not equal to the pressure inside the ion source.

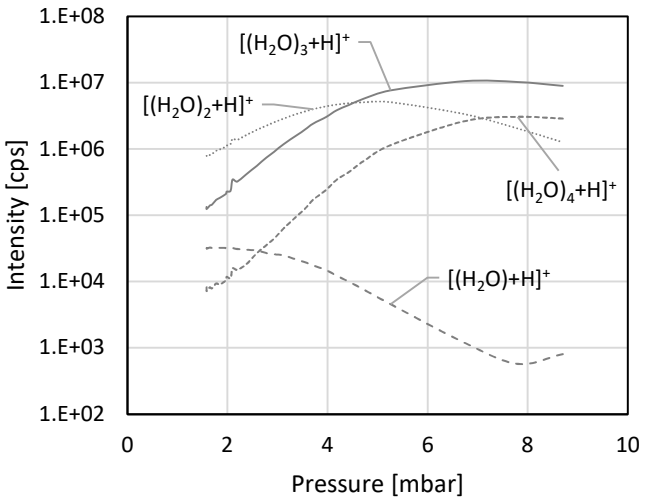

Figure 4.27: Pressure variation in the µ-plici 2.0 source, water cluster signals.

The pressure is varied by reducing the pumping rate with a valve in a range of 1.5 mbar to 9 mbar inside the tubing to the pump. The pressure inside the ion source is estimated to be roughly in the range of 20 – 30 mbar. With increasing pressure, the toluene signals increase. However, the water cluster equilibrium system is shifted to significantly higher cluster sizes (Figure 4.27).

Conclusion

As the first ion source design for the Sciex API 3200 MS, the µ-plici 2.0 source does not reach the requirements for a kinetically controlled protonation source. However, it represents a proof of concept for the adaptation of an AP-MS instrument to be coupled to a low-pressure ion source. It is possible to equip this MS with the proton transfer ion sources.

In addition to the general performance increase by widening the skimmer of the MS to 1 mm orifice diameter, several critical parameters are identified, which must be considered for further designs. First, the use of argon instead of helium as reagent mixing gas has not the expected profit because argon leads to a higher amount of charge transfer species. This result is in contrast to the theoretical model, in which only ArH^+ ions should enter the analyte tube. A possible

explanation is that the reaction time/number of collisions inside the reagent tube is not sufficiently high to maintain the thermodynamic control in this stage.

The measurements also show that the µ-plici 2.0 design no longer needs the dilution of the hydrogen. This suggests a lower risk of backflow effects of hydrogen into the plasma source. Most likely, this change is based on a higher helium flow through the plasma source.

The overall low protonation ratio of this source shows that a backflow of nitrogen into the reagent tube or a not equilibrated reaction cascade of the reagent are a significant issue. The pressure scan demonstrates that the ion source does not meet the requirements. The observed water cluster system has a mean cluster size of 3. The water mixing ratio is estimated to be below 5 ppm_V based on the stated purity of the used gas cylinders. In a kinetically controlled ion source, this leads to smaller cluster sizes (see also Figure 4.31). Water as a possible sink in the reaction cascade has proven to be a significant issue, too. First attempts to remove the water by freezing it out with liquid nitrogen show promising results. In further ion source versions, this is suggested as a standard workaround, but alternative technics must be investigated.

4.6.5 µ-plici 2.1

The µ-plici 2.1 design (Figure 3.9) is the successor of the previous ion source. The low protonation ratio, as well as the lack of thermodynamic control in the reagent cascade, is meant to be eliminated by the change from a tube-based structure to a chamber design. The overall dimensions are held constant.

The new reagent chamber is designed by placing a 200 µm inner diameter aperture at the end of the former reagent tube. Thus, backflow into the reagent zone is limited. The pressure inside the reaction chamber is higher, leading to a higher collision rate and thus more likely to thermodynamic control.

The inner diameter of the aperture of the plasma source is reduced to 50 µm to avoid an increase of the backflow effect of the hydrogen. This decreases the number of metastable species and thus the intensity of the ion signals. For

compensation, the source is equipped with a repelling electrode enhancing the ion sampling rate of the MS and the skimmer is widened further to 2 mm orifice diameter. This and the expected higher protonation ratio and kinetic control inside the analyte chamber is more than countering the loss.

The chamber design allows the optimisation of the different chambers according to pressure and mixing ratios with limited impact on the other reaction areas. Thus, the analyte protonation chamber is operated at much lower pressure. Simultaneously, the reagent chamber allows the formation of reagent ions under thermodynamic control.

Optimisation of the protonation ratio

The main focus of this ion source iteration is the optimisation and maximisation of the protonation ratio. The protonation ratio is defined as the quotient of the protonated analyte signal and the sum of the analyte signals, as discussed in chapter 1.5. With the µ-plici 2.1 setup, the fragmentation of toluene is nearly zero. It is expected that the remaining fragmentation occurs due to direct proton transfer from H_3^+ to toluene. Concomitant fragmentation can be produced by the applied voltages of the primary ion transfer. Thus, the voltages are selected as low as possible to avoid collision-induced dissociation driven by the electric fields. An in-depth investigation of the protonation ratio in dependence on different source parameter is carried out. Besides the different gas flow rates, the pressure inside the analyte protonation camber is a critical parameter.

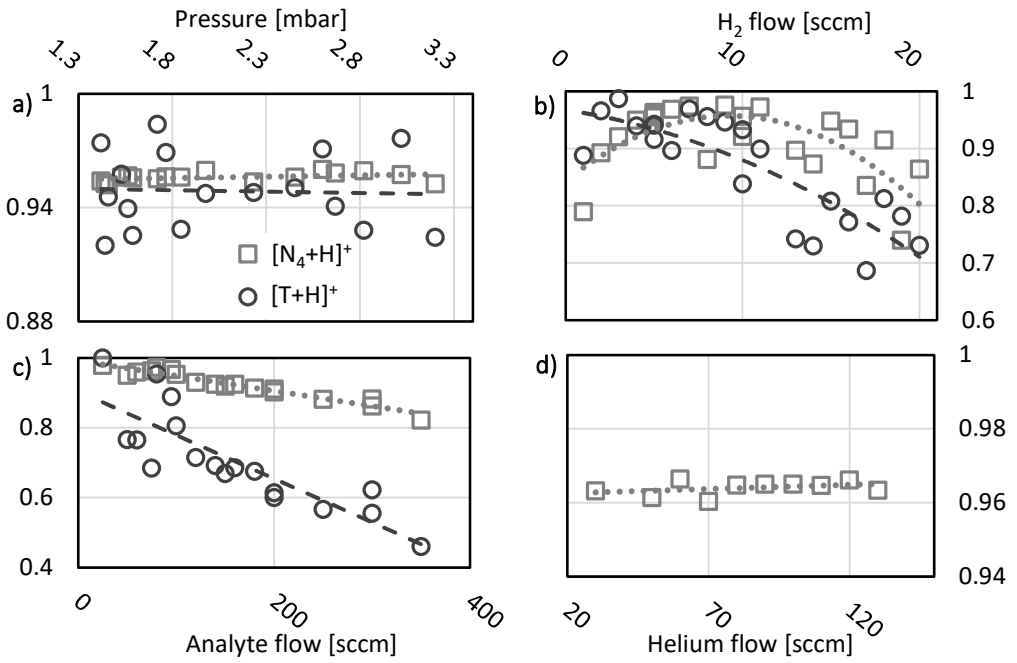

Figure 4.28: Optimization of μ-plici 2.1 in respect to the protonation ratio; a) variation of the pressure inside the protonation chamber (note, that the indicated pressure is the one measured inside the pump tubing), b) variation of the hydrogen flow, c) variation of the analyte flow, d) variation of the helium flow.

The results of this investigation are depicted in Figure 4.28. For the gas flow variations, the pressure inside the analyte protonation chamber is held constant. It should be noted that the reagent chamber pressure is not controlled and thus, not constant in cases of helium and hydrogen flow rate variation.

A variation of the helium gas flow into the plasma source between 25 sccm and 130 sccm does not change the protonation ratio (Figure 4.28, d). For this measurement, the hydrogen flow rate is 7 sccm, the analyte flow rate is 90 sccm, and the analyte protonation chamber pressure is 1.6 mbar.

A variation of the analyte protonation chamber pressure between 1.4 mbar and 3.1 mbar (Figure 4.28, a) leads to no significant change in the protonation ratio. It should be noted that the pressure is measured at the same position as described for the μ-plici 2.0 design. The pumping rate, compared to the predecessor design, is significantly increased by removing the annular space and increasing the tubing

diameter. However, the measured pressure does not equate the analyte protonation chamber pressure. A measurement of this pressure inside the chamber is about 10 – 15 mbar. For this scan, the pressure cannot exceed 3.1 mbar due to the gas load on the vacuum system. The pressure variation is carried out with 7 sccm hydrogen, 100 sccm helium, and 90 sccm analyte flow.

The decreasing protonation ratio with increasing analyte flow at constant pressure (1.5 mbar), 100 sccm helium, and 7 sccm hydrogen (Figure 4.28, c) is assumed to be a backflow effect. With an increasing nitrogen mixing ratio, this effect leads to an increase of non-protonated species from the reagent chamber.

The most interesting variation is the hydrogen flow rate scan with a measured analyte protonation chamber pressure increase from 1.4 mbar to 1.5 mbar, 100 sccm helium flow, and 90 sccm analyte flow rate (Figure 4.28, b). With increasing hydrogen flow into the reagent chamber, the protonation ratio of the nitrogen species increases up to 0.98 at 7 sccm. In contrast, the protonation ratio of toluene seems to decrease over the full range, which is due to the significant variation in the signal intensities in the low sccm range. This variation is caused by the M^+ signal being close to the detection limit and it thus appears only in some measurements while being absent in others. Above 7 sccm hydrogen, the protonation ratio of both, nitrogen and toluene species, decreases again; for the nitrogen species to 0.7 at 20 sccm. Recalling the assumptions made, this is confusing. A higher hydrogen flow leads to a higher pressure inside the reagent chamber. Thus, a higher probability of thermodynamic control and a lower backflow of nitrogen is expected. Both effects lead to a higher protonation ratio since they limit the non-proton carriers entering the protonation chamber.

Taking the water cluster signals into account, a possible explanation is revealed. All water cluster signals monitored (cluster size: 2-4) are increasing with the hydrogen flow rate. The mean cluster size grows from 2.5 to 3, resulting in a reagent chamber effluent with a lower capability to protonate both nitrogen and toluene. It should be noted that the calculated and stated cluster size is based only on the three measured species. The H_3O^+ ion could not be measured, and the $[(H_2O)_5+H]^+$ (m/z 91) receives no consideration because it has the same nominal

mass as $[M-H]^+$ of toluene. Thus, it cannot be identified unambiguously. The overall performance of the ion source is not decreasing with hydrogen flow rates exceeding 7 sccm, indicating no backflow effect of hydrogen into the plasma source.

Pressures

For a better understanding of the water cluster formation and the observed ion distribution, pressure measurements are carried out. The pressure inside the analyte protonation chamber is measured at the analyte inlet. The point of measurement is located approximately 5 cm upstream of the protonation chamber inside the analyte tube. With turned-on analyte flow, the measured pressure is too high through the restricting character of this 5 cm tube. The pressure is measured with only helium and hydrogen flow set to the standard measurement settings and the pumping vale opened. The static pressure inside the analyte chamber is measured to be 6 mbar. The standard value for the analyte flow is equal to the helium flow. Thus, the pressure inside the ion source is estimated to be at least 10 - 15 mbar. This pressure is too high for an analyte protonation under high kinetic control.

For an optimisation of the reagent ion formation, the pressure inside the reagent chamber is investigated. The setup is similar to the one used for the analyte protonation chamber. In contrast to the analyte flow, the influence of the hydrogen flow is negligible. The measurements show that the pressure increases from 70 mbar up to 150 mbar with increasing hydrogen flow from 0 sccm to 20 sccm. At this high pressure, the reagent formation is expected to be under low kinetic control, if not in thermodynamic equilibrium. Inside the reagent chamber, this is desired. Unfortunately, this also favours the formation of water clusters, which represent a sink in the subsequent kinetically controlled analyte protonation.

Water

The fact that water represents a challenge to this ion source type was already discussed in chapter 4.6.4. The ability to generate proton bound water clusters

leads to an increase in proton affinity compared to H_3O^+. While H_3O^+ is still able to protonate most analytes (e.g. toluene), the clusters beginning with $[(H_2O)_2+H]^+$ have much lower reactivity and thus, will "trap" the proton leading to a reduced sensitivity of the system. For high pressures and long reaction times, the clusters are still able to protonate toluene because H_3O^+ is always replenished through the cluster equilibrium. However, the amount of H_3O^+ available through this pathway is very small. In conventional ion sources, the cluster system $[(H_2O)_n+H]^+$ is strongly shifted n = (1 … 3) in the first pressure reduction with higher field gradients. Ionisation of the present analyte occurs mostly in this stage. An alternative technology utilises the water clusters for ionisation using a drift tube equipped with an electric field of 100-150 Td.[33] This shifts the cluster distribution to nearly solely H_3O^+ (n = 1) which is able to ionise the targeted analytes. However, to reduce CID induced fragmentation, the electric field gradients inside the µ-plici 2.1 ion source as well the primary ion transfer are chosen to be as low as possible. Also, a desired kinetic control inside the analyte protonation chamber will not allow the cluster system to replenish H_3O^+ ions. Thus, being able to ionise a significant amount of analyte requires the avoidance of cluster formation inside the reagent chamber. To investigate the influence of water present in the reagent chamber, simulations of the reaction kinetics as well as measurements, are carried out.

For the measurements, the hydrogen gas flow is directed through a cooling trap containing water. This setup is cooled down by either placing the trap into liquid nitrogen, a mixture of solid CO_2 in acetone or a cryostat, depending on the desired temperature. With this combination of cooling techniques, a temperature range of 77 K to 272.5 K is covered, resulting in a water vapour pressure range of $1{\cdot}10^{-19}$ mbar (estimated) to 6 mbar. The hydrogen tubing is held at 1230 mbar, giving a water mixing ratio range of $8{\cdot}10^{-17}$ (estimated) to $5{\cdot}10^{4}$ ppm_V. The used flow parameters are set to the standard values.

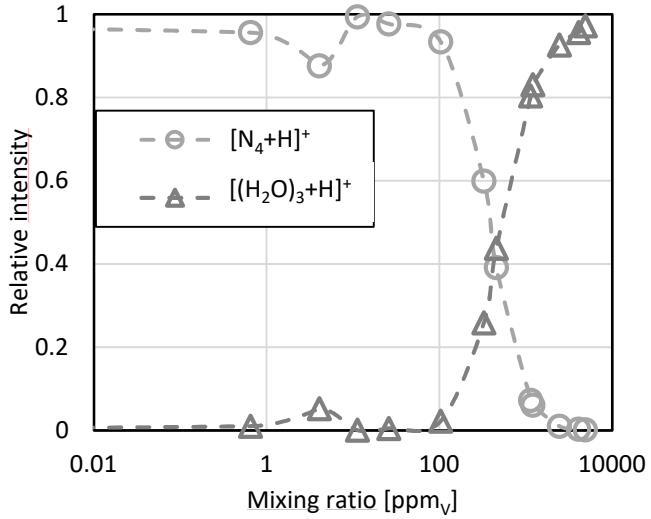

Figure 4.29: Relative ion signals of reagent ion $[N_4+H]^+$ and water cluster representative $[(H_2O)_3+H]^+$ as a function of the water mixing ratio inside the reagent chamber of μ-plici 2.1 setup in the range of 0.01 to 5 ·10⁴ ppm_V.

The effect of increasing mixing ratios of water on the source performance is judged by analysing the ion signal of the N_2H^+ reagent ion reservoir species N_4H^+ and the proton bound water cluster $[(H_2O)_3+H]^+$ signal, chosen as representative for the entire cluster system. As is seen in Figure 4.29, where the relative intensities of the mentioned species are plotted, the water cluster signal rapidly decreases with decreasing water mixing ratio below 1000 ppm_V. Then it slowly decreases further. The N_4H^+ signal is inversionally proportional, indicating the expected shift between protons being trapped in the water cluster system. Following the reasoning above, water has a higher proton affinity as nitrogen. Therefore, with high water mixing ratios, N_2H^+ protonates water leading to cluster formation. At very low water mixing ratios, N_2H^+ reacts with the abundantly present N_2 to form N_4H^+ ions rather than protonating water. The results indicate a tolerable water mixing ratio of up to 100 ppm_V. Thus, the water cluster signals recorded in analyte measurements (without any removal of water) are more likely caused by leaks rather than by the water mixing ratio present in the gas supply. It should be noted that the N_4H^+ signal increases further with lower water mixing ratio, which is not depicted in Figure 4.29. This indicates a lower tolerable water mixing ratio as assumed above. Thus, simulations of the reaction system are carried out with varying water mixing ratios allowing a closer inspection of this behaviour.

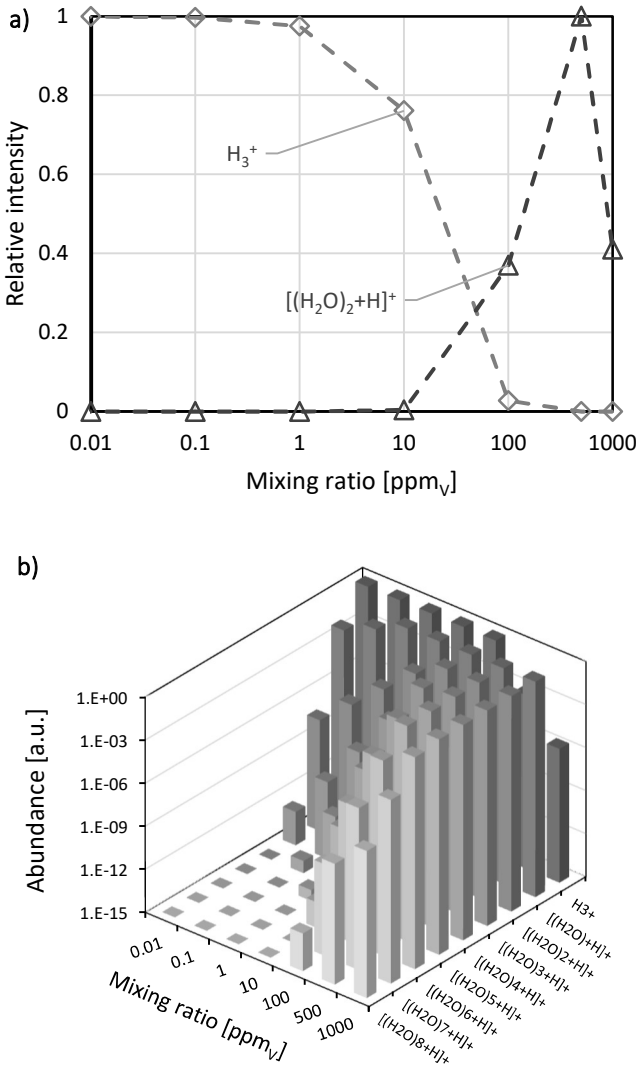

Figure 4.30: Simulated proton bound water cluster distribution plotted against the water mixing ratio inside the ion source; a) view comparable to Figure 4.29, b) logarithmic scale, all simulated cluster species.

The reaction system simulated for this theoretical investigation consists of helium metastables, hydrogen and the proton bound water cluster chemistry (Table 3). The results are depicted in Figure 4.30, where the abundance of each proton bound water cluster is given in dependency of the neutral water mixing ratio. For comparison, the H_3^+ mixing ratio is given. The H_3^+ ions are the targeted reagent ions being able to ionise the analytes in the subsequent chamber. Thus, the target of the optimisation of the reagent chamber is the maximisation of the H_3^+ output. As mentioned above, the water cluster system is not able to ionise the analyte under kinetically controlled conditions, leading to the necessity of minimisation of

the second and higher water clusters. H_3O^+ is not regarded as a sink of protons since its proton affinity is smaller than that of targeted analytes. Following this reasoning, the simulations suggest a maximal tolerable water mixing ratio of approximately 10 ppm_V. At this value, the abundance of the $[(H_2O)_2+H]^+$ water cluster is 2 orders of magnitude lower than the reagent ion H_3O^+. However, under these conditions, the water mixing ratio is required to be significantly lower when the analyte mixing ratios are below the ppb_V range. It should be noted that this is based on a high kinetic control inside the protonation chamber minimizing the impact of neutral water entering with the analyte gas flow. Nevertheless, the kinetic control of the µ-plici 2.1 setup is not sufficiently high this scenario as can be deduced from the measured pressures and the total number of collisions of around 100000.

To visualise the influence of the pressure inside the analyte chamber, this reaction system is simulated with a fixed water mixing ratio of 1000 ppm_V.

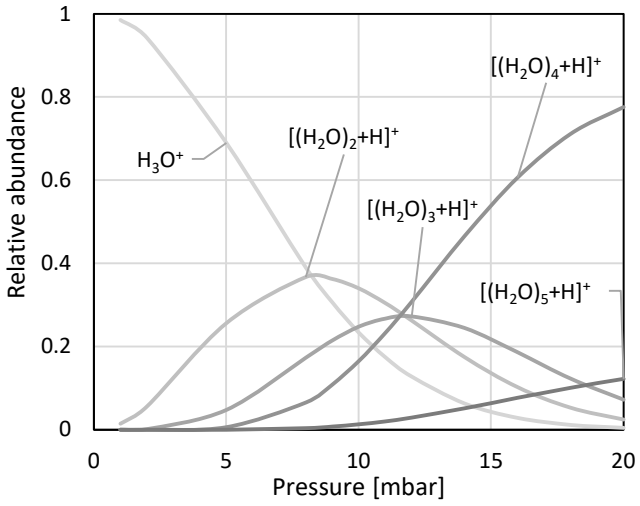

Figure 4.31: Simulation of the water cluster distribution inside the protonation chamber in dependence of the pressure in the range of 1 to 20 mbar; water mixing ratio 1000 ppm_V.

The result (Figure 4.31) suggests that the pressure has to be in the low mbar range to avoid water cluster formation in the analyte chamber, especially since the simulated humidity is well below ambient conditions. For a pressure of 10 mbar

and higher, the cluster distribution rapidly reaches a mean cluster size of 2 … 4. Taking into consideration the measured pressures, the water variation measurement, and the results of the simulations, all data are in accord. The analysis suggests that the ion source has to be as tightly sealed as possible and that water needs to be removed from all gas flows supplied by appropriate cool trapping to avoid water cluster formation. Also, the µ-plici 2.1 source does not meet the expectations for a high kinetic control, since the pressure is too high and thus supporting adverse water cluster formation.

Analytical performance

The µ-plici 2.1 setup shows significantly improved performance as compared to its predecessor. Especially the protonation ratios are in the desired range. Therefore, the analytical performance in terms of LOD, linear dynamic range, and protonation ratio is investigated in depth. To determine reliable LODs, dilution experiments are performed using 10 ppb_V and 10 ppm_V mixtures of toluene as well as BTX in nitrogen. Further dilution using the dynamic mixing stage is realised by using a 100 sccm MFC for the analyte mixture and a 2000 sccm MFC for nitrogen (cf. Figure 3.14). The determination of LODs is carried out with 100 sccm as well as 150 sccm analyte volume flow into the ion source. Thus, the maximum mixing ratios are calculated to be 9.5 ppm_V and 6.4 ppm_V for flow rates of 100 sccm and 150 sccm, respectively. The minimal mixing ratio provided by the dilution setup is 5 ppt_V calculated using the nominal mixing ratio of the mixtures. Based on the mixing ratio of xylene (cf. Table 4), the minimum mixing ratio accessible is 1.3 ppt_V.

Due to the adverse effects of water as discussed , these measurements can only be performede with liquid nitrogen cooled traps in the gas supply lines. Prior to each measurement, the ion source is operated approximately 30 - 60 minutes to ensure consistent performance. The LODs are calculated according to DIN 32645[72], applying the linear regression generated with 4 minutes averages for each titration step. The recorded ion signals are the sum of the ± 0.5 $^m/_z$ intervals around the recorded nominal masses.

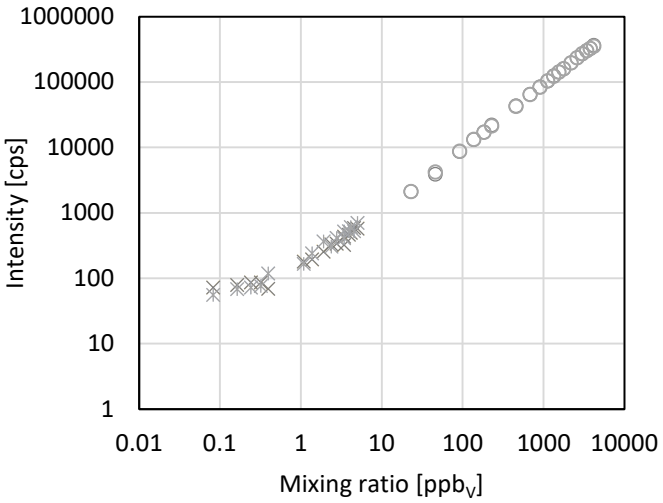

Figure 4.32: Dilution curve of the toluene analyte mixture; two data sets for "10 ppm" and "10 ppb", respectively; measured on the µ-plici 2.1 setup with 100 sccm analyte flow; logarithmic scaling.

For toluene as the analyte, the MS is operated in scanning mode with a total scan time of 10 s per mass spectrum between 10 and 100 $^{m}/_{z}$. Thus, one nominal mass interval is recorded for 0.11 s. During the 4 minutes observation time, each nominal mass is recorded for 2.6 s. Thus, the LOD is based on 2.6 s signal averaging. The resulting slopes show excellent linearity in the ppm_V range and acceptable performance in the ppb_V range (cf. Figure 4.32). Combining these two measurements, a significant inconsistency of the resulting slope at approx. 0.6 ppb_V is observed, suggesting the LOD to be in this range.

The optimisation attempts regarding the protonation ratio as discussed above (Figure 4.28) suggest that the measurements with 150 sccm analyte flow should result in less favourable LODs. The protonation ratio decreases significantly upon an increase in the analyte flow rate from 100 sccm to 150 sccm. Thus, it is expected for the LOD to be lower with 100 sccm because the LOD is calculated using the $[M+H]^+$ signal. This expected behaviour is represented in the LOD calculated by the signal to noise ratio of 3. With 150 sccm analyte flow rate, the S/N-LOD is 1.5 ppb_V, whereas for 100 sccm the LOD is significantly lower at 0.6 ppb_V.

Using BTX as analyte leads to an additional focus regarding the kinetic control of the system. With only toluene as analyte present, it represents the species with the highest proton affinity. With BTX, the targeted analytes can react with each other

resulting in an ion distribution differing from the neutral composition. The BTX measurements are carried out with the MS scanning 10-150 $^{m}/_{z}$ for 10 s for the ppm_V range. Thus, each nominal mass is recorded over 0.07 s to create a full mass spectrum. In the 4 minutes average time, each nominal mass is recorded for 1.7 s. In the ppb_V range, this scanning method is not suitable due to the short record time per nominal mass. Thus, the ppb_V range is recorded with the multiple ion scan method allowing to select specific nominal mass intervals which are recorded throughout 1 s each. For a 4 minutes average time and 4 selected nominal masses, an observation time and therefore a LOD for 1 minute is obtained.

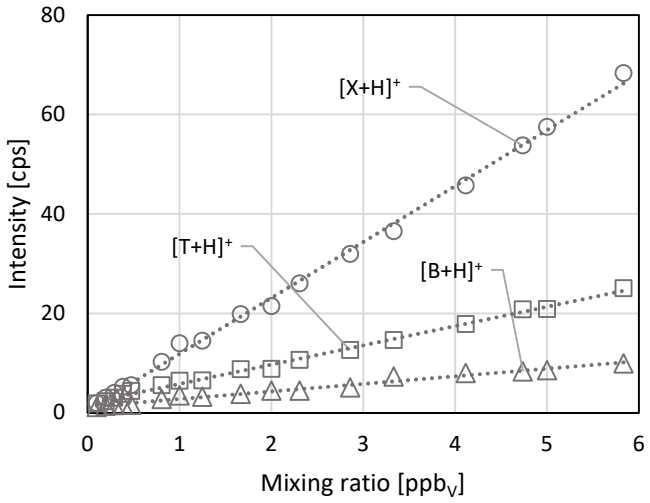

Figure 4.33: Determination of limit of detection on BTX mixture in ppb_V range; 150 sccm analyte.

In the ppb_V range, good linearity is observed, resulting in limits of detection of 0.33 ppb_V for toluene, 0.27 ppb_V for benzene and 0.73 ppb_V for xylene (Figure 4.33), respectively. The lower LOD, in comparison with the toluene measurements, is reasoned in the 23 times longer observation time. The significant different slopes are due to the different rate constants for the analyte ion formation reaction (Table 3).

In the ppm_V range, the linear trend is only be observed for xylene, while benzene and toluene show a curve (Figure 4.34). The reason for this observation is the low kinetic control inside the protonation chamber of this setup. Caused by the high

pressure, the protonated analytes can interact with neutral analyte still present. Thus, benzene can protonate toluene and xylene, and toluene itself protonates xylene.

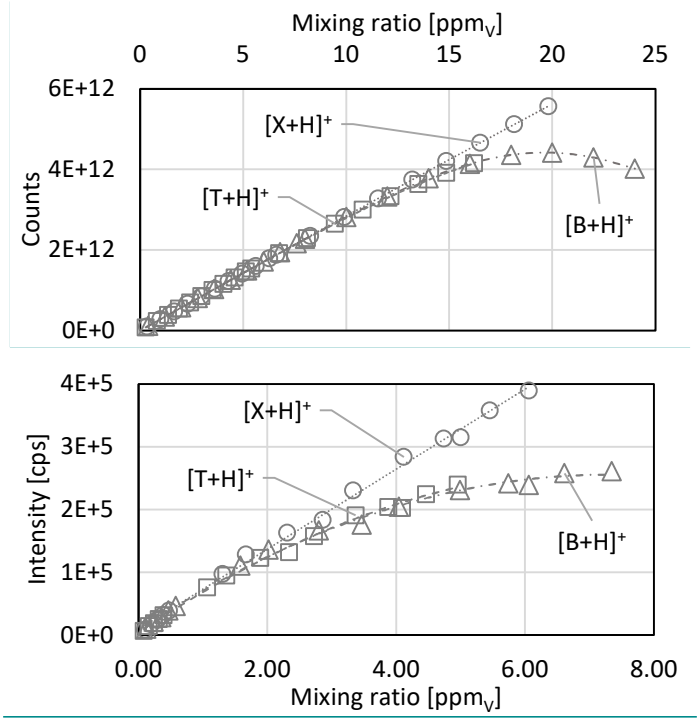

Figure 4.34: BTX in the ppm_V range; the curved trend for benzene and toluene; top: Simulation, bottom: Measurement.

The low kinetic control limits the linear range of the system at higher mixing ratios when multiple analyte species are present. For the μ-plici 2.1 setup this limitation is in the lower ppm_V range, where the slopes of benzene and toluene show a significant deviation from the expected linear trend.

To validate these results, simulations with the program package Cantera[67] are carried out with the estimated parameters pressure (10 mbar) and reagent ion mixing ratio (10 ppm_V) (Figure 4.34 top). The result depicts the observed non-linear response for the benzene and toluene ion signals. It is noted that the mixing ratios between the simulation and the measurement differ, but qualitatively the two results agree well. The differences in the mixing ratios is readily explained by

an overestimated reagent ion mixing ratio or an underestimated pressure inside the analyte protonation chamber.

Proton capacity

Compared to the ion sources on the CTOF, the different reaction regions of the µ-plici 2.1 source have smaller volumes. It is expected that this has a significant impact on the proton capacity. The toluene mixing ratio is measured between 1.3 ppm_V and 400 ppm_V to determine this influence. The helium flow inside the plasma source is set to 100 sccm, the hydrogen flow inside the reagent chamber to 5 sccm, and the analyte flow is held at 100 sccm.

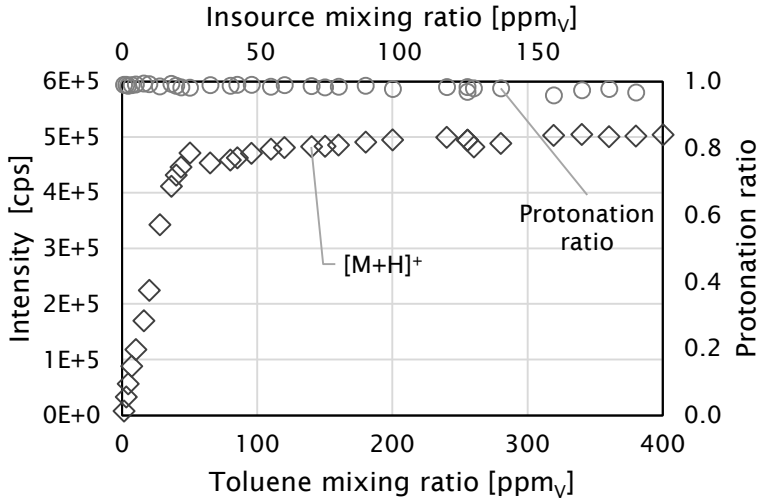

Figure 4.35: Protonation capacity of the µ-plici 2.1 setup; Titration of toluene from 1.3 ppm_V up to 400 ppm_V (top axis is insource mixing ratio); Protonation ratio (on secondary axis).

The $[M+H]^+$ signal of toluene shows a linear response up to 50 ppm_V and then saturates. This indicates that the µ-plici 2.1 setup has a proton capacity of approximately 50 ppm_V sampled mixing ratio. This corresponds to 25 ppm_V in-source mixing ratio.

The lower proton capacity of µ-plici 2.1 in comparison to µ-plici 1.0 (exceeded 100 ppm_V in-source, chapter 4.6.2) may be caused by various factors. Either the

total number of reagent ions inside the analyte protonation chamber or the kinetic control is lower. As mentioned in chapter 3.4.2, the pressure inside the protonation chamber is assumed to be between 10 mbar and 15 mbar, and the calculated number of collisions is 100000. Thus, kinetic control is not as high as envisioned. The number of reagent ions present in the analyte protonation chamber depends on the production rate of metastable helium species by the plasma source, the thermodynamic control inside the reagent chamber and the overall losses on the passage to the analyte chamber. The H_3^+ production rate of the two setups (µ-plici 1.0 and 2.1) cannot be measured independently. However, in a first approximation based on the volume flows, the total amount of metastable species reacted with the hydrogen is lower in the µ-plici 2.1 setup. Also, due to the smaller volume of the source, the loss of reagent ions in µ-plici 2.1 is assumed to be higher.

Kinetic and thermodynamic control

In addition to the high protonation ratio, the kinetic control of the analyte protonation is in focus of this ion source development. To investigate this figure of merit, different approaches are made. First, the observed ion distribution yields information on the type of control under which the ions are formed. Second, the ion source geometry, in combination with the volume flows, allows a rough estimation of the reaction time. With the measured pressures, the number of collisions can be calculated. As is described in chapter 4.1, this number of collisions provides a possible classification of the extent of kinetic control.

For the observation of the effects of low kinetic control, a mixture of different analytes is beneficial. Thus, a mixture of benzene, toluene and xylene (BTX) is used. This mixture allows the proton transfer from benzene and toluene onto xylene, resulting in a non-linear response of these two ion signals, as shown in Figure 4.34. Analysing the BTX mixture at a constant mixing ratio and increasing the pressure inside the ion source results in a clear anti-correlation of the signal intensities (Figure 4.36).

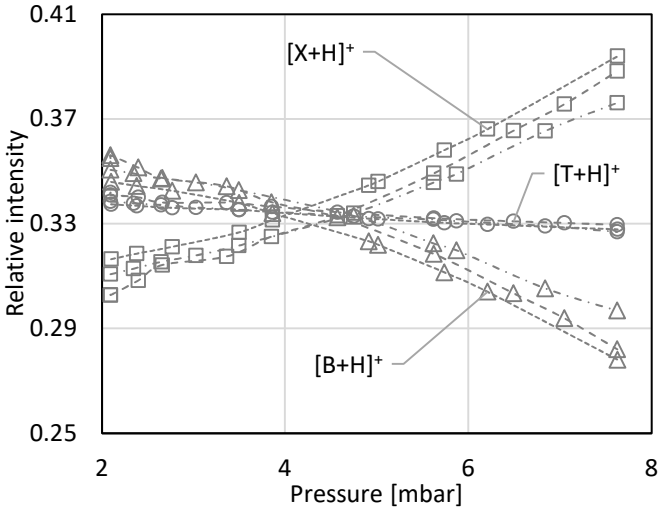

Figure 4.36: Pressure variation in µ-plici 2.1; analyte/analyte interaction of BTX mixture.

With increasing pressure, the benzene signal decreases while the xylene signal increases. The toluene signal remains stable, revealing the reaction pathway: While xylene is protonated by both benzene and toluene, toluene can only protonate xylene, and only benzene can protonate both. This is in agreement with the proton affinities of this species (see Table 1). This measurement shows the influence of the pressure on the kinetic control and additionally, the lack of the needed low pressure for a high kinetic control in this particular ion source version. As mentioned above, the pressure is still too high for a clean kinetically controlled protonation and has to be improved in the next ion source iteration.

Ion current measurements

For a better understanding of the sensitivity loss caused by the apertures used for the separation of the chambers and the influence of the ring electrode, ion current measurements are carried out using the experimental setup depicted in chapter 3.5.

By increasing the helium flow rate, the measured ion current increases, which is most likely due to reduced losses to the walls or due to a higher metastable production of the plasma (Figure 4.37).

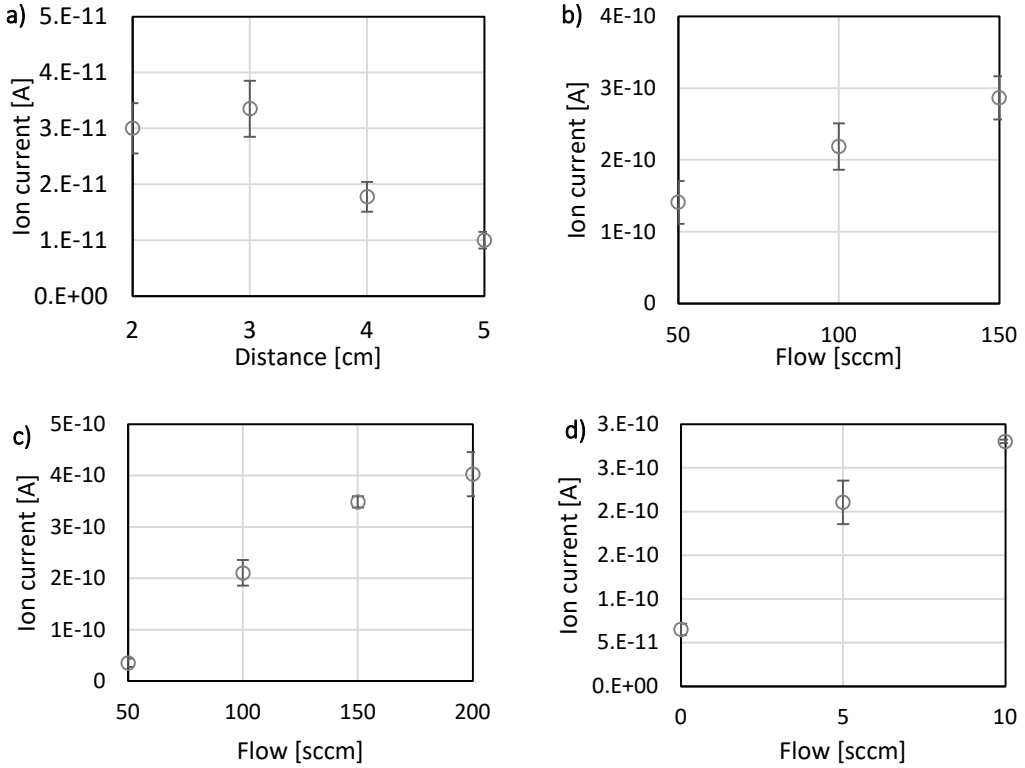

Figure 4.37: Ion current measurements µ-plici 2.1 setup (cf. Figure 3.11); a) distance behind the reagent chamber, b) variation of analyte flow, c) variation of helium flow (plasma source), d) variation of hydrogen flow.

In addition to the helium flow, the analyte flow, as well as hydrogen flow rates, have a positive influence on the ion current. This is most likely due to a transformation of the helium metastables into ionic species (with longer lifetimes) and due to lower wall losses. Interestingly, the ion current is significantly decreasing with the distance between the reagent chamber exit and the measurement electrode. Nevertheless, taking the conical analyte protonation chamber geometry into account and normalisation of the measured ion currents with the inner diameter of the analyte protonation chamber at the measuring position, the decrease of the ion current is no longer significant and can be explained by wall losses. It should be noted that the absolute currents are not comparable between the variation in distance and the flow variations, because of different source settings.

Other reagents

Within the ion source region, only weak electric field gradients are present. Additionally, the ionisation cascade begins with species having a lower proton affinity as water. This allows water to be protonated, leading to proton bound water cluster formation, which represents a strong proton sink. Reducing the water mixing ratio in the non-kinetically controlled chambers discriminates against this cluster formation. Also, the employed analytes contain only low water mixing ratios when mixed from gas cylinders with < 5 ppm_V water contamination. However, analysing ambient air samples results in massive water cluster signals as described earlier. This is caused by the pressure inside the analyte protonation chamber being not low enough. Also, the exothermic proton transfer from H_3^+ to analytes exhibiting high proton affinities often results in fragmentation of these analytes.[71] This process lowers the protonation ratio and contradicts the envisioned construction of a non-fragmenting pure protonating ion source. To reduce ionisation induced fragmentation, the reaction enthalpy of the analyte protonation step must be reduced.

One possible option for solving both problems is to utilise reagents with higher proton affinities, thus narrowing the gap of the proton affinities between reagent and analytes. Additionally, this allows suppressing protonation of matrix gas species such as nitrogen, and thus considerably lowering the corresponding mass signals. In turn, no electronic ion signal suppression (e.g. with a notch filter) is needed. The water cluster formation can be suppressed by using a reagent species with higher proton affinity as water. However, this lowers the range of possible analyte as well. Nitrogen can be suppressed by using methane as a reagent. methane is commonly used as CI reagent gas. This appears to be attractive, as a multitude of reference mass spectra is available, and the ion-molecule reaction chemistry is well known (equations 2-6). However, the classical EI driven CI sources suffer from unfavourable ion-molecule chemistry. A possible explanation is the fragment formation of the methane reagent chemistry (equations 2). To verify this problem, methane is investigated as reagent gas in the µ-plici 2.1 ion source (Figure 4.38). An advantage of the plasma-based H_3^+ source method is the formation of solely protonated methane, leading to only CH_5^+ reagent ions and not

a mixture of CH_5^+ and $C_2H_5^+$ as it is the case in EI driven CI sources. Also, it bypasses the fragment formation route, possibly solving the impurity problems.

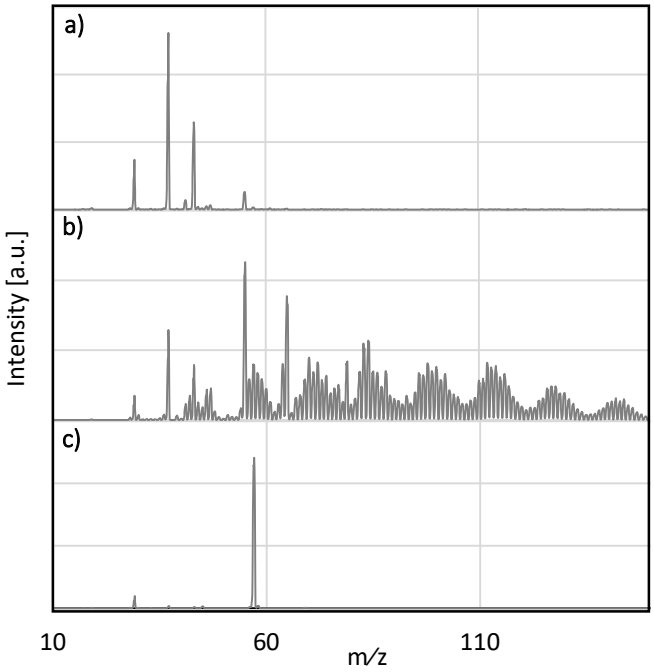

Figure 4.38: µ-plici 2.1 with methane as an alternative reagent; a) H_2 as reagent and methane as the analyte, b) methane as a reagent and N_2 as the analyte, c) H_2 as a reagent and N_2 as an analyte; Intensity equally scaled.

Without methane and only nitrogen as the analyte, water can be efficiently removed in all gas supply lines. Consequently, only N_2H^+ and N_4H^+ are observed (Figure 4.38 c). Using methane as analyte water cluster signals are dominant. Due to the higher proton affinity of water and the discrimination of low m/z values by the ion optics of the mass spectrometer, no CH_5^+ (m/z 17) are observed (Figure 4.38 a). The massive water cluster formation results from the higher water content of the used methane in combination with the inability to completely freezing it out, which is prevented by the significant lower vapour pressure of methane in comparison to nitrogen, helium, and hydrogen. Using methane as reagent without hydrogen present, massive C-H corresponding ion signals are observed (Figure 4.38 b). It is assumed that these ionic species are formed by the reaction cascade presented for EI ionisation (equation 2-6). Even more complex chemistry can be

driven compared to the desired clean, controlled protonation transfer, due to the fragmentation of the reagent in the primary ionisation step.

Conclusions

With the µ-plici 2.1 setup, a chamber based ion source design is introduced. This separation of different sections of the reaction cascade into physical chambers allows the optimisation of each section with only limited influence on the others. Therefore, the reagent ion formation can be operated under more thermodynamic control while the pressure inside the analyte protonation chamber can still be at its minimum. This results in a higher protonation ratio because due to the longer reaction time in the reagent chamber non-proton carriers are titrated. Concomitantly, the reagent ion mixing ratio within the source effluent is assumed to be lower compared to the predecessor source. By implementing the ring electrode, this loss of sensitivity can be compensated to a certain extent.

Due to the robust working conditions provided by this source, more investigations were carried out addressing primary reagent ion mixing ratios, proton capacity, and alternative reagents. In principle, methane can be used as a reagent to suppress protonated nitrogen species. It has been shown that the utilisation of hydrogen as first reagent being able to protonate further reagents is a good approach for a controlled pure proton transfer based reaction cascade. Thus, fragmentation due to strongly exothermic proton transfer steps are suppressed. This will also solve the susceptibility of the system regarding residual water if the chosen reagent has a higher proton affinity.

The successful modelling of the experimental results with kinetic simulations demonstrates the principal capability of the simulations as well as the accurate approximations about different starting parameters.

Reliable limits of detection were measured with this system showing the dramatic influence of a low kinetically controlled analyte protonation section. Thus, further improvements in the pressure reduction of the protonation chamber have to be made to maintain a high kinetic control and enable to represent the distribution of the neutral analyte ensemble accurately.

Ion current measurements reveal no significant loss of ions to the walls over the distance from reagent chamber to the skimmer. Nevertheless, the conical geometry of this source leads to a lower ion current sampled by the skimmer. Thus, a cylindrical geometry of the analyte protonation chamber should be favoured although this precludes a fast decrease of the pressure along this chamber.

4.6.6 µ-plici 2.2 stacked chamber system

The successor of the 2.1 setup is constructed for further investigations of the stepwise reduction of the exothermicity of the analyte protonation reactions to achieve a fragment free operation. As an improvement to all predecessors, the pumping rate is increased significantly, pressure control is implemented in each chamber to obtain reliable data, and the ring electrode is further improved increasing the sensitivity of the system.

The new implementation allows static pressure monitoring in each chamber. Also, the analyte protonation chamber is equipped with two pressure monitoring ports, one at the analyte inlet and the other close to the skimmer. This allows achieving a more accurate understanding of the pressure gradient inside this chamber.

For investigations on alternative reagents, an additional chamber is implemented between the former reagent chamber, which is now called primary reagent chamber and the analyte protonation chamber. This new chamber is used for secondary reagents to minimise excess energy, improve the selectivity of the system if needed and to solve the issues with residual water.

Pressure control

In the previous ion source designs the pressure control, especially inside the analyte protonation chamber, was insufficient. Thus, the pumping rate is increased significantly in this version. Also, each chamber is equipped with a second port, which is designed to be used for pressure measurements. The pressure information of each chamber is used for a reasonable prediction of the chemistry taking place. Additionally, this allows the determination of the pressures inside

further versions, in which a pressure measurement was not possible due to geometric restrictions.

The additional inlets allow to monitor the static pressure inside a selected chamber and changing the volume flows in parallel without any influence as it was in previous pressure measurements (see chapter 4.6.5).

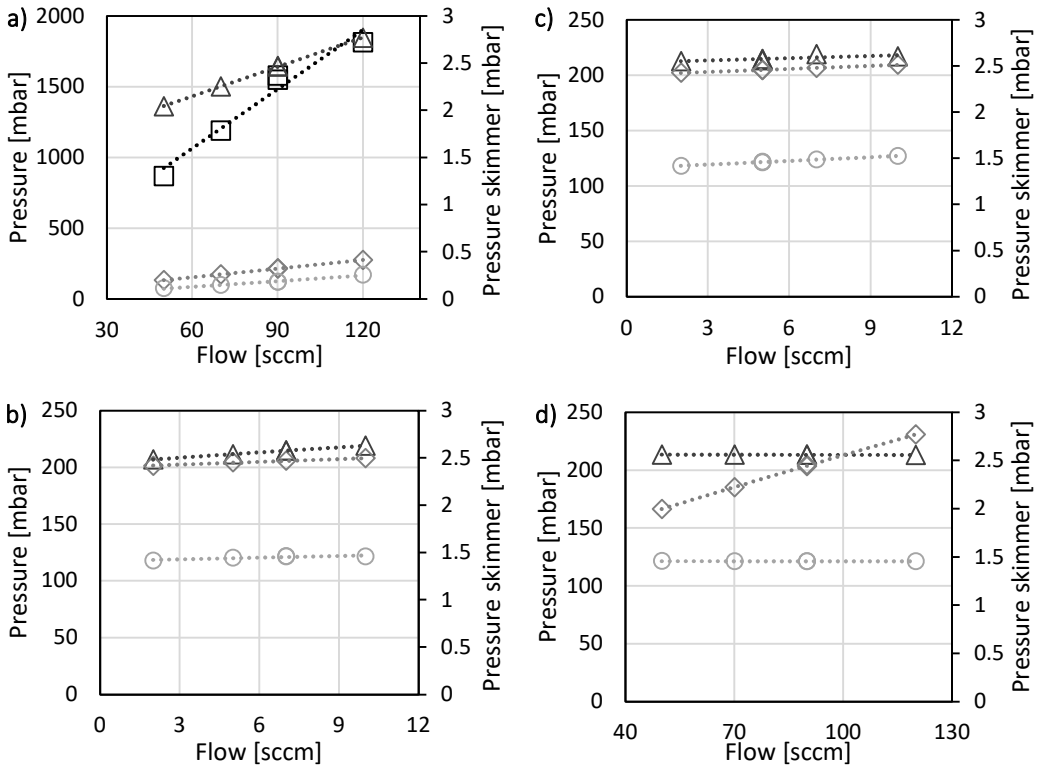

Figure 4.39: Pressures of µ-plici 2.2 measured at different positions: □ plasma source, ◇ primary reagent chamber, ○ secondary reagent chamber, △ skimmer chamber; secondary axis for the pressure inside the primary reagent chamber; inlet flow variation in a): plasma source, b): primary reagent chamber, c): secondary reagent chamber, d): analyte protonation chamber; plasma source pressure is constant and not depicted in b), c), and d).

As expected, the variation of hydrogen and reagent gas flows have the same influence on the pressure in these two chambers. Increasing the pressure in one chamber leads to the same increase in each chamber upstream to the targeted one (Figure 4.39). Varying the analyte flow rate should, therefore, influence all chambers. Increasing the analyte volume flow from 50 sccm to 120 sccm increases the pressure inside the analyte protonation chamber from 2 mbar to 2.7 mbar.

Concomitantly, no significant changes in pressures of the other chambers is noticed. It is assumed that this is due to the relatively small changes which are lower than the margins of error. Increasing the secondary reagent flow raises the pressure inside the secondary as well as in the primary reagent chamber by the same amount while enhancing the hydrogen flow has only a small influence on the secondary reagent chamber pressure (Figure 4.39 b).

Overall, this ion source shows the desired performance regarding the measured pressures. The pressure inside the protonation chamber is in the low mbar range, and an increase in pressure inside one of the other chambers leads to only small changes of the protonation chamber pressure. This allows the optimisation of the chemistry inside the individual chambers without adverse impact on the downstream chambers.

3 chamber system - chemical blending

The new chamber is designed for adding a secondary reagent. This reagent is protonated by H_3^+ in the first step resulting in solely protonated reagent ions with a higher proton affinity. This process minimises the fragmentation of the analyte ions caused by the excess energy of the protonation reaction. Since the electric field gradients inside the ion source and primary ion optics are held as low as possible, this design is expected to provide a fragment less ionisation means. Also, a higher proton affinity of the reagent limits the range of analytes being able to protonate. On the one hand, this is unfavourable when the particular analyte has a low proton affinity (e.g. noble gases), on the other hand, this can be useful for suppressing the protonation of matrix gas molecules. Different reagent gases (methane, *i*-butane, trifluoroacetic acid, and trifluoroethanol) are investigated to determine their use as bulk gas ionisation suppressing agents.

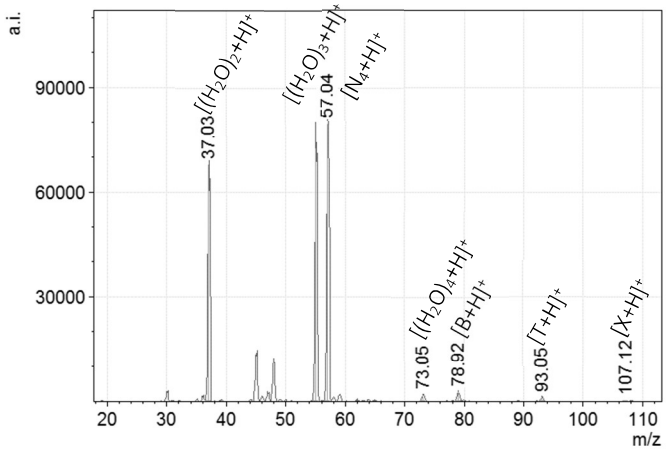

Figure 4.40: Reference mass spectrum µ-plici 2.2 3-chamber version; He 90 sccm, primary reagent (H_2) 5 sccm, secondary reagent (H_2) 5 sccm; analyte (BTX 10 ppb_V in nitrogen) 150 sccm.

hydrogen is used as primary and secondary reagent creating a reference experiment to compare the influence of the above mentioned secondary reagents. It should be noted, that this changes primarily the reaction time for the H_3^+ reagent ion formation by a factor 3 as in both chambers identical chemistry is proceeding. This doubles the reaction time, and due to the now higher pressure in the primary reagent chamber (as compared to the hydrogen chamber in the µ-plici 2.1 setup), the overall factor approaches 3. All gas supply lines are cooled, but due to the significantly higher reaction time for reagents in the 3-chamber version, the formation of water clusters cannot be entirely suppressed (Figure 4.40). However, a strong signal at m/z 57 is observed; this signal is most likely representing the reagent reservoir ion N_4H^+.

Methane

methane as an alternative reagent was initially investigated using the µ-plici 2.1 setup (see chapter 3.4.2). However, in the two-chamber design, methane can only be used as reagent ionised directly by the helium metastables, resulting in a significant amount of fragmentation and CH_3 radical chemistry. In the µ-plici 2.2 setup, methane is protonated via H_3^+ primary reagent ions avoiding the fragmentation caused by the energy-rich metastable species. The difference in proton affinities between hydrogen and methane is 121.2 kJ/mol, which is far

below the dissociation energy of CH_4 (422.8 kJ/mol). Therefore, no fragmentation is expected. The resulting analyte protonation chemistry is comparable to the classical CI experiments with a wide range of analytes but known fragmentation of proton affine analyte molecules.[6, 20, 22] The advantage of methane as the secondary reagent is the probability of leaving nitrogen as primary matrix gas unaffected. Thus, in the protonation chamber only reactions between reagent and analyte as well as the ionised analyte and the neutral analyte of higher proton affinity are expected to take place.

For these experiments, pure methane is added into the reagent chamber with different volume flow rates to optimise the system's performance. Due to the low purity of the methane, many different signals representing the impurities are detected. The high water mixing ratio and the higher reaction time compared to the µ-plici 2.1 version leads to significant water cluster formation. The water clusters are represented in Figure 4.41 by the signals of $[(H_2O)_2+H]^+$ (m/z 37), $[(H_2O)_3+H]^+$ (m/z 55), and $[(H_2O)_4+H]^+$ (m/z 73), which have an at least 10 fold higher intensity as compared to analyte or methane signals. The initial idea of leaving nitrogen unaffected works as predicted as neither N_2H^+ nor N_4H^+ signals are observed.

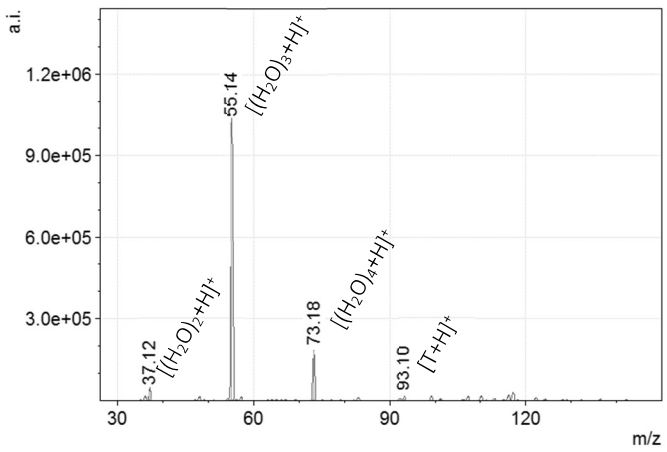

Figure 4.41: Spectrum µ-plici 2.2 3-chamber version; He 90 sccm, primary reagent (H_2) 5 sccm, secondary reagent (CH_4) 5 sccm; analyte (toluene 10 ppm_V in nitrogen) 120 sccm.

Nevertheless, the performance as judged by the analyte signal intensity is significantly lower than that of both, the μ-plici 2.1 version, and the reference measurement with a factor of 1000 lower toluene mixing ratio (Figure 4.40).

Isobutane

isobutane as a reagent cannot ionise such a wide range of analyte as methane but does not protonate water[13], which represents a significant proton sink. Also, isobutane is known to show more distinct fragmentation chemistry in CI sources.[13] The protonation by H_3^+ should minimise this behaviour as it is discussed above for methane. However, dissociative proton transfer reactions with H_3^+ have been reported.[21]

To investigate the performance of isobutane, it was used as a secondary reagent gas and toluene as an analyte. For a better study of the reagent gas itself, measurements with pure nitrogen as an analyte are carried out, too. The measurement results show multiple signals in the mass spectrum, rendering isobutane impractical as reagent gas, due to its low purity (Figure 4.42). Additionally, isobutane shows the same behaviour as methane in the μ-plici 2.1 setup (Figure 4.38), which suggests that either the H_3^+ as primary reagent ion fragments it or the impact of the plasma in the secondary reagent chamber is still significant in this setup. The letter can be ruled out since methane does not show this fragmentation (Figure 4.41), and the protonation ratio seems to be comparable high (Figure 4.40).

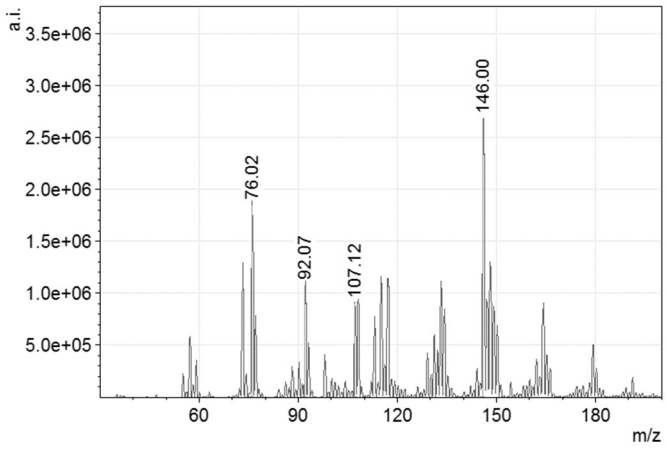

Figure 4.42: Spectrum µ-plici 2.2 3-chamber version; He 90 sccm, primary reagent (H_2) 5 sccm, secondary reagent (isobutane) 1.8 sccm; analyte (toluene 10 ppm_V in nitrogen) 90 sccm.

The expected primary reagent ion mixing ratio is about 7 – 15 ppm_V regarding the investigations mentioned in chapter 4.2. Thus, a mixture of isobutane in helium should lead to a good performance by minimising the fragmentation chemistry encountered when using pure isobutane. Newsome et al. showed a similar effect by using a 10%$_V$ mixture of isobutane in argon.[13] To validate this report, a mixture of 8.5%$_V$ of isobutane in helium was investigated. The resulting mass spectra show a significantly lower amount of high m/z signals corresponding as compared to the pure isobutane ion chemistry (Figure 4.43).

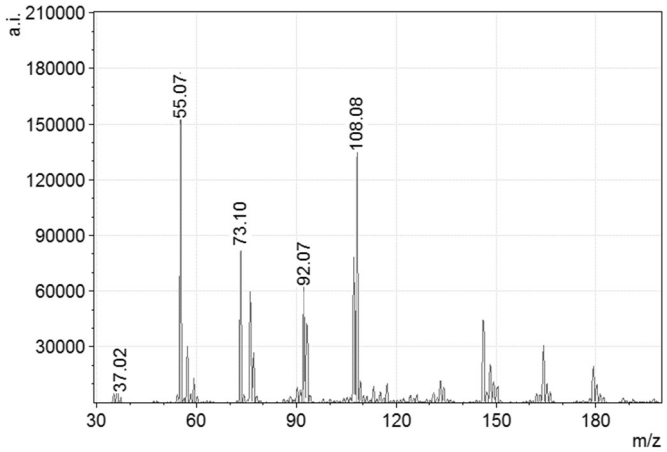

Figure 4.43: Spectrum µ-plici 2.2 3-chamber version; He 90 sccm, primary reagent (H_2) 7 sccm, secondary reagent (isobutane 8.5 % in helium) 2 sccm; analyte (toluene 10 ppm_V in nitrogen) 90 sccm.

Unfortunately, this mixture seems not to be able to inhibit water cluster formation completely. Although the signals of impurities are much smaller and fewer, the $^{m}/_{z}$ 93 signal is not unequivocally identified as $[M+H]^+$ of toluene.

Trifluoroacetic acid and trifluoroethanol

As alternative reagents, trifluoroacetic acid (TFA; 114 $^{g}/_{mol}$) and trifluoroethanol (TFE; 100 $^{g}/_{mol}$) are investigated to inhibit water cluster formation. At the same time, they have proton affinities similar to water and therefore, prove a wide range of accessible analytes, comparable to PTR-MS. Additionally, these two molecules are stable compared to most of the other compounds with similar proton affinities. In contrast to isobutane, massive impurities and ion chemistry products are not expected, leading to the clean protonation of the analytes.

In a first attempt, the headspace of the two liquid reagents was sampled by passing helium over them. The saturated gas phase is then added to the reagent chamber.

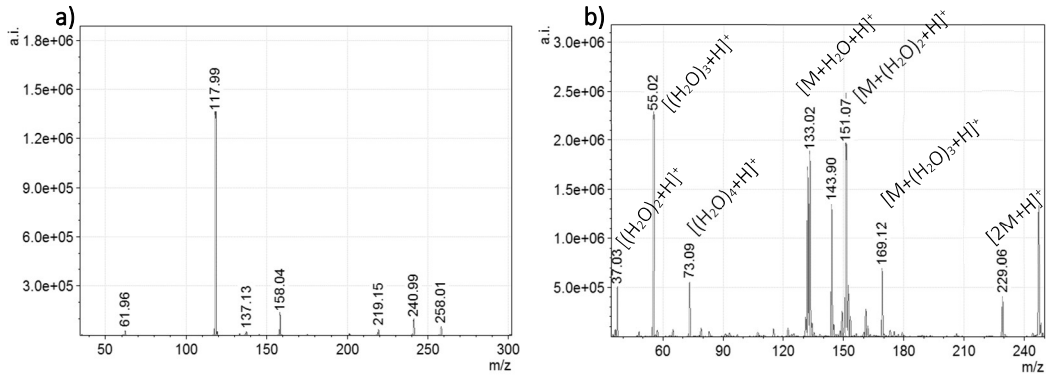

Figure 4.44: Spectra μ-plici 2.2 3-chamber version; He 90 sccm, primary reagent (H_2) 5 sccm, secondary reagent (liquid sampling with helium a): TFE, b): TFA) 5 sccm; analyte (toluene 10 ppm_V in nitrogen) 90 sccm.

Although the proton affinity of both trifluoroethanol and trifluoroacetic acid is higher than that of water, water cluster formation is still observed with trifluoroacetic acid (Figure 4.44 b), while trifluoroethanol seems to suppress it (a). This is interesting because trifluoroacetic acid has a higher proton affinity

(711.7 kJ/mol) compared to the Ethanol analogue (700.2 kJ/mol). Both mass spectra show no M^+ or $[M+H]^+$ ions of the reagents, but water adducts of the type $[M+(H_2O)_n+H]^+$ and dimeric reagent species. These two observations show clearly that both the reagent and the water mixing ratio, are too high in these experiments. The latter can be reasoned by the non-tight arrangement, which can cause significant amounts of ambient air leaking into the reagent chamber. Also, trifluoroethanol shows a simpler mass spectrum with lower to no water cluster signals. Thus, trifluoroethanol was mixed with helium (saturated) to have a closed setup similar to the isobutane and methane measurements.

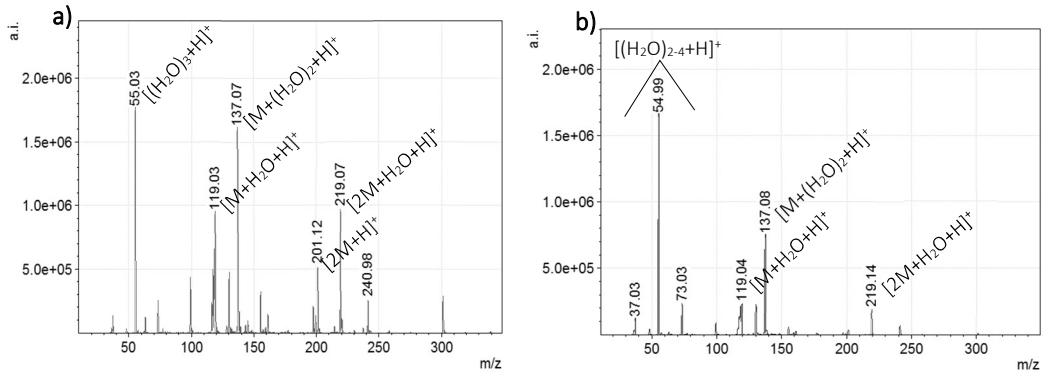

*Figure 4.45: Spectra µ-plici 2.2 3-chamber version; He 90 sccm, H_2 5 sccm, Reagent (TFE in helium **a):** saturated vapour pressure; **b):** 150 ppm) 5 sccm; toluene 10 ppm_V 90 sccm.*

With trifluoroethanol (saturated) as the reagent, no M^+ or $[M+H]^+$ is observed (Figure 4.45 a). For better identification of the different signals, fragmentation experiments were carried out using the collision cell. The dominating species are found to be water clusters (e.g. $^m/_z$ 55) or mixed trifluoroethanol/water clusters (e.g. $[M+H_2O+H]^+$ ($^m/_z$ 119), $[M+(H_2O)_2+H]^+$ ($^m/_z$ 137), $[2M+H]^+$ ($^m/_z$ 201), $[2M+H_2O+H]^+$ ($^m/_z$ 219)). These clusters are expected to be relative unreactive according to direct analyte protonation similar to the pure water clusters. Thus, the mixing ratio is diluted further, and a 150 ppm_V mixture is used (Figure 4.45 b). Even with this degree of dilution, dimeric reagent species are observed. Concomitantly, pure water clusters, as well as the above mentioned mixed clusters, are present. In all approaches with the trifluoro compounds, no analyte signals were unambiguously identified.

Two-chamber version

Besides the additional chamber for reduction of excess energy, this ion source is designed to temper all problems appeared in previous versions. Thus, the µ-plici 2.2 design also allows the operation as a two-chamber version analogue to its predecessors.

The principal dimensions are identical to the µ-plici 2.1 version except for the protonation chamber surrounding the skimmer. It was optimised to allow for an increased pumping rate together with a better focusing by the redesigned ring electrode. Also, the protonation chamber is of cylindrical shape to decrease the reaction time. Due to these changes, the performance should be improved in comparison to the predecessor version allowing this ion source to sample ambient air. The comparison of measurements with only nitrogen as the analyte shows the changes in reaction time regarding the reagent ion species. While the two-chamber version of µ-plici 2.2 shows solely N_2H^+ ion signals, the µ-plici 2.1 leads to N_4H^+ as the dominant signal.

N_4H^+

As shown in the previous ion source versions, N_4H^+ acts as a reservoir species for the reagent N_2H^+ ion. Due to the mass discriminating ion optic of the MS instrument, it was in most mass spectra the sole signal corresponding to the reagent ions. Measurements with a variation of the nitrogen mixing ratio suggest the N_4H^+ as a reservoir species formed by N_2H^+ and molecular nitrogen. This clustering reaction is also supported by the literature.[73–75]

By increasing the pressure above 1.9 mbar inside the protonation chamber, the N_4H^+ signal increases sharply (Figure 4.46). This increase is shaped equally to the increase in water cluster signals, indicating third-order kinetics. In contrast, the N_2H^+ signal decreases only slightly.

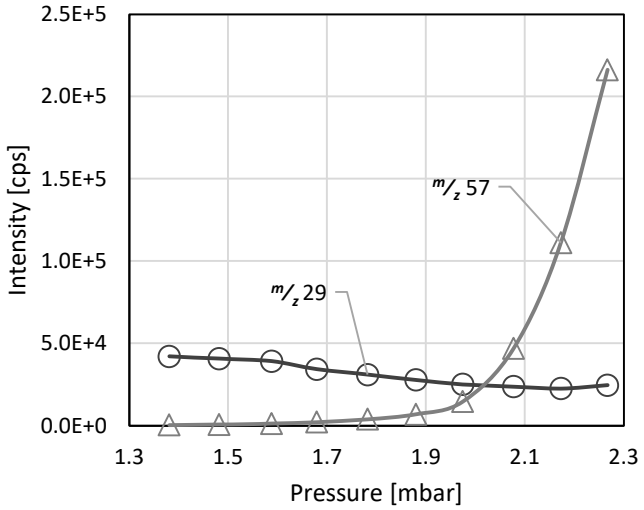

Figure 4.46: N_2H^+ and N_4H^+ signals depending on the pressure inside the 2 chamber version of µ-plici 2.2.

It is assumed that this is due to the mass discriminating primary ion transfer optic of the MS leading to overall small signals in the low m/z range. During the entire experiments and with the µ-plici 2.2 source in general, no charge transfer species, e.g. N_2^+ N_4^+, were observed. This provides evidence that the N_4H^+ species is formed by N_2H^+ and molecular nitrogen.

Conclusion

The µ-plici 2.2 design allows sufficient pressure reduction to maintain the desired kinetic control for the analyte protonation. Also, the focusing efficiency of the ring electrode is improved. The two-chamber setup shows promising performance compared to the former designs. In the three-chamber setup, the benefit of the new reagent chamber for chemical blending and reducing of the excess energy could not be validated so far, due to lack of suitable reagents. Isobutane, as well as methane, have not the required high purity. The trifluoro compounds show no fragmentation and have the required proton affinity to suppress water cluster signals but at the same time have a too high polarity, resulting in cluster formation with water. Concomitantly, the tested mixing ratios are too high, allowing the formation of dimers. Both, the dimers as well as mixed clusters, are expected to have a too low reactivity for an analyte protonation.

5 Conclusion and outlook

In this work, six ion source designs of a plasma-based chemical ionisation ion source were built and coupled to two different mass spectrometers. One aim was the recorded mass spectra to depict the neutral molecule distribution as close as possible. For that purpose, simulations were carried out, giving a good overview of the quantification of kinetic and thermodynamic control. In CI, the mass spectrum can only represent the neutral ensemble under high kinetical control, which is defined to have a maximal difference between ion and neutral ensemble of 20%. Also, these simulations helped in the following iterative optimisations of the µ-plici ion source series. A second aim was the control over the type of ionisation reaction with the focus on a pure proton transfer reaction. For that purpose, protonation capacity and protonation ratio were introduced as figures of merit for more straightforward classification of the ion sources.

On the time of flight MS by TOFWERK, three different ion sources based on the plasma source by PAC and the first differential pumping stage of the MS were designed. Based on the initial ("free") setup, an improved design incorporating a cage electrode for improved plasma operation was built. Both utilised an expansion mode as well as a seeded plasma mode of operation. Especially the cage arrangement setup showed excellent analytical performance with a limit of detections in the low ppt_V range. Also based on the free arrangement setup, the first version of the µ-plici series was designed by equipping the plasma source with a T-piece like nozzle allowing the addition of reagent gasses to control the ion-molecule chemistry. This allows the protonation of analytes diluted in air or

nitrogen. In contrast, both the free and the cage arrangement setup only protonate analytes diluted in hydrogen.

Based on the µ-plici 1.0 source, a whole series of ion sources was designed in an iterative process on a SCIEX API3200 triple quadrupole instrument. Using a mass spectrometer dedicated for sampling from atmospheric pressure requires the modification of the inlet system. In this work, it was successfully demonstrated that the AP instrument could be modified to sample from the lower mbar range present in the µ-plici ion sources. The three ion sources built for the API3200 also implement a stepwise improved control of the ionisation process by using a cascaded chamber design. The µ-plici 2.x ion sources showed clearly the importance to limit the number of collisions inside the protonation chamber, as the kinetic control simulations predict. This behaviour was significantly improved over the three iterations by improving the pressure control in the protonation chamber resulting in µ-plici 2.2 being able to operate under high kinetic control. Also improved over these iterations was the thermodynamic control inside the reagent chamber and the separation of the different chambers suppressing leakage of undesired charge transfer species, e.g. N_2^+, He^+, H_2^+. The µ-plici 2.2 ion source design allows the implementation of a third chamber used for a secondary reagent to limit the amount of excess energy available in the analyte protonation reaction. In the course of this work, several possible reagents were tested, rendering the purity and capability to form mixed water clusters a critical parameter for future experiments.

The various results achieved on the different ion source versions represent proofs of concepts for further ion source developments. Especially the cage arrangement and the µ-plici 2.2 are regarded as blueprints. The former for high sensitivity with less focus on controlled chemistry, and the latter for chemistry control and high kinetic control. Exploring the idea of the µ-plici series, further work should focus on an improved MS coupling or on using an MS instrument dedicated for low-pressure sampling. Also, the search for secondary reagents should be continued. Here, specific applications can utilise different reagents. The formation of water clusters needs to be limited with a cleaner reagent setup.

For analytical use, the plasma performance should be investigated in more detail, and the produced ion current should be controlled for signal stability. Utilising a discharge in pure hydrogen allows for the substitution of the helium as a limited resource. Based on the results presented in this thesis, it should also be possible to use a mixture of clean, dry air and hydrogen, and thus utilizing N_2H^+ as reagent ion. This will lower limitations for the ion source operation in light of explosives regulations.

6 Abbreviations

µ-plici	micro plasma induced chemical ionisation
AP	atmospheric pressure
APCI	atmospheric pressure chemical ionisation
APPI	atmospheric pressure ionisation
B	Benzene
BTX	a mixture of benzene, toluene, and xylene
CI	chemical ionisation
CID	collision induced dissociation
CT	charge transfer
DA	dopant assisted
DA-APPI	dopant assisted atmospheric pressure photo ionisation
DART	direct analysis in real time
DC	direct current
DIA	distribution of ion accaptance
EI	electron ionisation
EP	entrance potential
ESI	electrospray ionisation
FAPA	flowing atmospheric pressure afterglow
FT	Fourier transform
GB	Gas phase basicity
GC	gas chromatograph
ID	inner diameter
LOD	limit of detection
LTP	low-temperature plasma
M	molecular ion (analyte)
MFC	mass flow controller
MS	mass spectrometer
Nd:YAG	neodymium-doped yttrium aluminium garnet
PA	proton affinity
PC	proton capacity
PEEK	poly ether ether ketone
PI	photo ionisation
PR	protonation ratio
PS	plasma source
PT	proton transfer
PTR	proton transfer reaction
QIT	quadrupol ion trap
R	reagent ion
RF	radio frequency
S/N	signal to noise ratio
T	toluene
TIC	total ion count
TOF	time of flight
UV	ultraviolet
VOC	volatile organic compounds
VUV	vacuum ultraviolet

7 List of Figures

8 List of Tables

9 References

1. Munson, B.: CIMS, Chemistry in Mass Spectrometry. Int. J. Mass Spectrom. 377, 502–506 (2015). doi:10.1016/j.ijms.2014.03.015

2. Field, F.H.: Chemical ionization mass spectrometry. Acc. Chem. Res. 1, 42–49 (1968). doi:10.1021/ar50002a002

3. Munson, M.S.B., Field, F.H.: Chemical Ionization Mass Spectrometry. I. General Introduction. J. Am. Chem. Soc. 88, 2621–2630 (1966). doi:10.1021/ja00964a001

4. Munson, B.: Chemical ionization mass spectrometry. Anal. Chem. 43, 28A-42A (1971)

5. Munson, B.: Chemical ionization mass spectrometry: ten years later. Anal. Chem. 49, 772A-775A (1977). doi:10.1021/ac50017a001

6. Harrison, A.G.: Chemical Ionization. CRC Press, Inc., Boca Raton (1983)

7. McLuckey, S.A., Mentinova, M.: Ion/Neutral, Ion/Electron, Ion/Photon, and Ion/Ion Interactions in Tandem Mass Spectrometry: Do We Need Them All? Are They Enough? J. Am. Soc. Mass Spectrom. 22, 3–12 (2011). doi:10.1007/s13361-010-0004-9

8. Kersten, H., Funcke, V., Lorenz, M., Brockmann, K.J., Benter, T., O'Brien, R.: Evidence of Neutral Radical Induced Analyte Ion Transformations in APPI and Near-VUV APLI. J. Am. Soc. Mass Spectrom. 20, 1868–1880 (2009). doi:10.1016/j.jasms.2009.06.014

9. Dempster, A.J.: LII. The ionization and dissociation of hydrogen molecules and the formation of H 3. Philos. Mag. Ser. 6. 31, 438–443 (1916). doi:10.1080/14786440508635520

10. Thomson, J.J.: Bakerian Lecture: Rays of Positive Electricity. Proc. R. Soc. A Math. Phys. Eng. Sci. 89, 1–20 (1913). doi:10.1098/rspa.1913.0057

11. Thomson, J.J.: XIX. Further experiments on positive rays. Philos. Mag. Ser. 6. 24, 209–253 (1912). doi:10.1080/14786440808637325

12. Munson, B.: Chemical Ionization Mass Spectrometry: Theory and Applications. In: Encyclopedia of Analytical Chemistry. John Wiley & Sons, Ltd, Chichester, UK (2000)

13. Newsome, G.A., Steinkamp, F.L., Giordano, B.C.: Isobutane Made Practical as a Reagent Gas for Chemical Ionization Mass Spectrometry. J. Am. Soc. Mass Spectrom. 27, 1789–1795 (2016). doi:10.1007/s13361-016-1463-4

14. Subba Rao, S.C., Fenselau, C.: Evaluation of benzene as a charge exchange reagent. Anal. Chem. 50, 511–515 (1978). doi:10.1021/ac50025a036

15. Wilson, M.S., Dzidic, I., McCloskey, J.A.: Chemical ionization mass spectrometry of nucleosides. Biochim. Biophys. Acta - Nucleic Acids Protein Synth. 240, 623–626 (1971). doi:10.1016/0005-2787(71)90722-2

16. Jelus, B.L., Munson, B., Fenselau, C.: Reagent gases for G.C.-M.S. analyses. Biol. Mass Spectrom. 1, 96–102 (1974). doi:10.1002/bms.1200010203

17. Arsenault, G.P.: Mixed Charge Exchange–Chemical Ionization Reactant Gases in High-Pressure Mass Spectrometry. J. Am. Chem. Soc. 94, 8241–8243 (1972). doi:10.1021/ja00778a056

18. Čermák, V.: Retarding-Potential Measurement of the Kinetic Energy of Electrons Released in Penning Ionization. J. Chem. Phys. 44, 3781–3786 (1966). doi:10.1063/1.1726534

19. Lundeen, C.V., Viscomi, V.S., Field, F.H.: Determination of nitrogen-15 by chemical ionization mass spectrometry. Anal. Chem. 45, 1288–1290 (1973). doi:10.1021/ac60329a046

20. Herman, J.A., Harrison, A.G.: Effect of reaction exothermicity on the proton transfer chemical ionization mass spectra of isomeric C 5 and C 6 alkanols. Can. J. Chem. 59, 2125–2132 (1981). doi:10.1139/v81-307

21. Ausloos, P., Lias, S.G.: Proton-Transfer Reactions between H3+ and Saturated Hydrocarbons. J. Chem. Phys. 40, 3599 (1964). doi:10.1063/1.1725059

22. Tsang, C.W., Harrison, A.G.: Chemical ionization of amino acids. J. Am. Chem. Soc. 98, 1301–1308 (1976). doi:10.1021/ja00422a001

23. Odiorne, T.J., Harvey, D.J., Vouros, P.: Chemical ionization mass spectrometry using tetramethylsilane. J. Phys. Chem. 76, 3217–3220 (1972). doi:10.1021/j100666a020

24. Robb, D.B., Covey, T.R., Bruins, A.P.: Atmospheric pressure photoionization: An ionization method for liquid chromatography-mass spectrometry. Anal. Chem. 72, 3653–3659 (2000). doi:10.1021/ac0001636

25. Kauppila, T.J., Kostiainen, R.: Dopant-assisted atmospheric pressure photoionization. In: Gross, M.L. and Caprioli, R.M. (eds.) The Encyclopedia of Mass Spectrometry. pp. 223–229. Elsevier, Oxford (2007)

26. Horning, E.C., Horning, M.G., Carroll, D.I., Dzidic, I., Stillwell, R.N.: New picogram detection system based on a mass spectrometer with an external ionization source at atmospheric pressure. Anal. Chem. 45, 936–943 (1973). doi:10.1021/ac60328a035

27. Carroll, D.I., Dzidic, I., Horning, E.C., Stillwell, R.N.: Atmospheric Pressure Ionization Mass Spectrometry. Appl. Spectrosc. Rev. 17, 337–406 (1981). doi:10.1080/05704928108060409

28. Moini, M.: Atmospheric pressure chemical ionization: principles, instrumentation, and application. In: Gross, M.L. and Caprioli, R.M. (eds.) The Encyclopedia of Mass Spectrometry. pp. 344–353. Elservier, Oxford (2007)

29. Carroll, D.I., Dzidic, I., Horning, E.C., Stillwell, R.N.: Atmospheric Pressure Ionization Mass Spectrometry. Appl. Spectrosc. Rev. 17, 337–406 (1981). doi:10.1080/05704928108060409

30. Dzidic, I., Carroll, D.I., Stillwell, R.N., Horning, E.C.: Comparison of Positive Ions Formed in Nickel-63 and Corona Discharge Ion Sources Using Nitrogen, Argon, Isobutane, Ammonia and Nitric Oxide as Reagents in Atmospheric Pressure Ionization Mass Spectrometry. Anal. Chem. 48, 1763–1768 (1976). doi:10.1021/ac50006a035?

31. Hunter, E.P.L., Lias, S.G.: Evaluated Gas Phase Basicities and Proton Affinities of Molecules: An Update. J. Phys. Chem. Ref. Data. 27, 413–656 (1998). doi:10.1063/1.556018

32. Hogness, T.R., Lunn, E.G.: The Ionization of Hydrogen by Electron Impact as Interpreted by Positive Ray Analysis. Phys. Rev. 26, 44–55 (1925). doi:10.1103/PhysRev.26.44

33. Ellis, A.M., Mayhew, C.A.: Proton Transfer Reaction Mass Spectrometry. John Wiley & Sons, Ltd, Chichester, UK (2014)

34. Hansel, A., Jordan, A., Holzinger, R., Prazeller, P., Vogel, W., Lindinger, W.: Proton transfer reaction mass spectrometry: on-line trace gas analysis at the ppb level. Int. J. Mass Spectrom. Ion Process. 149–150, 609–619 (1995). doi:10.1016/0168-1176(95)04294-U

35. Blake, R.S., Monks, P.S., Ellis, A.M.: Proton-Transfer Reaction Mass Spectrometry. Chem. Rev. 109, 861–896 (2009). doi:10.1021/cr800364q

36. Kebarle, P., Searles, S.K., Zolla, A., Scarborough, J., Arshadi, M.: Solvation of the hydrogen ion by water molecules in the gas phase. Heats and entropies of solvation of individual reactions. H+(H2O)n-1 + H2O → H+(H2O)n. J. Am. Chem. Soc. 89, 6393–6399 (1967). doi:10.1021/ja01001a001

37. Sonderfeld, H.: Charakterisierung und Einsatz eines PTR-ToF-MS zur Messung von flüchtigen organischen Verbindungen Dissertation Fachbereich C : Mathematik und Naturwissenschaften. (2013)

38. Weston, D.J.: Ambient ionization mass spectrometry: Current understanding of mechanistic theory; Analytical performance and application areas. Analyst. 135, 661–668 (2010). doi:10.1039/b925579f

39. Huang, M.-Z., Yuan, C.-H., Cheng, S.-C., Cho, Y.-T., Shiea, J.: Ambient Ionization Mass Spectrometry. Annu. Rev. Anal. Chem. 3, 43–65 (2010). doi:10.1146/annurev.anchem.111808.073702

40. Chen, H., Gamez, G., Zenobi, R.: What Can We Learn from Ambient Ionization Techniques? J. Am. Soc. Mass Spectrom. 20, 1947–1963 (2009). doi:10.1016/j.jasms.2009.07.025

41. Cody, R.B., Laramée, J.A., Durst, H.D.: Versatile New Ion Source for the Analysis of Materials in Open Air under Ambient Conditions. Anal. Chem. 77, 2297–2302 (2005). doi:10.1021/ac050162j

42. Harper, J.D., Charipar, N.A., Mulligan, C.C., Zhang, X., Cooks, R.G., Ouyang, Z.: Low-Temperature Plasma Probe for Ambient Desorption Ionization. Anal. Chem. 80, 9097–9104 (2008). doi:10.1021/ac801641a

43. Andrade, F.J., Shelley, J.T., Wetzel, W.C., Webb, M.R., Gamez, G., Ray, S.J., Hieftje, G.M.: Atmospheric Pressure Chemical Ionization Source. 1. Ionization of Compounds in the Gas Phase. Anal. Chem. 80, 2646–2653 (2008). doi:10.1021/ac800156y

44. Badal, S.P., Michalak, S.D., Chan, G.C.-Y., You, Y., Shelley, J.T.: Tunable Ionization Modes of a Flowing Atmospheric-Pressure Afterglow (FAPA) Ambient Ionization Source. Anal. Chem. 88, 3494–3503 (2016). doi:10.1021/acs.analchem.5b03434

45. Smirnov, B.M.: Theory of Gas Discharge Plasma. Springer International Publishing, Cham (2015)

46. Phelps, A. V., Molnar, J.P.: Lifetimes of Metastable States of Noble Gases. Phys. Rev. 89, 1202–1208 (1953). doi:10.1103/PhysRev.89.1202

47. Byrdwell, W.C.: Atmospheric pressure chemical ionization mass spectrometry for analysis of lipids. Lipids. 36, 327–346 (2001). doi:10.1007/s11745-001-0725-5

48. Küchler, A.: Hochspannungstechnik. Springer Berlin Heidelberg, Berlin, Heidelberg (2009)

49. Kücükarpaci, H.N., Saelee, H.T., Lucas, J.: Electron swarm parameters in helium and neon. J. Phys. D. Appl. Phys. 14, 9–25 (1981). doi:10.1088/0022-3727/14/1/004

50. Arikawa, T., Kanazawa, K., Tsurubuchi, S.: Penning and dissociative ionizaions of methane molecules in collisions with metastable helium atoms. J. Mass Spectrom. Soc. Jpn. 31, 97–104 (1983). doi:10.5702/massspec.31.97

51. Whitney, T.A., Klemann, L.P., Field, F.H.: Investigation of polytertiary alkylamines using chemical ionization mass spectrometry. Anal. Chem. 43, 1048–1052 (1971). doi:10.1021/ac60303a020

52. Milne, G.W.A., Lacey, M.J., Arsenault, G.P.: Modern Ionization Techniques in Mass Spectrometry. C R C Crit. Rev. Anal. Chem. 4, 45–81 (1974). doi:10.1080/10408347408542670

53. Roberge, W., Dalgarno, A.: The formation and destruction of HeH/+/ in astrophysical plasmas. Astrophys. J. 255, 489 (1982). doi:10.1086/159849

54. Smyth, H.D.: Primary and Secondary Products of Ionization in Hydrogen. Phys. Rev. 25, 452–468 (1925). doi:10.1103/PhysRev.25.452

55. Joyce, J.R., Richards, D.S.: Kinetic Control of Protonation in Electrospray Ionization. J. Am. Soc. Mass Spectrom. 22, 360–368 (2011). doi:10.1007/s13361-010-0037-0

56. Xia, H., Attygalle, A.B.: Untrapping Kinetically Trapped Ions: The Role of Water Vapor and Ion-Source Activation Conditions on the Gas-Phase Protomer Ratio of Benzocaine Revealed by Ion-Mobility Mass Spectrometry. J. Am. Soc. Mass Spectrom. 28, 2580–2587 (2017). doi:10.1007/s13361-017-1806-9

57. Klee, S., Derpmann, V., Wißdorf, W., Klopotowski, S., Kersten, H., Brockmann, K.J., Benter, T., Albrecht, S., Bruins, A.P., Dousty, F., Kauppila, T.J., Kostiainen, R., O'Brien, R., Robb, D.B., Syage, J.A.: Are Clusters Important in Understanding the Mechanisms in Atmospheric Pressure Ionization? Part 1: Reagent Ion Generation and Chemical Control of Ion Populations. J. Am. Soc. Mass Spectrom. 25, 1310–1321 (2014). doi:10.1007/s13361-014-0891-2

58. Kersten, H.: Development of an Atmospheric Pressure Ionization source for in situ monitoring of degradation products of atmospherically relevant volatile organic compounds, http://nbn-resolving.de/urn/resolver.pl?urn=urn:nbn:de:hbz:468-20110418-092806-6, (2011)

59. Klee, S.: Charakterisierung und Optimierung von Corona-Mikroplasma initiierten Ionisationsprozessen zur Anwendung in der Atmosphärendruckionisations-Massenspektrometrie, http://nbn-resolving.de/urn/resolver.pl?urn=urn%3Anbn%3Ade%3Ahbz%3A468-20140807-145941-9, (2014)

60. Constapel, M., Schellenträger, M., Schmitz, O.J., Gäb, S., Brockmann, K.J., Giese, R., Benter, T.: Atmospheric-pressure laser ionization: A novel ionization method for liquid chromatography/mass spectrometry. Rapid Commun. Mass Spectrom. 19, 326–336 (2005). doi:10.1002/rcm.1789

61. Syage, J.A.: Mechanism of [M + H]+ formation in photoionization mass spectrometry. J. Am. Soc. Mass Spectrom. 15, 1521–1533 (2004). doi:10.1016/j.jasms.2004.07.006

62. Klee, S., Derpmann, V., Wißdorf, W., Klopotowski, S., Kersten, H., Brockmann, K.J., Benter, T., Albrecht, S., Bruins, A.P., Dousty, F., Kauppila, T.J., Kostiainen, R., O'Brien, R., Robb, D.B., Syage, J.A.: Are clusters important in understanding the mechanisms in atmospheric pressure ionization? part 1: Reagent ion generation and chemical control of ion populations. J. Am. Soc. Mass Spectrom. 25, 1310–1321 (2014). doi:10.1007/s13361-014-0891-2

63. Brockmann, K.J., Wissdorf, W., Lorenz, M., Mueller, D., Poehler, T., Kunte, R., Benter, T.: Investigation of Ion Transfer Times in a commercial Atmospheric Pressure Ion Source. In: Proceedings of the 60thASMS Conference on Mass Spectrometry and Allied Topics. , Vancouver, BC, Canada (2012)

64. Brachthäuser, Y.: Development and characterization of a Fourier Transform based Quadrupole Ion Trap (FT-QIT) technique for process and residual gas analysis, http://nbn-resolving.de/urn/resolver.pl?urn=urn%3Anbn%3Ade%3Ahbz%3A468-20170717-144524-6, (2017)

65. Brachthaeuser, Y., Mueller, D., Kersten, H., Brockmann, K., Benter, T.: Development of a compact multiple-ionization-stage TOF mass analyzer system for trace component monitoring within chemically challenging process gas matrices. In: Procedings of the 62th ASMS Conference on Mass Spectrometry and Allied Topics. , Baltimore,MD, USA (2014)

66. AB Sciex: API 3200™ System Hardware Guide. System. (2010)

67. Goodwin, D.G., Moffat, H.K., Speth, R.L.: Cantera: An object- oriented software toolkit for chemical kinetics, thermodynamics, and transport processes, http://www.cantera.org, (2016)

68. Lorenz, M., Schiewek, R., Brockmann, K.J., Schmitz, O.J., Gäb, S., Benter, T.: The Distribution of Ion Acceptance in Atmospheric Pressure Ion Sources: Spatially Resolved APLI Measurements. J. Am. Soc. Mass Spectrom. 19, 400–410 (2008). doi:10.1016/j.jasms.2007.11.021

69. Anicich, V.: An index of the literature for bimolecular gas phase cation-molecule reaction kinetics. JPL Publ. 03-19. 1172 (2003)

70. Bartmess, J.E.: Gas-phase ion chemistry of 5-methylene-1,3-cyclohexadiene (o-isotoluene) and 3-methylene-1,4-cyclohexadiene (p-isotoluene). J. Am. Chem. Soc. 104, 335–337 (1982). doi:10.1021/ja00365a082

71. Milligan, D.B., Wilson, P.F., Freeman, C.G., Meot-Ner, M., McEwan, M.J.: Dissociative Proton Transfer Reactions of H3+ , N2H+ , and H3O+ with Acyclic, Cyclic, and Aromatic Hydrocarbons and Nitrogen Compounds, and Astrochemical Implications †. J. Phys. Chem. A. 106, 9745–9755 (2002). doi:10.1021/jp014659i

72. DIN 32645:2008-11: Chemical analysis - Decision limit, detection limit and determination limit under repeatability conditions - Terms, methods, evaluation.

73. Kebarle, P.: Ion Thermochemistry and Solvation From Gas Phase Ion Equilibria. Annu. Rev. Phys. Chem. 28, 445–476 (1977). doi:10.1146/annurev.pc.28.100177.002305

74. Hiraoka, K., Saluja, P.P.S., Kebarle, P.: Stabilities of complexes (N2)nH+ , and (O2)nH+ for n = 1 to 7 based on gas phase ion-equilibria measurements. Can. J. Chem. 57, 2159–2166 (1979). doi:10.1139/v79-346

75. Yu, Q., Bowman, J.M., Fortenberry, R.C., Mancini, J.S., Lee, T.J., Crawford, T.D., Klemperer, W., Francisco, J.S.: Structure, Anharmonic Vibrational Frequencies, and Intensities of NNHNN +. J. Phys. Chem. A. 119, 11623–11631 (2015). doi:10.1021/acs.jpca.5b09682